Systematic Characterization of RhoGEF/RhoGAP Regulatory Proteins Reveals Organization Principles of Rho GTPase Signaling

Paul M. Müller[1]*, Juliane Rademacher[1]*, Richard D. Bagshaw[2]*, Keziban M. Alp[1], Girolamo Giudice[3], Louise E. Heinrich[5], Carolin Barth[1], Rebecca L. Eccles[1], Marta Sanchez-Castro[2], Lennart Brandenburg[1], Geraldine Mbamalu[2], Monika Tucholska[2], Lisa Spatt[1], Celina Wortmann[1], Maciej T. Czajkowski[1,4], Robert-William Welke[1], Sunqu Zhang[2], Vivian Nguyen[2], Trendelina Rrustemi[1], Philipp Trnka[1], Kiara Freitag[1], Brett Larsen[2], Oliver Popp[1,4], Philipp Mertins[1,4], Chris Bakal[5], Anne-Claude Gingras[2,7], Olivier Pertz[6], Frederick P. Roth[2,8,9], Karen Colwill[2], Tony Pawson[2,7†], Evangelia Petsalaki[2,3+], Oliver Rocks[1,2++]

[1] *Max-Delbrück-Center for Molecular Medicine, Robert-Rössle-Strasse 10, 13125 Berlin, Germany*
[2] *Lunenfeld-Tanenbaum Research Institute, Sinai Health System, 600 University Avenue, Toronto, Ontario M5G 1X5, Canada*
[3] *EMBL-EBI, Wellcome Trust Genome Campus, Hinxton, Cambridgeshire, CB10 1SD, UK*
[4] *Berlin Institute of Health (BIH), Kapelle-Ufer 2, 10117 Berlin, Germany*
[5] *Institute for Cancer Research, Chester Beatty Laboratories, 237 Fulham Road. London SW7 3RP, UK*
[6] *Institute of Cell Biology, University of Bern, Baltzerstrasse 4 6, 3012 Bern, Switzerland*
[7] *Department of Molecular Genetics, University of Toronto, Toronto, ON, Canada*
[8] *Donnelly Centre and Departments of Molecular Genetics and Computer Science, University of Toronto, Toronto, Ontario M5S 3E1, Canada*
[9] *Canadian Institute for Advanced Research, Toronto, Ontario M5G 1Z8, Canada*
* these authors contributed equally
† Deceased
+ co-correspondence: petsalaki@ebi.ac.uk (E.P.)

++Lead Contact: oliver.rocks@mdc-berlin.de (O.R.)

Summary

Rho GTPases control cell shape formation and thus fundamental physiological processes in all eukaryotes. Their functions are regulated by 145 RhoGEF and RhoGAP multi-domain proteins in humans. To provide the framework for a systems-level understanding of how these regulators orchestrate cellular morphogenesis, we comprehensively characterized their substrate specificities, localization and interactome. The resulting resource places the RhoGEFs/RhoGAPs in functional context, serving as a foundation for targeted and integrated studies. Our data reveals their critical role in the spatial organization of Rho signaling. They localize to multiple compartments to provide positional information, are extensively interconnected to jointly coordinate their signaling networks and are widely autoinhibited to remain sensitive to local activation. RhoGAPs exhibit lower substrate specificity than RhoGEFs and may contribute to preserving Rho activity gradients. We demonstrate the utility of our integrated data by detailing a multi-RhoGEF complex downstream of G-protein-coupled receptors in which the enzymes mutually regulate their activities.

Introduction

Rho GTPases coordinate changes in cytoskeletal architecture to regulate cell shape. They drive fundamental aspects of cell behavior in all eukaryotes, including motility, cytokinesis and tissue morphogenesis (Heasman and Ridley, 2008; Jaffe and Hall, 2005). Defects in Rho signaling have been widely found in cancer metastasis and other serious diseases (Cook et al., 2014; Porter et al., 2016). 12 of the 20 family members are classical GTPases that cycle between an inactive GDP-bound and an active GTP-bound form (Bos et al., 2007). Upon activation, they bind effector proteins to initiate localized cytoskeletal remodeling processes. Their activity cycle is initiated by activating guanine nucleotide exchange factors (RhoGEFs) and terminated by GTPase activating proteins (RhoGAPs) (Hodge and Ridley, 2016). In addition, guanine nucleotide dissociation inhibitors (RhoGDIs) sequester the GTPases in the cytosol to render them inactive (Garcia-Mata et al., 2011).

Rho signaling responses in cells are highly localized. A critical aspect of Rho biology therefore is its spatiotemporal control (Pertz, 2010). Rho activities have been observed in confined subcellular domains at the front and rear of migrating cells (Fritz et al., 2013; Machacek et al., 2009), or in distinct zones during Xenopus oocyte wound repair or invadopodia assembly (Benink and Bement, 2005; Bravo-Cordero et al., 2011), with several GTPases operating simultaneously. Cell morphogenesis thus involves the concerted action of multiple Rho family members and their regulators, which together form complex spatially organized networks (Devreotes and Horwitz, 2015; Guilluy et al., 2011).

Humans express 66 proteins that contain RhoGAP domains (Tcherkezian and Lamarche-Vane, 2007). RhoGEFs comprise two subgroups: 70 Dbl homology–pleckstrin homology (DH-PH) domain proteins (García-Mata and Burridge, 2007; Rossman et al., 2005) and 11 members of the dedicator of cytokinesis (DOCK) family (Laurin and Cote, 2014). Two proteins, BCR and ABR, encode both a RhoGEF and RhoGAP domain. With 145 members, the RhoGEFs/RhoGAPs by far outnumber the 12 classical Rho GTPase switch proteins they regulate, allowing for complex control of Rho signaling activity and specificity. RhoGEFs and RhoGAPs are typically large proteins with a catalytic core and a spectrum of additional domains and sequence motifs that mediate protein-protein and protein-lipid binding (Figure S0). These modular components are

used as interaction scaffolds, for subcellular targeting or to autoregulate the catalytic activities through mechanisms including reversible intramolecular interactions (Aghazadeh et al., 2000).

Our current understanding of the spatial organization of Rho signaling is limited and stems from studies on single RhoGEFs and RhoGAPs, so that a systems-level view is lacking. A comprehensive characterization of all regulators is necessary to elucidate the constituents, contexts and coordination of the different Rho signaling networks. Here, we assembled a full-length expression library of 141 RhoGEFs and RhoGAPs and undertook such a study using a combination of proteomics, imaging and functional assays. We provide the first complete analysis of the substrate specificities of the regulators for RhoA, Rac1 and Cdc42 to link them to their downstream pathways. Our data reveal a high degree of promiscuity, particularly among the RhoGAPs, and indicate that most regulators are autoinhibited, permitting responsiveness to local stimuli. Our spatial mapping showed a strong enrichment of the regulators on all cellular compartments known to host Rho signaling, with a so far underestimated prevalence for focal adhesion localization, highlighting their importance in providing positional information to contextualize Rho signaling. Using mass spectrometry, we identified 1082 novel interactions of the regulators, connecting them to proteins in numerous signaling pathways. We found a large number of interactions amongst RhoGEFs and RhoGAPs themselves, hinting at a widespread interplay between Rho regulatory pathways that has not been previously recognized. The combined datasets introduce a framework for future in-depth studies on the diverse roles of RhoGEFs/RhoGAPs in the control of Rho GTPases and will help to advance our understanding of the spatial and temporal regulation of cell shape in fundamental physiological processes. Moreover, they reveal common organization principles underlying the generation of localized signaling activity patterns that may also apply to other reaction cycles in signal transduction.

We demonstrate the utility of this resource by detailing a novel multi-RhoGEF complex formed by the well-studied RhoA regulators ARHGEF11 and ARHGEF12 and the yet uncharacterized Cdc42 GEF PLEKHG4B, showing that the enzymes mutually regulate their catalytic activities to modulate Rho signaling downstream of G protein-coupled receptors.

Results

cDNA expression library of full-length mammalian RhoGEFs/RhoGAPs

To comprehensively characterize all mammalian RhoGEFs and RhoGAPs, we generated an expression library comprising 141 full-length cDNAs of these proteins. Almost all of the constructs represent the longest isoform known to exist (Figure S0; Table S1; STAR Methods). The collection includes 64 potential Dbl family RhoGEFs, the 11 DOCK family RhoGEFs, 64 RhoGAP domain-containing proteins and two proteins with dual RhoGEF/RhoGAP functions. Of these, the majority (112) comprise human-derived cDNAs.

Family-wide RhoGEF and RhoGAP activity screens

As a first step towards an integrative understanding of how RhoGEFs and RhoGAPs control Rho signaling responses, we systematically characterized their substrate specificities to link them to their downstream pathways. By reviewing over 450 publications in which claims on substrate specificities had been made, we found an incomplete data landscape with a high degree of conflict between reports (Table S2, STAR Methods). Many discrepancies can be attributed to differences in experimental approaches and setups, highlighting the need for a standardized comprehensive analysis. To achieve this, we devised the first screening-compatible automated live cell imaging assay using the latest generation of FRET-based biosensors for the canonical GTPases RhoA, Rac1 and Cdc42 (Fritz et al., 2013, 2015; Martin et al., 2016). This approach allows the analysis of full-length regulators in their native cellular environment. Extensive control experiments demonstrated the sensitivity and robustness of this assay (Figure S1, STAR Methods). We found catalytic activities towards RhoA, Rac1 or Cdc42 for 45 out of 75 RhoGEFs and for 48 out of 63 RhoGAPs tested. In addition, the dual GEF/GAP proteins ABR and BCR both exhibited GAP activity (Figure 1, Table S2). The active regulators included proteins whose substrate specificity was exclusive to one target (35 RhoGEFs, 31 RhoGAPs) but also many that regulated multiple Rho GTPases (10 RhoGEFs, 19 RhoGAPs). Our results thus not only reveal extensive promiscuity among the regulators, but also that in the GDP/GTP reaction cycle the inactivating RhoGAPs tend to be less selective than the activating RhoGEFs (p-value=0.02, STAR Methods). This is also supported by the literature search in which we found approximately

twice as many promiscuous RhoGAPs as RhoGEFs (Table S2). Promiscuity has been predominantly reported in the co-regulation of Cdc42 and Rac1, presumably because they control related cytoskeletal processes such as the formation of actin-rich protrusions at the leading edge (Jaffe and Hall, 2005; Lawson and Ridley, 2018). However, we found a similar number of regulators that control RhoA together with Cdc42 and/or Rac1 (18 and 17 vs. 16), and thus GTPase combinations that elicit more diverse downstream responses, including RhoA-dependent regulation of actomyosin contractility. While we see high overall agreement of identified substrate specificities with existing data (70%, Table S2, STAR Methods), we describe 10 entirely novel activities. PLEKHG4B, for instance, turned out to be a strong and exclusive Cdc42 GEF (see also Figure 7), and SYDE2 a GAP specific to Rac1. The screen also revealed discrepancies with earlier reports. For example, the previously proposed representative Cdc42-specific GAPs ARHGAP1, ARHGAP17 or ARHGAP31 (CDGAP) showed either no activity towards this GTPase in our assay or rather inactivated Rac1 more efficiently. In fact, none of the GAPs tested in our screen exhibited an exclusive substrate specificity for Cdc42, although 21 GAPs promiscuously regulated Cdc42. By contrast, we found exclusive Cdc42 activity for a total of 12 GEFs.

Autoinhibition is a common feature of RhoGEFs and RhoGAPs

Some RhoGEFs and RhoGAPs displayed minimal or no activity in our screen. A requirement for relief from autoinhibition via mechanisms such as phosphorylation, protein or lipid interactions may account for the observed inactivity. Such regulation has been exemplified for a number of RhoGEFs and a few RhoGAPs (Cherfils and Zeghouf, 2013). However, the extent to which autoinhibition is a more general mechanism in controlling the functions of full-length Rho regulators is unknown. We therefore included shorter isoforms or truncated versions of 9 RhoGEFs and 10 RhoGAPs in the screen, which lack potential regulatory elements present in the longest isoforms. For 13 of these regulators, we indeed found that the catalytic efficiency of the shorter proteins was higher than for the longer ones (Figure 2). Cellular regulatory conditions are thus preserved in our assay. ARHGAP9 normally only exhibits catalytic activity towards Rac1 as its longest isoform. Surprisingly, when we expressed isoform 3, lacking an N-terminal SH3 domain, it also inactivated Cdc42. This suggests that autoregulatory features

might not only modulate the catalytic efficiency of Rho regulators but also affect their substrate selectivity. Overall, our data shows that RhoGEFs and RhoGAPs are widely subject to autoinhibition.

RhoGEF/RhoGAP expression results in a continuum of cell morphologies

Given the role of Rho signaling in regulating cell morphology, we sought to explore the association between the specificity of RhoGEFs and RhoGAPs for particular downstream Rho GTPases and the effect of RhoGEF/RhoGAP expression on cell shape. We observed a rounded phenotype in MDCK cells transiently expressing RhoGEFs with substrate specificity for RhoA, while cells expressing GAPs with RhoA activity tended to be 'arborized', with long membrane extensions (Figure S2). To further investigate such associations, we used high-content microscopy (Bakal et al., 2007) to accurately quantify phenotypes resulting from overexpression of each of the regulators and asked whether this can be used to predict their specificity for RhoA, Rac1 or Cdc42 (STAR Methods). While we were able to predict RhoA-specific GEFs with reasonable accuracy (optimal cutoff at ~50% precision at 50% recall; STAR Methods), we did not find a direct relationship between substrate specificity and cell morphology for the rest of the regulators. Expression of RhoGEFs/RhoGAPs thus results in a continuum of cell morphologies that contrasts the classical categories of rounded (RhoA), lamellipodia (Rac1) and filopodia (Cdc42) observed upon global expression of the respective GTPases (Hall, 1998).

RhoGEFs and RhoGAPs display diverse spatial distribution in cells

To understand how RhoGEFs and RhoGAPs spatially orchestrate Rho signaling, we mapped the subcellular distribution of all 141 regulators in our library at steady-state. We first used confocal live-cell microscopy in MDCK epithelial cells to assign transiently expressed YFP fusion proteins to one (or more) of the following main localization categories: cytoplasm, plasma membrane, vesicles, cytoskeleton, focal adhesions, nucleus, Golgi, mitochondria, lysosomes, endomembranes and endoplasmic reticulum. This analysis revealed that over half of RhoGEFs and RhoGAPs (76/141) inherently localize to distinct structures, collectively decorating virtually all cellular compartments (Figure 3A & D, Figure S3, Table S3; Biostudies:S-BSST160). For two

proteins, ARHGAP9 and MCF2L2, we observed dependence of localization on the position of the fluorescent protein tag (Figure S3). Interestingly, C-terminally tagged ARHGAP9-YFP localized to mitochondria while a fusion of YFP at the N-terminus was enriched at cell junctions, perhaps because the N-terminal fusion disrupted a mitochondrial targeting signal predicted for ARHGAP9 residues 1-14 (PredSL tool (Petsalaki et al., 2006)). Consistent with this, we observed loss of mitochondrial localization for ARHGAP9 isoform 3 (ARHGAP9_iso3-YFP), which lacks the first 181 N-terminal amino acids. We identified eight other cases in which different isoforms exhibited distinct localization pattern: ARHGAP26, ARHGAP36, ARHGEF16, ARHGEF25, CHN1, DNMBP, SRGAP1 and SYDE1 (Figure S3; Biostudies:S-BSST160).

Focal adhesions are major sites of Rho GTPase regulation

Because the localization of the regulators on focal adhesions and actin filaments, two key sites of Rho signaling, cannot be optimally resolved using confocal microscopy, we carried out additional screens to further refine the RhoGEF/RhoGAP distribution atlas. First, we used total internal reflection fluorescence (TIRF) microscopy in COS-7 cells (which have a flat morphology) to resolve additional regulators enriched on focal adhesions. This led to the identification of as many as 37 RhoGEFs and RhoGAPs that clearly associated with these structures, as determined by colocalization with the adhesion marker paxillin. These included well-studied regulators such as SOS1, TRIO, CHN2 and KALRN that have not previously been reported at focal adhesions (Figure 3B, Figure S4A; Biostudies:S-BSST160). A systematic literature search yielded evidence for localization to focal adhesions for only 13 of these proteins (Table S3). Previous efforts to define the components of the integrin adhesome have already revealed a prevalence of Rho GTPase signaling network proteins (Winograd-Katz et al., 2014; Zaidel-Bar et al., 2007). 9 RhoGEFs/RhoGAPs were previously proposed to be an integral part of the adhesome (adhesome.org); we could confirm six of them. Notably, six of the focal adhesion-associated regulators exhibited a distinct microlocalization with a pericentric enrichment juxtapositioned to focal adhesions and a fluorescence intensity minimum in the center (Figure 4A). We also noticed that RhoGEFs and RhoGAPs with activity towards Rac1 were overrepresented at focal adhesions compared to RhoA and Cdc42 (Figure 4B, Tables S2, S3). Again, this finding is supported by data from the literature review (Figure S4B).

Prevalence of actin-associated RhoGEFs and RhoGAPs

Next, we focused on regulators associating with actin. We treated cells with Cytochalasin D, an agent that disrupts the actin network and induces the appearance of phalloidin-reactive filamentous foci (Schliwa, 1982). By scoring transiently expressed RhoGEFs and RhoGAPs for their association with these foci (STAR Methods), we identified in total 34 actin-associated proteins, including 11 proteins previously reported to bind to actin, such as MYO9B and ARHGAP42. Of these 34 proteins, 23 were novel, including DOCK1, ITSN2 and ARHGAP5 (Figure 3C and Figure S4C; Biostudies:S-BSST160). RhoGEFs and RhoGAPs with activity towards Cdc42 were overrepresented for association with actin relative to RhoA and Rac1 (Figure 4B).

Overall, we found 99 (70%) of the 141 overexpressed RhoGEF/RhoGAP proteins to be enriched on one or more subcellular locations at steady-state (Figure 3D, Table S3) with a distribution as follows: 40 plasma membrane (thereof 13 enriched at cell junctions), 37 focal adhesions, 38 cytoskeleton (33 actin, 1 tubulin, 3 undefined filaments, 1 filaments and actin), 19 vesicles and 10 nucleus (1 thereof nuclear membrane), and further: 1 Golgi, 1 mitochondria, 1 lysosomes, 1 endomembranes and 1 endoplasmic reticulum. 39 (28%) of the regulators localized to multiple organelles. RhoGEFs and RhoGAPs thus extensively localize to all cellular compartments previously known to harbor Rho signaling. Notably, the latter five 'non-canonical' locations were only decorated by RhoGAPs. We thus did not find evidence for Rho stimulating activities at these structures. In addition to Rac1 and Cdc42 regulators being enriched on focal adhesions and actin, respectively, we observed an enrichment of RhoGEFs/RhoGAPs with activity towards RhoA in the nucleus (Figure 4B). Compared to a control set of proteins from the Cell Atlas study (Thul et al., 2017), significantly more proteins in our RhoGEF/RhoGAP screen localized to focal adhesions, actin and the plasma membrane (Fisher's exact test p-values < 2.2e-16, < 2.2e-16, 4.154e-07 and odds ratios=30.2, 14.5 and 2.9 respectively). Compared to a study that used confocal microscopy in a similar manner as our study to assess localization (Simpson et al., 2000), the RhoGEFs/RhoGAPs in our set were significantly enriched in terms of discrete localization (i.e. not cytoplasm or nucleus; p-value=4.083e-09, odds ratio=3.0). Our literature search revealed that for 27 (19%) of the regulators in our collection, there were no previous reports describing their localization, and 28 (20%) and 53 (37.5%) were not annotated in the

Cell Atlas and Uniprot databases, respectively. For 38 proteins (27%) the localizations we found were different from those reported in the literature (Table S3). We thus provide a detailed map of the cellular RhoGEF/RhoGAP distribution revealing the spatial context of all regulators.

The RhoGEF/RhoGAP interactome is highly interconnected and includes components of multiple cellular processes

To determine the constituents of the RhoGEF/RhoGAP signaling networks, we used affinity purification coupled to mass spectrometry to obtain a comprehensive description of their interactome (STAR Methods). After analyzing raw data from 855 samples, we obtained a high quality, interconnected network of 1292 interactions (silver set; 1082 novel) among 863 unique proteins (STAR Methods, Figure 5A, Table S4). The interactors are enriched in Gene Ontology (GO) terms (Berriz et al., 2009) connected to regulation by Rho signaling (Figure S5A; STAR Methods). Our dataset explores a so far largely uncharted part of the human interactome and connects Rho GTPases to several signaling pathways (Figure S5B) and functional complexes involved in linking the actin cytoskeleton to critical cell functions. The RhoGEF/RhoGAP interactome, for example, connects the dystrophin complex, which anchors the extracellular matrix to the actin cytoskeleton, to proteins involved in cell polarity regulation, for example SCRIB and DLG1. These are in turn associated with ERM family proteins (EZR-MSN-RDX), which link the cytoskeleton to the plasma membrane and, further, to cell junction regulators such as components of the cadherin/catenin complex or the tight junction protein TJP2. This subnetwork is also connected to the Rich1/Amot polarity complex, components involved in regulation of the actin cytoskeleton and membrane trafficking (Figure 5A).

Notably, in addition to 20 interactions between RhoGEFs or RhoGAPs and Rho effector proteins and 24 interactions with small GTPases, our network includes as many as 66 unique interactions between RhoGEFs/RhoGAPs themselves, indicating an extensive crosstalk among the Rho regulators (Figure 5B, enrichment p-value for all $<<0.001$; STAR Methods). To assess the quality of our dataset, we tested 26 RhoGEF/RhoGAP pairs by co-immunoprecipitation and successfully validated 22 interactions (Figure S5C). Both homo- and heterotypic interactions occurred, with fewer complexes between RhoGAPs (24 GEF/GAP, 28 GEF/GEF, 11 GAP/GAP

and 3 GEF-ABR or GEF-BCR). Connections include complexes that localize to the same cellular compartment, such as FARP2-VAV1 on focal adhesion, ARHGAP28-SYDE1 on actin filaments or BCR-ARHGEF39 at the plasma membrane, where they may act in concert to fine-tune Rho responses (Figure 5B). We also noticed the frequent association of close homologs such as ARHGAP17 and ARHGAP44 (RICH1 and RICH2), INPP5B and OCRL (INPP5F) or ARHGEF10 and ARHGEF10L.

Network data reveals interactors controlling RhoGEF/RhoGAP localization

Our network data provides a rich source of information that can be used to functionally characterize individual regulators (Eccles et al., 2016) or be combined with the other datasets for hypothesis generation. For example, we found that the interactomes of the focal adhesion-associated RhoGEFs/RhoGAPs are enriched in components of the adhesome (Zaidel-Bar et al., 2007) (Biostudies:S-BSST160; p-value=2.5e-08, odds ratio 2.3) and asked whether we could identify interactors that are responsible for their local recruitment. We selected ARHGAP39, a neuronal RacGAP controlling synaptic plasticity (Lee et al., 2017), and confirmed its interaction with PEAK1, a kinase implicated in cancer progression. We found PEAK1 also to localize on focal complexes, as previously reported for this protein (Wang et al., 2010). The interaction critically involves one of the WW domains of ARHGAP39: when this domain is disrupted by a Y81A point mutation, it not only fails to associate with PEAK1 but is also no longer recruited to focal adhesions (Figure 6A-C). Further examples of interactions potentially mediating focal adhesion targeting are those between ARHGAP12 and ASAP1/2, ARHGAP31 and Talin or ARHGAP9 and ASAP1 or CRKL (Table S4). Similarly, the interactome of actin-localized regulators is enriched in actin-binding proteins (Biostudies:S-BSST160; p-value=1e-13, odds ratio=7.2), whose function may be to locally recruit these RhoGEFs/RhoGAPs. Examples are the interactions between ITSN2, ARHGEF15 and ARHGAP11A and the well-known actin-binding proteins Vinculin, Radixin and Gelsolin/Caldesmon, respectively.

Our spatial distribution screen may miss localizations that require the presence of stoichiometric concentrations of partner proteins or the delivery of a specific stimulus to create local protein or lipid binding sites. However, our network data can be used to investigate such cases. For example, we saw that members of the C-DOCK RhoGEF subfamily

(DOCK6, DOCK7 and DOCK8) form a highly interconnected network with the four members of the LRCH protein family (Leucine-Rich-Repeats (LRR) and a Calponin Homology (CH)) (Figure 6D-F, S6; Table S4). Indeed, we found that coexpression of the LRCH proteins caused a striking relocalization of the three RhoGEFs from the cytosol to the sites of LRCH expression; peripheral actin filaments and the endoplasmic reticulum.

A multi-RhoGEF complex downstream of GPCR

To further explore the potential of the resource, we focused on two key findings of our study, the extensive interconnection of the RhoGEF/RhoGAP regulators and the widespread autoregulation. To this end, we functionally characterized a multi-RhoGEF complex identified in our proteomics analysis: the interaction between the yet undescribed RhoGEF PLEKHG4B and ARHGEF11 and ARHGEF12, two well-studied activators of RhoA signaling downstream of G protein-coupled receptors (GPCR) that have been shown to be essential for chemokine signaling-driven tumor cell invasion (Struckhoff et al., 2013; Yagi et al., 2011) (Figure 5B,7A). ARHGEF11/12 are engaged at the membrane upon GPCR stimulation when activated heterotrimeric G alpha 12 and 13 subunits bind to the RGS (regulator of G protein signaling) domains of the GEFs (Sternweis et al., 2007). PLEKHG4B is one of the eight members of the Pleckstrin homology domain containing family G (PLEKHG) proteins. We confirmed by co-immunoprecipitation that ARHGEF11 and ARHGEF12 exclusively associate with PLEKHG4B, but not with any of the other PLEKHG family proteins (Figure S7A). The N-termini of the three proteins are critical to this interaction (Figure 7B). While ARHGEF11 and ARHGEF12 are RhoA-specific, PLEKHG4B selectively activated Cdc42 (Figure 1,7C) and thus draws an additional Rho GTPase substrate into this multi-GEF assembly. Next, we investigated how the GEF activities of the proteins are regulated within the complex. We observed that the truncation of the N-terminus of PLEKHG4B increased its Cdc42 GEF activity compared to the full-length form, through both FRET biosensor and a luciferase reporter assay (Figure 7E,S7B, STAR Methods). PLEKHG4B is therefore another RhoGEF that is subject to autoinhibition. An increase in the Cdc42 GEF activity of full-length PLEKHG4B appeared when we added either N-terminal fragments of ARHGEF11 or ARHGEF12 or catalytically inactive mutants (Figure 7C-E). This

suggests that binding to its partner GEFs releases the autoinhibition of PLEKHG4B. Conversely, coexpressing an N-terminal fragment of PLEKHG4B or its GEF-inactive mutant strongly decreased the catalytic activities of ARHGEF11 and ARHGEF12 towards RhoA (Figure 7D,F). The three proteins thus mutually control one another's GEF activities. We finally investigated the function of the multi-GEF complex in the context of the GPCR signaling pathway. As expected, both ARHGEF11 and ARHGEF12 selectively associated with constitutively active Gα13QL. Addition of PLEKHG4B, however, inhibited this interaction (Figure 7G, upper panels). Fittingly, while the expression of Gα13QL robustly activated downstream Rho signaling through engagement of the endogenous RGS domain-containing RhoGEFs, this response was inhibited by the dominant negative ARHGEF11 N-terminus that competes with the endogenous GEFs for Gα13 binding (Fukuhara et al., 2000). Importantly, the N-terminus of PLEKHG4B, also capable of binding to ARHGEF11/12, caused an equally strong inhibition of Gα13 signaling.

To our knowledge, this is the first description of a multi-Rho regulator assembly, consisting of exchange factors with different GTPase specificities. In complex, ARHGEF11 and ARHGEF12 enhance the Cdc42 GEF activity of PLEKHG4B. In return, PLEKHG4B inhibits ARHGEF11/12-mediated RhoA activation in two ways: directly by reducing their catalytic activity, and indirectly by perturbing their engagement by Gα12/13. By exploiting our family-wide multiplex datasets, we thus provide a proof of concept for a novel mechanism of cross-talk among Rho GTPases in a pathway implicated in cancer metastasis, with a shift in Rho signaling between RhoA and Cdc42 (Figure 7H).

Discussion

Rho GTPase signals translate into complex morphodynamic cell behaviors. Approximately every 150th gene in human encodes a RhoGEF or RhoGAP protein. Understanding how these regulators spatially orchestrate Rho signaling networks through their multi-domain architecture can provide a paradigm for the context-specific control of cell responses. Here, we have provided the first systems-level view of RhoGEF/RhoGAP function by presenting a comprehensive analysis of key properties of these proteins. These datasets together

unravelled emergent organization principles of Rho signaling control that had not been visible in studies of individual regulators.

Promiscuity, differential specificities and autoregulation in the Rho regulatory system

We have established a screening assay for RhoGEF/RhoGAP activity and provide a systematic overview of the substrate specificities of the regulators for the canonical GTPases RhoA, Rac1 and Cdc42. Carrying out such a study under standardized conditions has long been needed given the incomplete and inconsistent data landscape. For reference and comparison, our resource includes an extensive review of literature annotations regarding specificity, making this a 'one-stop-shop' for information on these proteins.

The screen revealed new global insights into the Rho regulatory system. Our finding that a large number of RhoGEFs/RhoGAPs exhibit promiscuous substrate specificities is consistent with findings that Rho signaling typically involves the concurrent action of multiple Rho GTPases within the same spatio-temporal niche (Machacek et al., 2009; Martin et al., 2016). Promiscuity may thus be a favorable feature of the RhoGEFs and RhoGAPs. Rather than introducing noise to the signaling system due to spurious engagement of effectors, it may in fact be required for the proper parallel activation of downstream pathways to simultaneously control distinct cytoskeletal structures. The combinatorial possibilities to fine-tune the activities of the different Rho family members involved can further increase if multiple regulators cooperate with each other, as suggested by our interactome analysis. This reveals that in the past, many Rho regulators have been functionally placed into oversimplified linear pathways in which they were assumed to control only one Rho GTPase and one specific cytoskeletal response.

We found that RhoGAPs exhibit lower substrate specificity than RhoGEFs. This is in agreement with a biochemical study in which only limited selectivity for Rho, Rac or Cdc42-like GTPases was observed for the catalytic domains of 10 RhoGAPs (Amin et al., 2016), in contrast to a preceding analysis of RhoGEF domains which were more selective (Jaiswal et al., 2013). The lower substrate specificity of the GAPs is reminiscent of other fundamental reaction cycles driven by the activities of opposing enzymes. The catalytic domains of inactivating protein phosphatases, for example, also typically display lower sequence selectivity than their kinase

counterparts. The same may hold true for the opposing regulators of histone acetylation and of protein ubiquitination (Smoly et al., 2017). This has led to the view that the inactivating enzymes may fulfill a housekeeping function to rapidly reset the basal state of the reaction cycle. Although certainly not true for all phosphatases or RhoGAPs, this concept deserves further investigation as it may explain how GAPs contribute to the maintenance of transient and localized Rho signaling responses.

The lack of any GAP in our screen with exclusive substrate specificity for Cdc42 is surprising. This is unlikely due to missing distinguishing structural features in the interface of the Cdc42/GAP complex, given that RhoGEFs can readily discriminate Cdc42 from other Rho GTPases. Crystal structures of RhoGEF domain/Rho GTPase complexes have yielded specificity-determining residues in the interface (Jaiswal et al., 2013; Schaefer et al., 2014), however, current data regarding RhoGAP/Rho GTPase complexes is too sparse to draw conclusions. The lack of Cdc42-GAP specificity could mean that Cdc42 is never operating alone in cells and that whenever its activity is terminated, either RhoA or Rac1, or both, are switched off at the same time. It will be interesting to determine whether Cdc42/Rac1 and Cdc42/RhoA form unique functional units in the control of distinct morphodynamic processes that require simultaneous termination. Cdc42 activity often peaks at early stages of cellular morphogenesis, for instance during cell polarization, protrusion or adhesion. Another explanation could be that it has a unique initiating role in these processes and that a failsafe termination of the underlying signaling programs requires the rigorous inactivation of the entire cascade of Rho GTPases involved.

One cause of discrepancies between data from our activity screen and previous reports is surely differences between *in vitro* and *in vivo* experiments. Our cell-based assay revealed the importance of using the full-length multi-domain architecture of RhoGEFs and RhoGAPs in analyses of their substrate specificities. It takes into account posttranslational modifications and protein-protein/protein-lipid interactions of the regulators in their cellular environment. This feature of our assay led us to the conclusion that most RhoGEFs and RhoGAPs are autoinhibited. This has been described for several individual RhoGEFs. The mechanism typically involves the inhibitory binding of the PH domain to the adjacent DH domain (Rojas et al.,

2007), or a back-folding of mostly N-terminal regions onto the DH domain, thereby preventing access of the regulators to their substrates (Mitin et al., 2007). RhoGAPs are less well studied but seem to be subject to similar mechanisms of sterical inhibition (Canagarajah et al., 2004). Autoinhibition maintains the regulators in a 'stand-by' low activity state which allows the precise release of inhibition by context-specific upstream signals or, alternatively, by feedback regulation. Many RhoGEFs and RhoGAPs are already enriched on distinct supramolecular structures. A localized activating stimulus can further confine their activity to a designated zone of micrometer size. Interestingly, RhoGAPs have significantly fewer domains than RhoGEFs (p-value=5e-04, STAR Methods). Together with their lower tendency to engage in homotypic complexes, this may contribute to more autonomy of RhoGAPs from regulation.

Data from *in vitro* RhoGEF/RhoGAP assays are no less important due to their higher accuracy and sensitivity and the view they provide on biochemical activities. They reveal the rate constant of catalysis, typically of a recombinant isolated catalytic domain in a cuvette, rather than the activity of a full-length regulator in a cellular context. Therefore, the catalytic efficiencies determined *in vitro* and *in vivo* may not always correlate. For example, *in vitro*, the DH-PH domain of ARHGEF12 caused a dramatic increase in RhoA activation while that of MCF2L had only a moderate effect (Jaiswal et al., 2013). In contrast, MCF2L was far more active towards RhoA than ARHGEF12 in our full-length protein screen. Inversely, TIAM1 was the strongest Rac1 GEF in our assay, whereas its DH-PH domain showed relatively weak activity towards Rac1 in the *in vitro* study. Under cell-free conditions, the substrate selectivity of RhoGEFs and RhoGAPs may also differ. ARHGAP32 and ARHGAP8 are two examples where different *in vitro* selectivities for RhoA, Rac1 and Cdc42 were observed compared to *in vivo* pull-down assays (Okabe et al., 2003; Shang et al., 2003). It has been suggested that regions adjacent to the GAP domain of RhoGAPs contribute additional determinants of specificity (Amin et al., 2016). Not all RhoGEFs and RhoGAPs tested in our screen may regulate the canonical Rho GTPases RhoA, Rac1 and Cdc42. For example, ARHGEF26, which only showed moderate activity towards Cdc42 in our study is presumably a GEF for RhoG (Ellerbroek et al., 2004).

Overexpression of RhoGEFs and RhoGAPs resulted in a continuum of cell morphologies different from the clear-cut phenotypes observed upon global expression of activated forms of the Rho GTPases (Hall, 1998). We thus found only a limited relation between induced cell shapes and substrate specificities of the regulators. The diversity of cell morphologies is not surprising as it reflects the promiscuity, cooperativity and, most importantly, the differential subcellular distribution of the RhoGEFs and RhoGAPs.

RhoGEFs/RhoGAPs provide spatial information to Rho signaling

This study presents the first in-depth analysis of the steady-state subcellular localization of mammalian RhoGEFs/RhoGAPs. We find a striking enrichment of the regulators in multiple cellular compartments, establishing their crucial roles in conveying spatial information to Rho signaling. Previous studies have already described how RhoGEFs and RhoGAPs elicit localized signaling responses. Microtubule-associated ARHGEF2, for example, activates RhoA upon tubulin depolymerization (Krendel et al., 2002) and ARHGAP17 associates with polarity proteins at apical junctions to fine-tune tight junction integrity (Wells et al., 2006). Once again, the systemic view is illuminating: our detailed localization atlas provides not only cellular contexts for the function of all RhoGEFs and RhoGAPs but also a 'heat map' of Rho regulation. Besides the plasma membrane and the vesicular compartment, two prominent sites of Rho signaling, we found a remarkable one fourth of the regulators localize at least partially to focal adhesions. These structures serve as combinatorial hubs where scaffolding molecules, kinases, phosphatases, GTPases and other proteins are dynamically assembled into complexes to regulate migration and other cell behaviours and to initiate signaling pathways in response to adhesion events. It is here that Rho proteins control the coupling of actin to integrin complexes and the contractility of actomyosin to generate mechanical tension (Guilluy et al., 2011; Parsons et al., 2010). Although roles are yet to be assigned for most of the 37 RhoGEFs/RhoGAPs we identified at focal adhesions, our data strongly suggests that intricately tuned Rho signaling is far more crucial in the control of cell-matrix adhesion than previously assumed. The finding that some regulators localize to a narrow zone pericentral to focal complexes opens up the exciting possibility that the regulation of Rho GTPase activities is further micro-compartmentalized at these structures. A similar localization pattern has been

described for invadopodia, which were found to be surrounded by ARHGEF28 to activate RhoC, while ARHGAP35 localized inside these structures to locally inhibit the GTPase (Bravo-Cordero et al., 2011). Combining our localization catalog with the other datasets we generated will help to further spatially and temporally untangle the diverse functions of the Rho GTPase family members during the different stages of adhesion complex maturation. The prevalence of Rac1-specific regulators at these structures that emerged from our family-wide analysis will fuel future research on the importance of regulated actin branching at these sites.

Rho signaling is crucial for cytoskeleton dynamics, making it no surprise we found 34 actin-associated RhoGEFs and RhoGAPs. This almost doubles the number of regulators known to associate with these structures. One possibility is that these proteins control actin remodeling processes that require added spatial precision. It is also conceivable that these RhoGEFs and RhoGAPs use their multi-domain architecture to position additional cytoskeleton regulatory proteins to the site of action or to link actin dynamics to systemic signaling responses. It will be interesting to investigate whether some of the RhoGEFs and RhoGAPs are subject to feedback regulation by these cytoskeletal regulatory proteins, or whether actin binding itself modulates their catalytic activities.

Our experiments uncovered a large fraction of RhoGEFs and RhoGAPs whose subcellular locations differed from those previously reported. There are several potential explanations: errors in automated annotations in Uniprot or through the unspecific binding of antibodies in the Cell Atlas database, the analysis of different isoforms, different cell lines or differences in experimental conditions. It is of note, however, that our data agrees mostly with individual studies, in which researchers had a more focused interest in single proteins. The fact that there is only little agreement with literature and databases for the focal adhesion and actin-associated regulators demonstrates the added sensitivity of our TIRF and Cytochalasin D screens.

The subcellular targeting information of many RhoGEFs and RhoGAPs is likely encoded in their diverse domains or motifs (e.g. nuclear localization signals in all 9 nuclear-localized regulators (ELM server; Dinkel et al., 2016)). But protein-protein interactions probably play an equally important role. We demonstrated that the C-DOCK RhoGEFs are recruited to distinct

subcellular sites by the LRCH family proteins and that ARHGAP39 is targeted to focal adhesions by PEAK1. Many more such events may emerge from the interactions in our network. Both RhoGEFs/RhoGAPs and their interactors are significantly enriched for PDZ, SH2, WW and SH3 domains (p-values <<0.01, Table S2), which are common in scaffold or adaptor proteins. The role of interaction partners in the recruitment of the Rho regulators to specific cellular locations highlights the importance of combining interactome and localization information in the design of future studies.

Interconnection of the RhoGEF/RhoGAP interactome

Our RhoGEF/RhoGAP network analysis yielded the first systematic interactome of these proteins and provides a basis for generating hypotheses and the design of both targeted and systems-level studies. One example of the potential of this network is our previous characterization of the interaction between ARHGAP36 and the catalytic subunit of protein kinase A (PKA). It led us to discover an unanticipated function of the RhoGAP as a potent antagonist of PKA signaling and thus added a novel layer of regulation for this kinase (Eccles et al., 2016).

We find that the RhoGEFs and RhoGAPs engage in a remarkable number of interactions, hinting at an extensive crosstalk among these proteins that was previously unrecognized. A few examples of associations between Rho regulators have already been reported: for instance ECT2 and RACGAP1 interact to regulate cytokinesis (Miller and Bement, 2009) and BCR and TIAM1 cooperate to control excitatory synapse development (Um et al., 2014). Our interactome shows that many more regulators associate in complexes. Collaborative networks of interactions within similar protein classes have been described previously for phosphatases and kinases to interlink distinct types of cellular responses and to add robustness to signaling systems (Breitkreutz et al., 2010; St-Denis et al., 2016). Here, we used our dataset to uncover a multi-RhoGEF assembly that adds to the intricate spatio-temporal regulation of GPCR-mediated signaling in a pathway implicated in tumor cell invasion. This case study revealed several novel findings. ARHGEF11/ARHGEF12/PLEKHG4B form the first known functional complex constituted of three Rho regulators. PLEKHG4B exclusively activates Cdc42 and thereby expands the repertoire of downstream GTPases in the Gα12/13 pathway which was

previously thought to only activate RhoA (Diviani et al., 2001; Lenoir et al., 2014). The trimeric complex is subject to intricate cross-regulation: Cdc42 activation is triggered by ARHGEF11 and ARHGEF12 which release the autoinhibition of PLEKHG4B, while the latter restricts Gα12/13-mediated RhoA activation by inhibiting ARHGEF11/12 GEF activity and by blocking their access to the G alpha subunits.

Concluding Remarks

Over the past decade, our understanding of Rho signaling has advanced beyond a linear 'Rho-centric' concept in which a static GTPase was presumed to be sequentially regulated by a GEF and a GAP to control one specific cytoskeletal structure. This study establishes the framework for a more elaborate 'regulator-centric' model. A critical function of the RhoGEFs and RhoGAPs is to contextualize the Rho signaling networks and to delimit their spatial expanse. They do so by providing positional cues based on the placement of the enzymes on dedicated supramolecular structures and the assembly of additional signaling proteins. The regulators can associate to cooperative networks and thereby increase the combinatorial possibilities to fine-tune the activities of multiple Rho family members simultaneously. Our discovery that most regulators are autoinhibited suggests a mechanism by which they are poised to respond to specific upstream stimuli and feedback control, which can further spatially confine the activity of the regulators on the supramolecular structures. Diffusion spreads the activated Rho GTPases and thereby the local morphogenetic signals from their source. This is balanced by an efficient turnover of the GDP/GTP cycle, mediated by the action of RhoGAPs in the vicinity of the activated GTPases. RhoGAPs are more promiscuous, less interconnected in homotypic GAP/GAP complexes and localize on 'non-canonical' structures, such as the endoplasmic reticulum or mitochondria. These properties may contribute to a housekeeping function of the RhoGAPs, allowing them to create a barrier by which the signal is maintained in a steep gradient and prevented from leaking to the cell volume. RhoGDIs finally ensure the (re-)cycling of Rho GTPases through the confined activity zones. These mechanisms governing localized Rho signaling are fundamentally different from those in place in the Ras GTPase system, with only about 16 RasGEFs/RasGAPs with proven activity (Hennig et al., 2015). Here, spatial organization does not require the contribution of the opposing regulators but instead arises

from cycles of lipid anchoring and membrane release of the Ras proteins (Lorentzen et al., 2010; Rocks et al., 2010; Schmick et al., 2014).

Our family-wide characterization of the RhoGEF/RhoGAP regulatory proteins has generated multifaceted datasets on their enzymatic properties, spatial distribution and physical interactions. This integrated resource provides a basis by which the complexity of spatio-temporal control of Rho GTPase signaling can be further dissected and principles by which cells regulate their context-specific functions can be explored.

Supplemental Information

Supplemental Information includes 7 figures plus uncropped Western Blots, 4 tables and 2 data files. This and extended information can be found at Biostudies:S-BSST160 (McEntyre et al., 2015). The mass spectrometry proteomics data from the Q Exactive HF-X run have been deposited to the ProteomeXchange Consortium via the PRIDE (Vizcaíno et al., 2016) partner repository with the dataset identifier PXD010084. The rest of the mass spectrometry proteomics data have been deposited under the dataset identifier PXD010144.

Author Contributions

Conceptualization: P.M.M., R.D.B., T.P., E.P., and O.R.; Methodology: P.M.M. (FRET and TIRF screen), O.R., C.W. (confocal screen), R.D.B., K.M.A., V.N., M.S., M.T., O. Popp and B.L. (Mass Spectrometry), J.R. (case study, Cytochalasin D screen), L.E.H., R.D.B., P.M.M., O.R., C. Bakal, E.P. (computational methods), S.Z., L.S., L.B., G.M., T.R., K.F., J.R. and P.T. (library); Analysis: E.P., P.M.M., J.R., R.D.B. and O.R.; Software: E.P., G.G. and P.M.M.; Investigation: R.L.E., L.B., M.T.C., C. Barth, R.W.W. and P.T.; Data Curation: E.P., P.M.M., R.D.B., J.R. and O.R.; Resources: K.C. and O. Pertz; Writing: O.R. with contributions of E.P. and P.M.M; Partial Supervision and Project Administration: E.P., K.C., P.M., F.P.R. and T.P.; Supervision: O.R.

Acknowledgements

This work is dedicated to the memory of our dear mentor, Tony Pawson, without whom this study would not have been initiated. We thank O. Daumke, R. Hodge, D. Panakova and P. Bieling for critically reading the manuscript and R.D. Fritz for helpful discussions. We thank I. Laue, D. Heidler and the rest of the Rocks lab for technical assistance. We thank the MDC Advanced Light Microscopy Facility for technical assistance. This work was supported by the Human Frontier Science Program (LT000759/2008-L) (to O.R.), the CIHR Post-doctoral fellowship award (to R.D.B.), the Cancer Research UK (CRUK) Programme Foundation Award (C37275/A20146) and the Stand Up to Cancer campaign for Cancer Research UK (to C.B.),

Genome Canada through Ontario Genomics, the Ontario Government (ORF GL2-025) and the Terry Fox Research Institute (to T.P). Interaction proteomics at the Lunenfeld-Tanenbaum Research Institute was performed at the Network Biology Collaborative Centre, currently supported by Genome Canada and Ontario Genomics (OGI-139).F.P.R. and E.P. were supported by the Canada Excellence Research Chairs Program, the Krembil Foundation, the Avon Foundation and by the NIH/NHGRI Center of Excellence in Genomic Science program (HG004233).

References

Aghazadeh, B., Lowry, W.E., Huang, X.Y., and Rosen, M.K. (2000). Structural basis for relief of autoinhibition of the Dbl homology domain of proto-oncogene Vav by tyrosine phosphorylation. Cell *102*, 625–633.

Amin, E., Jaiswal, M., Derewenda, U., Reis, K., Nouri, K., Koessmeier, K.T., Aspenström, P., Somlyo, A.V., Dvorsky, R., and Ahmadian, M.R. (2016). Deciphering the Molecular and Functional Basis of RHOGAP Family Proteins: A SYSTEMATIC APPROACH TOWARD SELECTIVE INACTIVATION OF RHO FAMILY PROTEINS. J. Biol. Chem. *291*, 20353–20371.

Bakal, C., Aach, J., Church, G., and Perrimon, N. (2007). Quantitative morphological signatures define local signaling networks regulating cell morphology. Science *316*, 1753–1756.

Banerjee, J., Fischer, C.C., and Wedegaertner, P.B. (2009). The amino acid motif L/IIxxFE defines a novel actin-binding sequence in PDZ-RhoGEF. Biochemistry *48*, 8032–8043.

Benink, H.A., and Bement, W.M. (2005). Concentric zones of active RhoA and Cdc42 around single cell wounds. J. Cell Biol. *168*, 429–439.

Berriz, G.F., King, O.D., Bryant, B., Sander, C., and Roth, F.P. (2003). Characterizing gene sets with FuncAssociate. Bioinformatics *19*, 2502–2504.

Berriz, G.F., Beaver, J.E., Cenik, C., Tasan, M., and Roth, F.P. (2009). Next generation software for functional trend analysis. Bioinformatics *25*, 3043–3044.

Bos, J.L., Rehmann, H., and Wittinghofer, A. (2007). GEFs and GAPs: critical elements in the control of small G proteins. Cell *129*, 865–877.

Boulter, E., Garcia-Mata, R., Guilluy, C., Dubash, A., Rossi, G., Brennwald, P.J., and Burridge, K. (2010). Regulation of Rho GTPase crosstalk, degradation and activity by RhoGDI1. Nat. Cell Biol. *12*, 477–483.

Bravo-Cordero, J.J., Oser, M., Chen, X., Eddy, R., Hodgson, L., and Condeelis, J. (2011). A Novel Spatiotemporal RhoC Activation Pathway Locally Regulates Cofilin Activity at Invadopodia. Curr. Biol. *21*, 635–644.

Breitkreutz, A., Choi, H., Sharom, J.R., Boucher, L., Neduva, V., Larsen, B., Lin, Z.-Y., Breitkreutz, B.-J., Stark, C., Liu, G., et al. (2010). A global protein kinase and phosphatase interaction network in yeast. Science *328*, 1043–1046.

Canagarajah, B., Leskow, F.C., Ho, J.Y.S., Mischak, H., Saidi, L.F., Kazanietz, M.G., and Hurley, J.H. (2004). Structural mechanism for lipid activation of the Rac-specific GAP, beta2-chimaerin. Cell *119*, 407–418.

Cherfils, J., and Zeghouf, M. (2013). Regulation of small GTPases by GEFs, GAPs, and GDIs. Physiol. Rev. *93*, 269–309.

Choi, H., Larsen, B., Lin, Z.-Y., Breitkreutz, A., Mellacheruvu, D., Fermin, D., Qin, Z.S., Tyers, M., Gingras, A.-C., and Nesvizhskii, A.I. (2011). SAINT: probabilistic scoring of affinity purification-mass spectrometry data. Nat. Methods *8*, 70–73.

Cook, D.R., Rossman, K.L., and Der, C.J. (2014). Rho guanine nucleotide exchange factors: regulators of Rho GTPase activity in development and disease. Oncogene *33*, 4021–4035.

Colwill, K., Wells, C.D., Elder, K., Goudreault, M., Hersi, K., Kulkarni, S., Hardy, W.R., Pawson, T., and Morin, G.B. (2006). Modification of the Creator recombination system for proteomics applications--improved expression by addition of splice sites. BMC Biotechnol. *6*, 13.

Cox, J., and Mann, M. (2008). MaxQuant enables high peptide identification rates, individualized p.p.b.-range mass accuracies and proteome-wide protein quantification. Nat. Biotechnol. *26*, 1367–1372.

Devreotes, P., and Horwitz, A.R. (2015). Signaling networks that regulate cell migration. Cold Spring Harb. Perspect. Biol. *7*, a005959.

Eccles, R.L., Czajkowski, M.T., Barth, C., Müller, P.M., McShane, E., Grunwald, S., Beaudette, P., Mecklenburg, N., Volkmer, R., Zühlke, K., et al. (2016). Bimodal antagonism of PKA signalling by ARHGAP36. Nat. Commun. *7*, 12963.

Eddy, S.R. (2011). Accelerated Profile HMM Searches. PLoS Comput. Biol. *7*, e1002195.

Ellerbroek, S.M., Wennerberg, K., Arthur, W.T., Dunty, J.M., Bowman, D.R., DeMali, K.A., Der, C., and Burridge, K. (2004). SGEF, a RhoG guanine nucleotide exchange factor that stimulates macropinocytosis. Mol. Biol. Cell *15*, 3309–3319.

Ethier, M., Hou, W., Duewel, H.S., and Figeys, D. (2006). The proteomic reactor: a microfluidic device for processing minute amounts of protein prior to mass spectrometry analysis. J. Proteome Res. *5*, 2754–2759.

Finn, R.D., Coggill, P., Eberhardt, R.Y., Eddy, S.R., Mistry, J., Mitchell, A.L., Potter, S.C., Punta, M., Qureshi, M., Sangrador-Vegas, A., et al. (2016). The Pfam protein families database: towards a more sustainable future. Nucleic Acids Res. *44*, D279–D285.

Fritz, R.D., Letzelter, M., Reimann, A., Martin, K., Fusco, L., Ritsma, L., Ponsioen, B., Fluri, E., Schulte-Merker, S., van Rheenen, J., et al. (2013). A Versatile Toolkit to Produce Sensitive FRET Biosensors to Visualize Signaling in Time and Space. Sci. Signal. *6*, rs12–rs12.

Fritz, R.D., Menshykau, D., Martin, K., Reimann, A., Pontelli, V., and Pertz, O. (2015). SrGAP2-Dependent Integration of Membrane Geometry and Slit-Robo-Repulsive Cues Regulates Fibroblast Contact Inhibition of Locomotion. Dev. Cell *35*, 78–92.

Fukuhara, S., Chikumi, H., and Gutkind, J.S. (2000). Leukemia-associated Rho guanine nucleotide exchange factor (LARG) links heterotrimeric G proteins of the G(12) family to Rho. FEBS Lett. *485*, 183–188.

García-Mata, R., and Burridge, K. (2007). Catching a GEF by its tail. Trends Cell Biol. *17*, 36–43.

Garcia-Mata, R., Boulter, E., and Burridge, K. (2011). The “invisible hand”: regulation of RHO GTPases by RHOGDIs. Nat. Rev. Mol. Cell Biol. *12*, 493–504.

Guilluy, C., Garcia-Mata, R., and Burridge, K. (2011). Rho protein crosstalk: another social network? Trends Cell Biol. *21*, 718–726.

Hall, A. (1998). Rho GTPases and the Actin Cytoskeleton. Science *279*, 509–514.

Heasman, S.J., and Ridley, A.J. (2008). Mammalian Rho GTPases: new insights into their functions from in vivo studies. Nat. Rev. Mol. Cell Biol. *9*, 690–701.

Hennig, A., Markwart, R., Esparza-Franco, M.A., Ladds, G., and Rubio, I. (2015). Ras activation revisited: role of GEF and GAP systems. Biol. Chem. *396*, 831–848.

Hermjakob, H. (2004). IntAct: an open source molecular interaction database. Nucleic Acids Res. *32*, 452D – 455.

Hill, C.S., Wynne, J., and Treisman, R. (1995). The Rho family GTPases RhoA, Rac1, and CDC42Hs regulate transcriptional activation by SRF. Cell *81*, 1159–1170.

Hodge, R.G., and Ridley, A.J. (2016). Regulating Rho GTPases and their regulators. Nat. Rev. Mol. Cell Biol. *17*, 496–510.

Huang, D.W., Sherman, B.T., and Lempicki, R.A. (2009a). Systematic and integrative analysis of large gene lists using DAVID bioinformatics resources. Nat. Protoc. *4*, 44–57.

Huang, D.W., Sherman, B.T., and Lempicki, R.A. (2009b). Bioinformatics enrichment tools: paths toward the comprehensive functional analysis of large gene lists. Nucleic Acids Res. *37*, 1–13.

Jaffe, A.B., and Hall, A. (2005). Rho GTPases: biochemistry and biology. Annu. Rev. Cell Dev. Biol. *21*, 247–269.

Hubner, N.C., Bird, A.W., Cox, J., Splettstoesser, B., Bandilla, P., Poser, I., Hyman, A., and Mann, M. (2010). Quantitative proteomics combined with BAC TransgeneOmics reveals in vivo protein interactions. J. Cell Biol. *189*, 739–754.

Huttlin, E.L., Bruckner, R.J., Paulo, J.A., Cannon, J.R., Ting, L., Baltier, K., Colby, G., Gebreab, F., Gygi, M.P., Parzen, H., et al. (2017). Architecture of the human interactome defines protein communities and disease networks. Nature *545*, 505–509.

Jaiswal, M., Dvorsky, R., and Ahmadian, M.R. (2013). Deciphering the molecular and functional basis of Dbl family proteins: a novel systematic approach toward classification of selective activation of the Rho family proteins. J. Biol. Chem. *288*, 4486–4500.

Krendel, M., Zenke, F.T., and Bokoch, G.M. (2002). Nucleotide exchange factor GEF-H1 mediates cross-talk between microtubules and the actin cytoskeleton. Nat. Cell Biol. *4*, 294–301.

Krogh, A., Larsson, B., von Heijne, G., and Sonnhammer, E.L. (2001). Predicting transmembrane protein topology with a hidden Markov model: application to complete genomes. J. Mol. Biol. *305*, 567–580.

Lamarche-Vane, N., and Hall, A. (1998). CdGAP, a novel proline-rich GTPase-activating protein for Cdc42 and Rac. J. Biol. Chem. *273*, 29172–29177.

Laurin, M., and Cote, J.-F. (2014). Insights into the biological functions of Dock family guanine nucleotide exchange factors. Genes Dev. *28*, 533–547.

Lawson, C.D., and Ridley, A.J. (2018). Rho GTPase signaling complexes in cell migration and invasion. J. Cell Biol. *217*, 447–457.

Lee, J.-Y., Lee, L.-J., Fan, C.-C., Chang, H.-C., Shih, H.-A., Min, M.-Y., and Chang, M.-S. (2017). Important roles of Vilse in dendritic architecture and synaptic plasticity. Sci. Rep. *7*, 45646.

Letunic, I., and Bork, P. (2017). 20 years of the SMART protein domain annotation resource. Nucleic Acids Res. *46*, D493–D496.

Liu, G., Zhang, J., Larsen, B., Stark, C., Breitkreutz, A., Lin, Z.-Y., Breitkreutz, B.-J., Ding, Y., Colwill, K., Pasculescu, A., et al. (2010). ProHits: integrated software for mass spectrometry-based interaction proteomics. Nat. Biotechnol. *28*, 1015–1017.

Lorentzen, A., Kinkhabwala, A., Rocks, O., Vartak, N., and Bastiaens, P.I.H. (2010). Regulation of Ras localization by acylation enables a mode of intracellular signal propagation. Sci. Signal. *3*, ra68.

Machacek, M., Hodgson, L., Welch, C., Elliott, H., Pertz, O., Nalbant, P., Abell, A., Johnson, G.L., Hahn, K.M., and Danuser, G. (2009). Coordination of Rho GTPase activities during cell protrusion. Nature *461*, 99–103.

Martin, K., Reimann, A., Fritz, R.D., Ryu, H., Jeon, N.L., and Pertz, O. (2016). Spatio-temporal co-ordination of RhoA, Rac1 and Cdc42 activation during prototypical edge protrusion and retraction dynamics. Sci. Rep. *6*, 21901.

McEntyre, J., Sarkans, U., and Brazma, A. (2015). The BioStudies database. Mol. Syst. Biol. *11*, 847.

Mellacheruvu, D., Wright, Z., Couzens, A.L., Lambert, J.-P., St-Denis, N.A., Li, T., Miteva, Y.V., Hauri, S., Sardiu, M.E., Low, T.Y., et al. (2013). The CRAPome: a contaminant repository for affinity purification-mass spectrometry data. Nat. Methods *10*, 730–736.

Miller, A.L., and Bement, W.M. (2009). Regulation of cytokinesis by Rho GTPase flux. Nat. Cell Biol. *11*, 71–77.

Mitin, N., Betts, L., Yohe, M.E., Der, C.J., Sondek, J., and Rossman, K.L. (2007). Release of autoinhibition of ASEF by APC leads to CDC42 activation and tumor suppression. Nat. Struct. Mol. Biol. *14*, 814–823.

Murtagh, F., and Legendre, P. (2014). Ward's Hierarchical Agglomerative Clustering Method: Which Algorithms Implement Ward's Criterion? J. Classification *31*, 274–295.

Okabe, T., Nakamura, T., Nishimura, Y.N., Kohu, K., Ohwada, S., Morishita, Y., and Akiyama, T. (2003). RICS, a novel GTPase-activating protein for Cdc42 and Rac1, is involved in the beta-catenin-N-cadherin and N-methyl-D-aspartate receptor signaling. J. Biol. Chem. *278*, 9920–9927.

O'Leary, N.A., Wright, M.W., Brister, J.R., Ciufo, S., Haddad, D., McVeigh, R., Rajput, B., Robbertse, B., Smith-White, B., Ako-Adjei, D., et al. (2016). Reference sequence (RefSeq) database at NCBI: current status, taxonomic expansion, and functional annotation. Nucleic Acids Res. *44*, D733–D745.

Orchard, S., Ammari, M., Aranda, B., Breuza, L., Briganti, L., Broackes-Carter, F., Campbell, N.H., Chavali, G., Chen, C., del-Toro, N., et al. (2013). The MIntAct project—IntAct as a common curation platform for 11 molecular interaction databases. Nucleic Acids Res. *42*, D358–D363.

Parsons, J.T., Horwitz, A.R., and Schwartz, M.A. (2010). Cell adhesion: integrating cytoskeletal dynamics and cellular tension. Nat. Rev. Mol. Cell Biol. *11*, 633–643.

Pertz, O., Hodgson, L., Klemke, R.L., and Hahn, K.M. (2006). Spatiotemporal dynamics of RhoA activity in migrating cells. Nature *440*, 1069–1072.

Pertz, O. (2010). Spatio-temporal Rho GTPase signaling - where are we now? J. Cell Sci. *123*, 1841–1850.

Petsalaki, E.I., Bagos, P.G., Litou, Z.I., and Hamodrakas, S.J. (2006). PredSL: a tool for the N-terminal sequence-based prediction of protein subcellular localization. Genomics Proteomics

Bioinformatics *4*, 48–55.

Porter, A.P., Papaioannou, A., and Malliri, A. (2016). Deregulation of Rho GTPases in cancer. Small GTPases *7*, 123–138.

Rappsilber, J., Ishihama, Y., and Mann, M. (2003). Stop and go extraction tips for matrix-assisted laser desorption/ionization, nanoelectrospray, and LC/MS sample pretreatment in proteomics. Anal. Chem. *75*, 663–670.

Rocks, O., Gerauer, M., Vartak, N., Koch, S., Huang, Z.-P., Pechlivanis, M., Kuhlmann, J., Brunsveld, L., Chandra, A., Ellinger, B., et al. (2010). The palmitoylation machinery is a spatially organizing system for peripheral membrane proteins. Cell *141*, 458–471.

Rojas, R.J., Yohe, M.E., Gershburg, S., Kawano, T., Kozasa, T., and Sondek, J. (2007). GαqDirectly Activates p63RhoGEF and Trio via a Conserved Extension of the Dbl Homology-associated Pleckstrin Homology Domain. J. Biol. Chem. *282*, 29201–29210.

Rossman, K.L., Der, C.J., and Sondek, J. (2005). GEF means go: turning on RHO GTPases with guanine nucleotide-exchange factors. Nat. Rev. Mol. Cell Biol. *6*, 167–180.

Russell, J., and Cohn, R. (2012). Cytoscape (Book on Demand Limited).

Schaefer, A., Reinhard, N.R., and Hordijk, P.L. (2014). Toward understanding RhoGTPase specificity: structure, function and local activation. Small GTPases *5*, 6.

Schaefer, M.H., Fontaine, J.-F., Vinayagam, A., Porras, P., Wanker, E.E., and Andrade-Navarro, M.A. (2012). HIPPIE: Integrating protein interaction networks with experiment based quality scores. PLoS One *7*, e31826.

Schliwa, M. (1982). Action of cytochalasin D on cytoskeletal networks. J. Cell Biol. *92*, 79–91.

Schmick, M., Vartak, N., Papke, B., Kovacevic, M., Truxius, D.C., Rossmannek, L., and Bastiaens, P.I.H. (2014). KRas localizes to the plasma membrane by spatial cycles of solubilization, trapping and vesicular transport. Cell *157*, 459–471.

Shang, X., Zhou, Y.T., and Low, B.C. (2003). Concerted regulation of cell dynamics by BNIP-2 and Cdc42GAP homology/Sec14p-like, proline-rich, and GTPase-activating protein domains of a novel Rho GTPase-activating protein, BPGAP1. J. Biol. Chem. *278*, 45903–45914.

Simpson, J.C., Wellenreuther, R., Poustka, A., Pepperkok, R., and Wiemann, S. (2000). Systematic subcellular localization of novel proteins identified by large-scale cDNA sequencing. EMBO Rep. *1*, 287–292.

Smoly, I., Shemesh, N., Ziv-Ukelson, M., Ben-Zvi, A., and Yeger-Lotem, E. (2017). An Asymmetrically Balanced Organization of Kinases versus Phosphatases across Eukaryotes Determines Their Distinct Impacts. PLoS Comput. Biol. *13*, e1005221.

So, J., Pasculescu, A., Dai, A.Y., Williton, K., James, A., Nguyen, V., Creixell, P., Schoof, E.M., Sinclair, J., Barrios-Rodiles, M., et al. (2015). Integrative analysis of kinase networks in TRAIL-induced apoptosis provides a source of potential targets for combination therapy. Sci. Signal. *8*, rs3.

St-Denis, N., Gupta, G.D., Lin, Z.Y., Gonzalez-Badillo, B., Veri, A.O., Knight, J.D.R., Rajendran, D., Couzens, A.L., Currie, K.W., Tkach, J.M., et al. (2016). Phenotypic and Interaction Profiling of the Human Phosphatases Identifies Diverse Mitotic Regulators. Cell Rep. *17*, 2488–2501.

Sternweis, P.C., Carter, A.M., Chen, Z., Danesh, S.M., Hsiung, Y.-F., and Singer, W.D. (2007). Regulation of Rho guanine nucleotide exchange factors by G proteins. Adv. Protein Chem. *74*, 189–228.

Sterpetti, P., Hack, A.A., Bashar, M.P., Park, B., Cheng, S.D., Knoll, J.H., Urano, T., Feig, L.A., and Toksoz, D. (1999). Activation of the Lbc Rho exchange factor proto-oncogene by truncation of an extended C terminus that regulates transformation and targeting. Mol. Cell. Biol. *19*, 1334–1345.

Struckhoff, A.P., Rana, M.K., Kher, S.S., Burow, M.E., Hagan, J.L., Del Valle, L., and Worthylake, R.A. (2013). PDZ-RhoGEF is essential for CXCR4-driven breast tumor cell motility through spatial regulation of RhoA. J. Cell Sci. *126*, 4514–4526.

Tcherkezian, J., and Lamarche-Vane, N. (2007). Current knowledge of the large RhoGAP family of proteins. Biol. Cell *99*, 67–86.

Thul, P.J., Åkesson, L., Wiking, M., Mahdessian, D., Geladaki, A., Ait Blal, H., Alm, T., Asplund, A., Björk, L., Breckels, L.M., et al. (2017). A subcellular map of the human proteome. Science *356*.

Vizcaíno, J.A., Csordas, A., del-Toro, N., Dianes, J.A., Griss, J., Lavidas, I., Mayer, G., Perez-Riverol, Y., Reisinger, F., Ternent, T., et al. (2016). 2016 update of the PRIDE database and its related tools. Nucleic Acids Res. *44*, D447–D456.

Wang, Y., Kelber, J.A., Cao, H.S.T., Cantin, G.T., Lin, R., Wang, W., Kaushal, S., Bristow, J.M., Edgington, T.S., Hoffman, R.M., et al. (2010). Pseudopodium-enriched atypical kinase 1 regulates the cytoskeleton and cancer progression. Proceedings of the National Academy of Sciences *107*, 10920–10925.

Wells, C.D., Fawcett, J.P., Traweger, A., Yamanaka, Y., Goudreault, M., Elder, K., Kulkarni, S., Gish, G., Virag, C., Lim, C., et al. (2006). A Rich1/Amot Complex Regulates the Cdc42 GTPase and Apical-Polarity Proteins in Epithelial Cells. Cell *125*, 535–548.

Wells, C.D., Gutowski, S., Bollag, G., and Sternweis, P.C. (2001). Identification of potential mechanisms for regulation of p115 RhoGEF through analysis of endogenous and mutant forms of the exchange factor. J. Biol. Chem. *276*, 28897–28905.

Wenger, C.D., Phanstiel, D.H., Lee, M.V., Bailey, D.J., and Coon, J.J. (2011). COMPASS: a suite of pre- and post-search proteomics software tools for OMSSA. Proteomics *11*, 1064–1074.

Yagi, H., Tan, W., Dillenburg-Pilla, P., Armando, S., Amornphimoltham, P., Simaan, M., Weigert, R., Molinolo, A.A., Bouvier, M., and Gutkind, J.S. (2011). A synthetic biology approach reveals a CXCR4-G13-Rho signaling axis driving transendothelial migration of metastatic breast cancer cells. Sci. Signal. *4*, ra60.

Yu, G., and He, Q.-Y. (2016). ReactomePA: an R/Bioconductor package for reactome pathway analysis and visualization. Mol. Biosyst. *12*, 477–479.

Zaidel-Bar, R., Itzkovitz, S., Ma'ayan, A., Iyengar, R., and Geiger, B. (2007). Functional atlas of the integrin adhesome. Nat. Cell Biol. *9*, 858–867.

STAR*METHODS

CONTACT FOR REAGENT AND RESOURCE SHARING

Requests for further information and resources and reagents should be directed to the Lead Contact Oliver Rocks (oliver.rocks@mdc-berlin.de).

EXPERIMENTAL MODEL AND SUBJECT DETAILS

Mammalian cell culture

Human embryonic kidney (HEK293T, ATCC number: CRL-3216) cells were cultured in Dulbecco's modified Eagle medium (DMEM) containing 10% fetal bovine serum (FBS) and 1% Penicillin/Streptomycin (37°C, 5% CO2) and transfected using polyethylenimine (PEI) dissolved in Opti-MEM. RhoGDI-knockdown HEK293T cells were generated by infection of cells for 24 h with lentiviral shRNA targeting RhoGDI and selection with puromycin (2 µg/ml). MDCK II canine kidney cells were cultured in modified Eagle medium (MEM) containing 10% FBS and 1% Penicillin/Streptomycin and transfected using Effectene (Qiagen). COS-7 cells were cultured in DMEM supplemented with 10% FBS and 1% Penicillin/Streptomycin (37°C, 5% CO2) and transfected using Lipofectamine 3000. The mCherry-Paxillin COS-7 reporter cell line was generated by infection of cells with a lentivirus encoding a Gateway system mCherry-Paxillin expression construct under the control of the Ubiquitin C (UbC) promoter (provided by Alexander Löwer, TU Darmstadt).

METHOD DETAILS

Cloning of RhoGEF/GAP cDNA expression library

We extracted the human proteome from SwissProt/Uniprot (UniProt, 2015), and scanned all sequences using the Pfam (Finn et al., 2016) HMM models for the RhoGAP, RhoGEF and DHR-2 domains and the hmmsearch function from the HMMER package (Eddy, 2011). We identified 145 RhoGAP and GEF proteins in total. Specifically, 68 proteins contain a RhoGEF domain, 64 contain a RhoGAP domain, 2 contain both a RhoGEF and RhoGAP domain and 11 contain a DHR2 domain. 141 full-length cDNAs were curated through the MGC/ORFeome collection, the Kazusa DNA Research Institute collection, gene synthesis (33 cDNAs, GenScript), the contribution by authors of previously published materials and cloning from cDNA libraries. cDNAs encoding OBSCN (~8000a.a.), ARHGEF33, ARHGEF37 and ARHGEF38 are not included in our collection. 116 of the 141 cDNAs in the library match the longest predicted isoform. The remaining 26 cDNAs represent slightly shorter forms which, on average, lack only 3% of the full-length size, with a maximum difference of 17%. cDNAs were from human (112), mouse (26), rat (2) and chimpanzee (1) genes. Expression libraries of mCitrine-YFP and mCherry fusion proteins were generated using a modified Creator donor plasmid system as previously described (Colwill et al., 2006). Briefly, cDNA inserts were amplified by PCR to be flanked by rare-cutting AscI and PacI restriction enzyme sites, digested and cloned into Donor Vectors (V7, V37). Expression constructs of five cDNAs were generated using the Gateway system

(ThermoFisher Scientific). Since approximately 40% of the RhoGEFs contain a PSD95-Dlg1-ZO1 (PDZ) domain-binding motif at the C-terminus, which might be involved in protein-protein interactions (García-Mata and Burridge, 2007), we have ensured that the set of N-terminally tagged vectors maintain their natural C-termini and introduced a stop codon into the respective PacI sites. Donor constructs were then recombined using Cre recombinase into 3xFLAG, mCitrine-YFP and mCherry acceptor vectors as previously described (Colwill et al., 2006). Sequences of the expression vectors can be found in Supplementary Data 1. All mutation and deletion constructs were created by site-directed mutagenesis (Agilent Technologies).

Lysis, immunoprecipitation & Western blotting

HEK293T cell pellets were lysed in NP40 lysis buffer (1% NP40, 20mM Tris-HCL pH 7.5, 150mM NaCl, 1mM EGTA, 5mM NaF) with cOmplete protease inhibitor cocktail (Roche) and N-ethylmaleimide (NEM, Sigma). For immunoprecipitation (IP), cleared lysates were added to either FLAG-M2 affinity gel (Sigma) or Protein G Sepharose beads (Sigma) coupled with anti-GFP (ab290, Abcam, 0.5 µl per 10 cm plate). After minimum 1 h rotation at 4°C, beads were washed three times in lysis buffer and eluted with Laemmli buffer. The following antibodies were used for Western blotting: FLAG (Sigma, M2, 1:5,000), GFP (Abcam, ab290, 1:10,000), RhoGDI (Santa Cruz, sc360, 1:2000), Tubulin (Sigma, DM1a, 1:10,000) and Cherry (abcam, ab125096, 1:2000). Protein bands were detected either by chemiluminescence or using the Li-COR Odyssey imaging system (LI-COR Biosciences).

FRET biosensor specificity screen

Literature review of RhoGEF/GAP specificities

We reviewed over 450 publications in which claims on catalytic activities of RhoGEFs and RhoGAPs towards RhoA, Rac1 and Cdc42 had been made and extracted information about the identified target GTPase(s) and the method used in the study. While some regulators have been characterized in multiple reports, for others, minimal data is available. 14 regulators have not been studied at all and for 28 not all three Rho proteins were analyzed. The resulting primary specificity list in which we integrated all reported activities of each regulator towards each of the three GTPases revealed a high degree of conflicting data. We hypothesized that the use of *in vitro* and *in vivo* methods is a major reason for controversial results (see discussion). Additional discrepancies may arise from the use of cellular 'pull-down' methods, which suffer from poor reproducibility due to the fast GTP hydrolysis that occurs during sample processing. We therefore generated separate datasets for activities detected *in vitro* and *in vivo* and, in addition, introduced selection criteria to further increase the significance of the specificity catalogue. An entry of a particular regulator in the list ('activity' or 'no activity' towards either RhoA, Rac1 or Cdc42) was only accepted either if no conflicting study exists (that is, a study

showing opposite results for the activity of a particular regulator towards a particular GTPase) or if a conflicting report could be overruled by three consistent studies (3:1 rule). Using this filter, we finally compiled four datasets: two separate *in vitro* and *in vivo* substrate specificity lists, a "gold standard" list that only includes matching activities from these two lists and, for comparison, an 'integrated' list with all reported activities combined, irrespective of the method used. The gold standard list shows an overall agreement of 70% with our specificity screen data (Table S2).

Establishment of the FRET-based assay

Overexpressed Rho biosensors exhibit an elevated basal activity due to the saturation of endogenous RhoGDIs, resulting in the accumulation of the reporter at membranes where abundant activation by endogenous RhoGEFs occurs. To increase the dynamic range of the sensors in response to activation and inactivation by RhoGEFs and RhoGAPs, we adjusted the cellular RhoGDI levels (Boulter et al., 2010; Pertz et al., 2006). Titration experiments revealed that a 2-fold excess of coexpressed RhoGDI plasmid over the sensor plasmids reestablished their low basal activity without saturating the system with RhoGDI (Figure S1A). This plasmid ratio was therefore used in the subsequent RhoGEF screen. Conversely, shRNA-mediated stable knockdown of RhoGDI even further increased the elevated basal activity level of the transfected sensors (Figure S1B) and consequently the dynamic range to detect inactivation by coexpressed RhoGAPs (Figure S1C). We thus used stable RhoGDI-knockdown HEK293T cells (shRNA#2) in all RhoGAP activity assays in this study. We also confirmed the robustness of the assay to technical and biological variability of sensor expression (Figure S1D). Based on this data, we used 30 ng sensor plasmid for the RhoGAP screen and 40 ng sensor plasmid for the RhoGEF screen. Another control experiment revealed that already minimal amounts of coexpressed RhoGEF or RhoGAP plasmid can substantially activate or inactivate all biosensors, respectively (Figure S1E,F). However, to ensure reliable detection also of RhoGEFs and RhoGAPs with lower catalytic activities, we used an excess of regulator plasmids over sensors plasmids: For the RhoGEF screen a 1:2:7 ratio of sensor:RhoGDI:RhoGEF was used and for the RhoGAP screen, a 1:9 ratio of sensor:RhoGAP was used. As judged by the respective mCherry intensities, the expression levels of the RhoGEFs and RhoGAPs in the screen were always higher than the levels that were required for the minimal detectable significant FRET sensor response.

Sample preparation for specificity screen

Wild type HEK293T cells and stable RhoGDI-knockdown HEK293T cells were cultured in poly-L-lysine-coated (25 ng/µl) microscopic 96-well plates (µ-Plate, ibidi) and kept in a custom-made humidity chamber inside a standard cell culture incubator with humidification system. Cells

were seeded in 250 µl FluoroBrite DMEM supplemented with 10% FBS and 100 U/ml Penicillin/Streptomycin at a density of 5.5 x 10^4 cells per well and allowed to adhere overnight. Before transfection, medium was replaced with fresh medium. For the RhoGEF specificity screen, cells were transfected with 40 ng FRET sensor, 80 ng RhoGDI or mCherry control, and 280 ng RhoGEF or mCherry control. For the RhoGAP specificity screen, cells were transfected with 30 ng FRET sensor and 270 ng RhoGAP or mCherry control. DNA was mixed with PEI transfection reagent (1 mg/ml, pH 7) at a ratio of 1:3 (DNA [µg] : PEI [µl]), incubated for 20 min, and thoroughly mixed by repeated pipetting before adding to the cells. One day after transfection, the medium was replaced with 300 µl FluoroBrite DMEM supplemented with 1% FBS. Cells were imaged 48 h post transfection.

For autoinhibition experiments, the amount of transfected plasmid of two of the investigated RhoGEF short isoforms was reduced to adjust their expression levels to the lower levels of the corresponding longer isoforms: ARHGEF5 isoform2 (60 ng), ARHGEF16 isoform2 (70 ng) levels were filled to 280 ng with miRFP670 empty vector.

For PLEKHG4B/ARHGEF11/ARHGEF12 co-regulation FRET experiments, cells were transfected with 40 ng FRET sensor, 80 ng RhoGDI or mCherry control, 140 ng mCherry labeled RhoGEF or mCherry control and 140 ng miRFP670 labeled RhoGEF mutants/ truncations or miRFP670 control. Regulators tested for autoinhibition were selected randomly.

Ratiometric FRET microscopy

FRET experiments were performed on a fully automated Olympus IX81 inverted epifluorescence microscope equipped with an UPLSAPO 10x/0.4 NA air objective, an MT20 150W xenon arc burner light source (Olympus) with an excitation filter wheel, a motorized dichroic mirror turret, and an emission filter wheel. Furthermore, the microscope was equipped with a motorized programmable stage (Märzhäuser Wetzlar) and a near-infrared laser-based autofocus system that allowed automated image acquisition of 96-well plates. Images were acquired with a water-cooled EMCCD camera (Hamamatsu) at a 16-bit depth. A temperature-controlled incubation chamber maintained 37°C, 5% CO2 and 60% humidity during the experiments. The following combinations of excitation filters (Ex), dichroic mirrors (DM) and emission filters (Em) were used: donor channel Ex: 430/25 DM: zt442RDC Em: 483/32; FRET-acceptor channel Ex: 430/25 DM: zt442RDC Em: 542/27; acceptor/mVenus channel Ex: 500/20 DM: zt514RDC Em: 542/27; mCherry channel Ex: 572/23 DM: HC BS 593 Em: 623/24; miRFP670 channel Ex: 640/30 DM: R405/488/561/635 Em: 692/40. Five fields of view were imaged for each condition in each of the above channels and transmission light channel. Microscopic images were processed and quantified as described in QUANTIFICATION AND STATISTICAL ANALYSIS.

High Content Imaging experimental details

Immunostaining Cells

COS-7 cells were plated in duplicate in 384-well plates and transfected with mCitrine-tagged RhoGEF/GAP constructs or empty YFP vector. Cells were fixed and permeabilized by the addition of 0.2% Triton X-100/PBS (phosphate-buffered saline) for 15 min. After washing 3 times in PBS, cells were incubated in 0.5% FBS/PBS for 1 h. Cells were washed 3 times in PBS before incubation with primary antibodies mouse anti-alphaTubulin (ThermoFisher Scientific A11126, 1:1000) and rabbit anti-GFP (Molecular Probes A11122,1:5000) in 0.5% FBS/PBS overnight at 4°C. Cells were washed 3 times in PBS before incubation with secondary antibodies Alexa Fluor647 goat anti-mouse (Molecular Probes A21237, 1:500) and Alexa Fluor488 goat anti-rabbit (Molecular Probes A11008, 1:500) in 0.5% FBS/PBS for 1 h. Cells were washed a further 3 times in PBS before incubation with 10μg/ml DAPI/PBS (ThermoFisher Scientific D1306) for 15 min and a final 2 washes in PBS. All steps were performed at room temperature.

Image Acquisition and Analysis

Cells were imaged at 20X using the Opera High Content Screening System (Perkin Elmer). 35-40 images were acquired per well (Biostudies:S-BSST160). Columbus image analysis software (Perkin Elmer) was used to automatically segment images and detect cells. In brief, nuclei and cell cytoplasm were detected using DAPI and alpha-tubulin staining. Poorly segmented or incompletely imaged cells were filtered out and transfected cells were identified according to the intensity of anti-GFP staining in the cytoplasm or nucleus. 236 features quantitatively describing cell and nuclear morphology, DAPI, alpha-tubulin and GFP staining intensities and textures of transfected cells were then calculated (Biostudies:S-BSST160).

Phenotypic Data Analysis

Wells containing below 1% transfected cells were removed from further analysis. Moreover, cells with bait expression deviating from the mean by more than two standard deviations were removed from further analysis to avoid bias from extreme data points. Well means for each feature for each treatment were then compared to control wells containing a YFP-only vector using Z scores (Z = (well mean score – control well mean score) / control well SD; Biostudies:S-BSST160).

In total, we measured 234 phenotypic features, many of which were redundant. To reduce redundancy, we performed hierarchical clustering of the features using 1-Pearson correlation as a distance and cut the tree at the point where the distance between trees was greater than 0.6. Then within the features in the same clusters, we kept the one that had the maximum

distance from the other clusters (Biostudies:S-BSST160). We performed the analysis separately for GAPs and GEFs. For each bait, we removed it from the set and performed the following procedure: We first created phenotypic profiles for each of RhoA-, Rac1- and Cdc42- specific baits. We then calculated the Pearson correlation of the bait that was left out with its respective phenotypic profile.

Localization study experimental details

Confocal microscopy

MDCK cells seeded on glass bottom dishes (MatTek) were live-imaged 24 h post transfection on a Fluoview 1000 confocal microscope (Olympus) equipped with a UPLSAPO_60/1.3 numerical aperture silicon immersion oil immersion lens. Images were taken with the following excitation (Ex) and emission (Em) settings: Hoechst Ex: 405 nm diode laser (50 mW) Em: 425–475 nm; mCerulean-CFP Ex: 440 nm diode laser (25 mW) Em: 460–500 nm; GFP, AlexaFluor488 Ex: Multi-Line Argon laser 488 nm (40 mW) Em: 500–545 nm; mCitrine-YFP, Venus-YFP Ex: Multi-Line Argon laser 515 nm (40 mW) Em: 530–545 nm; AlexaFluor555 Ex: 559 nm diode laser (20 mW) Em: 570–625 nm; mCherry Ex: 559 nm diode laser (20 mW) Em: 575–675 nm; AlexaFluor647 Ex: 635 nm diode laser (20 mW) Em: 655–755 nm. Images were also acquired using a Nikon/Andor CSU-W spinning disk microscope equipped with a 100x Oil CFI P-Apo λ /NA 1.45/WD 0.13 objective and an Andor iXON DU-888 EMCCD. The following excitation (Ex) and emission (Em) settings were used: mCerulean-CFP Ex: 445 nm laser (75 mW) Em: 460-500 nm; mCitrine-YFP Ex: 514 nm laser (40 mW) Em: 542-576 nm; mCherry Ex: 561 nm laser (100 mW) Em: 582-636 nm; AlexaFluor647 Ex 637 nm laser (140 mW) Em: 665-705 nm.

TIRF microscopy screen

Stable mCherry-paxillin COS-7 cells or wild type COS-7 were reverse transfected using Lipofectamine 3000 and seeded on glass bottom dishes (MatTek). Images were taken 15 - 20 h post transfection on an Olympus IX81 microscope equipped with an APON 60x/1.49 NA oil immersion TIRF objective and a motorized 4-line TIRF condenser (Olympus) to achieve TIRF illumination. Images were taken with a water-cooled EMCCD camera (Hamamatsu) at a 16-bit depth. Images were taken with the following excitation (Ex) and emission (Em) settings: mCitrine and mEGFP Ex: 488 nm solid state laser Em: 525/50; mCherry Ex: 561 nm solid state laser Em: 617/73; miRFP Ex: 640 nm diode laser Em: 692/40. A temperature-controlled incubation chamber maintained 37 °C, 5% CO2, and 60% humidity during the experiments. Line scans to determine fluorescence intensity profiles were generated using ImageJ software. The "plot profile" tool was used to create a graph of pixel intensity plotted over the distance along the line. To reduce noise, pixel intensity was averaged on a line width of 3 pixels. Intensity was

normalized to the average intensity along the selection to maintain relative intensity proportions.

Cytochalasin D assay

MDCK cells seeded on glass coverslips and transiently transfected with Citrine-tagged RhoGEF/RhoGAP library constructs were treated for 30 min at 37°C with 50 µM Cytochalasin D (Focus Biomolecules), fixed with 4% paraformaldehyde for 10 min, permeabilized with 0.2% Triton X-100/100mM glycine for 10 min and blocked for 20 min in 3% bovine serum albumin. GFP primary antibody (Abcam, ab13970) incubation was performed for 1 h at room temperature or at 4°C overnight and Alexa Fluor secondary antibodies (Molecular Probes, 1:1,000) were incubated for 30 min each. CF568 Phalloidin conjugate (Biotium) was used to stain actin filaments and was added to the secondary antibody mixture. Coverslips were mounted using ProLong Gold (Invitrogen). We validated this approach by showing that it reliably revealed all 12 regulators that had been found to colocalize with actin in the primary screen, and additionally a set of known actin-associated proteins. No co-aggregation was observed for negative control proteins such as NEFL, GalT or EEA1, known either to be cytosolic or to localize to other compartments (Figure S4C). In Cytochalasin D treated cells, we also detected a clear co-aggregation of ARHGEF11, a RhoGEF that associates with actin filaments but is not detectable through microscopy. This did not occur with a mutant deficient in actin binding (Banerjee et al., 2009)

RhoGEF/GAP interactome acquisition & analysis

Sample preparation and mass spectrometry

We used 3xFLAG- and mCitrine YFP-tagged RhoGAP and RhoGEF expression plasmids to eliminate bias for prey interactions inherent in either epitope tag. These were transiently transfected into HEK293T cells using polyethylenimine (PEI) and, as an additional experiment, mCitrine YFP-tagged RhoGEFs/GAPs constructs were stably integrated (selection marker G418) in HEK293T cells. Cells from 2 x 150 mm plates were lysed in NP40 lysis buffer supplemented with 10% glycerol, 10 mM sodium pyrophosphate, 10 µg/ml aprotinin, pepstatin and leupeptin, 100µM $NaVO_4$, 1mM phenylmethylsulfonyl fluoride, 1:1000 phosphatase inhibitor cocktail II (Calbiochem), calyculin A and benzonase, and the lysate was clarified by centrifugation at 20.000xg for 10 min. Bait proteins and associated polypeptides were isolated from the supernatant by adding 30 µl packed anti-FLAG M2 (Sigma) or 15 ul packed GFP-trap (Chromotek) sepharose beads and nutating at 4°C for 1 hour. Beads were washed 2x with lysis buffer and 1-2x with 20 mM Hepes pH 7.5. Proteins were then eluted three times with 50 mM phosphoric acid pH 1.8 for 5-10 min each. Samples were processed using a solid-phase digest protocol using proteomic reactors (Ethier et al. 2006; So et al. 2015) or spin-tips. For the

proteomic reactor, 3 cm of PolySulfoethyl A beads (particle size, 12 mm; pore size, 300 Å) (Western Analytical) was packed into 200-mm (internal diameter) fused silica tubing using a pressure bomb (nitrogen gas, 100 to 500 psi). Protein eluates were loaded on the column and washed with 10 mM potassium phosphate buffer (pH 3) and high-performance liquid chromatography (HPLC)–grade water. Bound proteins were reduced in DTT solution (100 mM DTT/10 mM ammonium bicarbonate pH 8) for 30 min and washed with HPLC-grade water. Reduced proteins were alkylated and trypsin-digested for 1 to 2 h in trypsin solution [sequencing-grade porcine trypsin (2 mg/ml; Promega)/100 mM Tris/10 mM iodoacetamide (pH 8)]. Peptides were eluted in 15 μl of 200 mM ammonium bicarbonate pH 8, and 1 μl of 50% formic acid was added to a final volume of 16 μl. For the spin tip method, steps were adapted from the column method of the proteomic reactor, with 30μm SCX beads (PolyLC) packed into a TopTip (Glygen). Centrifugal force (1000xg) was used to load samples, buffer exchange and add reagents to the immobilized proteins. Buffers, reagents and volumes closely followed the steps in the proteomic reactor, using adapters and Eppendorf tubes to recover flow through and final digested peptides. A subset of samples (search tasks #285 and 748) were digested 'on-bead' (Supplementary Data 2). Beads used for immunoprecipitations were resuspended in 50 mM ammonium bicarbonate pH 8 with 1μg of trypsin without an elution step. These samples were incubated overnight at 37°C on a rotating disc. An additional 0.5 μg of trypsin in 50 mM ammonium bicarbonate pH 8 was then added and samples were incubated for 2 h at 37°C with mixing. Beads were centrifuged at 400 x g for 1 min and the supernatant was transferred to a fresh 1.5 mL microfuge tube. Beads were rinsed twice with HPLC-grade water and the rinses were added to the original supernatant. These samples were acidified to 2% formic acid and dried in a centrifugal evaporator before being resuspended in 5% formic acid.

Digested samples were processed on a ThermoFisher LTQ linear ion trap, ThermoFisher LTQ-Orbitrap or SCIEX TripleTOF 5600 as indicated in Supplementary Data 2. Sample data generated by nanoLC-MS/MS on Thermo LTQs was acquired using a home-packed 75μm ID emitter tip column with 10cm of 3.5μm Zorbax C18. The gradient was delivered in a split-flow manner by an Agilent 1100 Capillary HPLC, or with flow control using an Agilent 1100 Nano HPLC. A gradient length of 100 minutes was used, during which time the amount of acetonitrile was started at 2% and increased from 2-35% between 8-65 minutes, from 35%-50% between 65-75 minutes, from 50%-80% between 75-80 minutes and held at 80% for 5 minutes. From 85-100 minutes, the HPLC was reset to deliver 2% acetonitrile. Data was acquired using a data-dependent method consisting of 1 MS scan followed by 4 MS/MS scans. After peptide ions were selected for MS/MS, they were added to a dynamic exclusion list for 30 sec. After each sample analysis gradient, four wash gradients were performed, which began with sequential injection through the autosampler loop of isopropanol, 2% TFA, acetonitrile or

0.1% formic acid, respectively. Each wash gradient consisted of 3 oscillations from 30% to 60% acetonitrile over 45 minutes. Following the wash steps, 50 fmol of digested BSA protein was injected and analyzed with a 30 min gradient prior to the next sample analysis. Under these conditions carry-over was minimal, but was nevertheless tracked to ascertain absence of contaminants from the prior sample run. Sample data generated by nanoLC-MS/MS with an Orbitrap were analyzed using an Eksigent nanoLC Ultra 1Dplus to deliver the gradient. Peptides were directly loaded onto a 75µm x 10cm packed tip (Zorbax C18) and eluted at 200 nL/min matching the 100 minute gradient described above. Data was acquired in a data-dependent manner with a high resolution MS scan (60000 resolution) followed by 3 MS/MS LTQ scans. The injection cycle of sample, wash gradients and BSA test was the same as for the LTQ. For the nanoLC-MS/MS on a TripleTOF 5600, samples were directly loaded by a NanoLC-Ultra 1D plus (Eksigent, Dublin CA) nano-pump at 400 nL/min onto a 75 µm × 12 cm emitter packed with 3 µm ReproSil-Pur C_{18}-AQ (Dr. Maisch HPLC GmbH, Germany). The gradient was delivered at 200 nL/min starting from 2% acetonitrile with 0.1% formic acid to 35% acetonitrile with 0.1% formic acid over 90 minutes followed by a 15 min clean-up at 80% acetonitrile with 0.1% formic acid, and a 15 min equilibration period back to 2% acetonitrile with 0.1% formic acid for a total of 120 min. To minimize carryover between each sample, the analytical column was washed for 3 hours by running an alternating sawtooth gradient from 35% acetonitrile with 0.1% formic acid to 80% acetonitrile with 0.1% formic acid, holding each gradient concentration for 5 min. Analytical column and instrument performance were verified after each sample by loading 30 fmol BSA tryptic peptide standard (Michrom Bioresources Inc. Fremont, CA) with 60 fmol α-Casein tryptic digest and running a short 30 min gradient. TOF MS calibration was performed on BSA reference ions before running the next sample in order to adjust for mass drift and to verify peak intensity. The instrument method was set to a discovery or IDA mode which consisted of one 250 ms MS1 TOF survey scan from 400–1300 Da followed by twenty 100 ms MS2 candidate ion scans from 100–2000 Da in high sensitivity mode. Only ions with a charge of 2+ to 4+ which exceeded a threshold of 200 cps were selected for MS2, and former precursors were excluded for 10 secs after 1 occurrence.

All MS/MS spectra were searched against the latest human proteome at the time (RefSeq v42 & v57 (O'Leary et al., 2016)) using the Mascot (Matrix Science) spectral matching program. Search engine results from each LC/MS/MS run were submitted to the ProHits platform (Liu et al., 2010). Conversion and Mascot parameters are detailed in Supplementary Data 2.

For a separate set of samples, submitted to PRIDE under the accession PXD010084 (Biostudies:S-BSST160), proteins were digested on-beads with trypsin as described (Hubner et al. 2010) and desalted using the stage trip protocol (Rappsilber et al. 2003). Peptides were separated on an EASY-nLC 1200 system (Thermo Fisher Scientific) coupled to a Q Exactive HF-X mass spectrometer (Thermo Fisher Scientific). A silica capillary-column (75 µm x 20 cm, 1.9 µm

C18 resin, ReproSil-Pur C18-AQ material, Dr Maisch GmbH) packed in-house was implemented at a flow rate of 250 nl/min. Peptides were separated using a 1 h gradient ramping from 2% to 30% LC solvent B (0.1% formic acid, 90% acetonitrile) in LC solvent A (0.1% formic acid, 3% acetonitrile). MS acquisition occurred in data-dependent mode using the top 20 peaks for MS2 fragmentation at a resolution of 70000 for MS1 and 15000 for MS2 and a maximum injection time of 100 ms for MS2. Database search was performed using MaxQuant version 1.5.2.8 (Cox and Mann 2008) with oxidized methionine, deamidation on asparagine and glutamine as well as acetylated N-termini as variable modifications and carbamidomethylation as a fixed modification against a human Uniprot database (2017-01) and a peptide and protein FDR cut-off of 1%. Quantitation on the protein level was done using the MaxLFQ algorithm (Cox et al. 2014) with the match-between-runs option turned on without requiring MS2 for LFQ comparisons.

Interactome network construction

The interactome data was extracted from the locally installed ProHits database, keeping data that was acquired in different mass spectrometry machines separate. The steps for data filtering and clean up that were applied on each dataset are as follows: First, we removed false positive hits due to carry-over of the bait or preys to the next sample. Specifically, every prey that was present in two or more consecutively prepared or ran samples with a reduced number of total peptides was removed. We then normalized the bait and prey total peptide counts by their sequence length. Better coverage of the bait implies better quality of the sample run and therefore better quality of the prey. To increase the score weight of these prey, we multiplied the normalized prey total peptide counts by that of the corresponding bait, creating a score for each prey that represents the weighted normalised total prey peptide counts. This led to improved precision and recall of known interactions in the subsequent analyses. In order to avoid bias against the bait-prey combinations that were tested in multiple replicates, we averaged the top two normalized prey total counts for each bait-prey combination for the background distribution. This allowed us to compare the total peptide counts for each prey across the different samples. In order to identify proteins that are statistically more abundant as prey of specific baits (in specific samples), we calculated the 99% prediction interval for the normalized prey peptide counts using as background their distribution across all samples, including the negative controls. Only those that have normalized prey peptide counts greater than the upper limit of the 99% prediction interval are kept as potential bait interactors. As a next step, using as a positive dataset high quality interactions that are present in the HIPPIE database (Schaefer et al., 2012) and as a negative dataset our negative controls, we defined a frequency and Mascot score cutoff that achieves a precision greater than 75% (7% and log(score)=6.3 respectively). Preys were removed if they appeared in the CRAPome database (Mellacheruvu et al., 2013) with a positive score and their

frequency or MASCOT scores did not comply with the identified respective cutoffs. A false discovery rate (based on DECOY sequences) of less than 1% was also a MASCOT cutoff score requirement. Additionally, preys appearing with less than three total unique peptides across specific bait samples were removed as interactors of these baits. The filtered list comprises the bronze ist of interactions. Finally, we calculated the ComPASS Z-score (Wenger et al., 2011) for our pairs and, using the same positive and negative datasets as above, we defined a silver cutoff that requires a precision of at least 70% and a gold cutoff whereby we achieved the best balance between precision and recall as defined by the Matthew Correlation Coefficient. Due to the variation in numbers of peptides that different mass spectrometers are able to sequence, samples processed by different machines were treated separately. The code for this analysis can be found here: https://gitlabci.ebi.ac.uk/petsalaki/the-rhome. The amount of data generated from the baits analyzed by a Q Exactive HF-X instrument (see above) was insufficient to create a background distribution and calculate the 99% prediction interval. Additionally, there were not enough true positive interactions to define the score and frequency cutoffs appropriately. As we had at least two replicates for these runs, we applied SAINTexpress (Choi et al., 2011) and required a cutoff greater than 0.3 SAINT score, a Z-score greater than 1, bait sequence coverage of at least 15%, project frequency less than 50%. This latter cutoff seems lenient, but several of our baits interacted with each other (validated by Western blot) in this set and therefore had a high project frequency. Finally, we merged all the interactome datasets, recalculated the project frequency over the entire project and removed prey with frequency greater than 10%.

Pathway enrichment

Pathway enrichment analysis (Figure S5B) was performed using the ReactomePA function from Bioconductor (Yu and He, 2016). Pathways were merged into one entry if they had a Pearson correlation greater than 0.7 in the vectors representing the genes included in these pathways. Clustering was done using the hclust function in R (Murtagh and Legendre, 2014).

GO terms enrichment

GO Term enrichment was calculated using the Funcassociate 3.0 web server(Berriz et al., 2003). Edges between GO terms were calculated using vectors of the genes included in the term and our set and calculating the Jaccard index. Results were visualized using Cytoscape(Russell and Cohn, 2012; Figure SA).

Evaluation of interactome quality

To confirm the quality of our dataset, we tested 26 randomly selected RhoGEF/RhoGAP pairs by co-IP and successfully validated 22 interactions (~83%; Figure S5A). Since we used a requirement of 70% precision to define the score cutoffs, this number is even higher than expected and underlines the quality of the dataset. Comparing our data to the most extensive

affinity-purification-based human interactome (Bioplex 2.0 (Huttlin et al., 2017)), we found an overlap of ~10% hits when looking at all common RhoGEF/GAP baits. Two factors may contribute to this relatively low number: while in our study we used N-terminally tagged full-length constructs and the longest isoforms of the regulators, only 18/94 (~19%) of the baits in the Bioplex study were of similar length to ours (i.e. less than 10% difference) and their constructs were C-terminally tagged. Additionally, the Bioplex studies used HEK293T cells, similarly to our study, but also MCF10A cells and constructs were stably expressed, whereas we collected data from both stable and transient expression of baits. If only the 18 constructs with similar length are compared, the overlap increases to 19%. Our uniquely-identified preys are relevant and complementary to those identified in the Bioplex study: A GO terms enrichment analysis (Huang et al., 2009a) revealed terms related to cell adhesion as the most highly enriched cluster for our unique preys (Biostudies:S-BSST160). Associations found uniquely in the Bioplex study also include relevant terms such as 'focal adhesion' and 'protein targeting' (Biostudies:S-BSST160), underlining that the two datasets are uncovering distinct sub-modules of similar and relevant functions. When describing 'novel' interactions, we are comparing to those found in the IntAct database (Hermjakob, 2004), which include the latest human interactome studies by AP/MS (Bioplex2) and yeast-two hybrid (HI-III;unpublished) studies, as well as extensively curated and comprehensive interactions found in the literature and all other available high throughput studies.

Bait-bait & bait-Rho GTPase effectors network

Among 1291 interacting pairs, we identified 62 bait-bait interactions of which 26 were tested and 22 confirmed by co-IP and Western blot. The expected number of RhoGEF/GAP - RhoGEF/GAP interactions in a randomized background network calculated by randomizing our network preys based on the BioPlex 2.0 network (Huttlin et al., 2017) but maintaining the size and degree distribution of our network for 10000 iterations is 6.7±3.7 interactions. We therefore observe a significant (p-value< 2.2e-16, odds ratio=10.09) enrichment of interactions among RhoGEFs/RhoGAPs, suggesting that they form a highly interconnected network. Similarly, we observe enrichment for interactions with known Rho GTPase effectors (expected=8.6±4.1, observed=20, p-value=7.6e-04, odds ratio=2.3) and with small GTPases (expected=10±4.5, observed=24, p-value=1.4e-04, odds ratio=2.5), indicating that Rho signaling is connected through the RhoGAP and GEF network to other small GTPase signaling pathways.

Domain enrichment in interacting preys

We sought to identify over-represented domains in our bait and prey proteins in order to shed light on potential functions of these domains in the cell context. Interestingly, other than the

RhoGAP and RhoGEF domains, we found that PDZ and SH3 domains are over-represented in both our bait-prey network (p-value=2.7e-16 and 2.5e-13 respectively) and our bait set individually (p-value=1e-04 and <2.2e-16 respectively). PDZ domains are often associated with recruitment of proteins to specific cellular localizations and bind to specific sequence motifs or lipids, while SH3 domains often act as adaptors to recruit proteins to specific signaling pathway functions. The over-representation of PDZ and SH3 domains in the prey proteins may suggest that in the absence of such domains in the RhoGAP/GEF protein sequences, PDZ or SH3 domain-containing interactors may act to recruit these proteins to sites where their function is required. SH3-domain containing prey are enriched for the GO term 'receptor tyrosine kinase binding' (p-value=1.2e-7) indicating that perhaps these interactors serve to connect RhoGAP/GEF function to extracellular signaling. Interestingly, using the ELM server (Dinkel et al., 2016), we were able to identify a PDZ-binding motif for 11 of the 18 baits interacting with PDZ-containing prey, and all baits interacting with an SH3-domain containing protein contain proline-rich regions in their sequence. Moreover, the majority of PDZ-containing preys are involved in cell junctions (p-value<1e-13) and cell polarity establishment (p-value<1e-15) and may act to recruit the appropriate RhoGAP/GEF to these sites for regulation of Rho GTPase function. All domains, including Pfam domains, were found using the SMART web-server (Letunic and Bork, 2017).

SRE.L-luciferase assay

Activation of Rho GTPases was assessed with the Rho-pathway selective SRE.L luciferase reporter as described previously (Hill et al., 1995; Wells et al., 2001). The assay is based on a mutated form of the serum response element that is efficiently engaged by active RhoA, Rac1 and Cdc42. HEK293T cells were cotransfected with the pGL4.34 SRE.L firefly reporter and the pRL-CMV Renilla luciferase control reporter (serves as control for transfection efficiency) together with a RhoGEF expression construct of interest. 150 000 cells were seeded into 12-well tissue culture plates in DMEM and transfected the next day (200 ng of pGL4.34, 20 ng of pRL-CMV and 50 ng of indicated FLAG-tagged plasmids) using FuGENE HD according to the manufacturer's instructions. The total amount of transfected DNA was kept constant between wells by adjustment with FLAG empty vector. 16-20 h post transfection, cells were washed in PBS and lysed in 140 µl NP40 lysis buffer containing cOmplete Protease Inhibitor (Roche) and 1 µg/ml DnaseI (New England BioLabs) for 20 min at 4°C on a rocking shaker. 20 µl of lysate were used for luciferase measurements. The transcription of Renilla luciferase and firefly luciferase were assessed using the Dual-Glo Luciferase Assay System (Promega) following manufacturer's instructions. Measurements were performed in a 96 well white flat bottom microplate (Greiner Bio One GmbH) in an Infinite M200 PRO plate reader (Tecan) using the i-control software in the luminescence mode, no attenuation and an integration time of 1000 ms. Firefly luminescence intensity was normalized to Renilla luminescence intensity. After taking aliquots

for the luciferase assay, lysates of triplicates were pooled for analysis of protein expression by Western Blot.

QUANTIFICATION AND STATISTICAL ANALYSIS

Automated FRET image analysis

Processing of raw image data sets was performed using a custom automated ImageJ script. Firstly, average background images for each channel were generated from 30 to 60 images of untransfected cells. Raw images and average background images were smoothed by Gaussian filter convolution with a radius of 1 pixel. Raw images were background corrected by subtraction of average background images. Background corrected images were then thresholded in each channel in order to define the regions of interest (ROIs) that were used for further analysis. The acceptor channel images, the mCherry channel images and, where needed, the miRFP670 channel images were thresholded in order to create ROIs that only include transfected cells. Furthermore, ROIs were generated in the donor and FRET-acceptor channels to exclude low intensity pixels. All ROIs were combined by logical "AND" operation. FRET-ratio (R) images were created within that final ROI by dividing the FRET-acceptor by the donor channel image on a pixel basis. The final ROI was then applied to measure the average intensity within the FRET-ratio image and images of the acceptor, mCherry, and miRFP670 channels.

FRET data analysis

Average FRET ratios were normalized to control. For the RhoGEF screen, four control wells were averaged per plate, for the RhoGAP screen, three control wells. Thresholds to assign RhoGEF and RhoGAP activities were defined as a multiple of the standard deviation (σ) of control+RhoGDI (RhoGEF screen) or control (RhoGAP screen), based on precision recall analysis benchmarks: 1+4σ of control+RhoGDI for RhoA (1.0613), 1+2σ of control+RhoGDI for Rac1 (1.0121), 1+2σ of control+RhoGDI for Cdc42 (1.016) for the RhoGEF screen and 1-4σ of control+RhoGDI (0.9265) for RhoA, 1-4σ of control (0.9603) for Rac1, 1-2σ of control (0.9779) for Cdc42 for the RhoGAP screen. For direct comparison of the catalytic activities of a given RhoGEF or RhoGAP towards RhoA, Rac1, and Cdc42, activities were quantified as follows: the change in FRET ratio compared to control+RhoGDI (RhoGEF screen) or control (RhoGAP screen) (ΔR) was normalized to the maximal FRET ratio change (ΔR_{MAX}). For regulators with multiple activities, only those above 20% of the main activity were taken into account.

Semiquantitative FRET data analysis

Semiquantitative FRET data analyses were performed on long and short forms of 19 Rho regulators to assess potential autoinhibition. The changes in FRET ratio (R) compared to

control+RhoGDI (RhoGEF screen) or control (RhoGAP screen) were calculated (*ΔR*). The RhoGEF or RhoGAP mCherry intensities were then normalized to the mCherry control intensities and *ΔR* of each of the the two regulator constructs where then each divided by their corresponding normalized mCherry intensities.

Calculation of enrichments

When calculating the enrichment of a feature in our interactome, we used as background a randomized network that maintained the size and degree distribution of our network. This was derived from the Bioplex 2.0 study (Huttlin et al., 2017), which is the most comprehensive human interactome acquired with a method similar to ours to date. This was done for 10000 iterations and we thus estimated the background expectation for the feature under question. When comparing enrichment of localizations, we used as background the Cell Atlas study or the (Simpson et al., 2000) study as described in the main text. The enrichment was then calculated using the fisher.test function in R. To compare the domain compositions of RhoGAP/GEFs, we compared the distribution of the domain numbers for RhoGAPs vs RhoGEFs using a Wilcox test (RhoGAPs: 3.2+/-2.4 vs. RhoGEFs:4.9+/-3.6, p-value 5e-04). More details for each specific analysis are provided in the Methods details above. To identify the actin-binding proteins among our interactome, we used the keyword 'actin binding proteins' to search the Uniprot database (UniProt, 2015; Biostudies:S-BSST160). The focal adhesion associated proteins were extracted from the adhesome.org database (Biostudies:S-BSST160; Zaidel-Bar et al., 2007). The calculation of substrate-specific enrichment of RhoGEFs/RhoGAPs on subcellular structures and compartments was done for all regulators (comprising those with promiscuous and with exclusive substrates) and only for those with exclusive substrate GTPases. Odds ratio and Fisher's exact test were calculated based on 2x2 contingency tables.

Statistical analysis of FRET screen

Statistical significance of all values above the threshold (RhoGEF screen) or below the threshold (RhoGAP screen) was calculated by unpaired Student's t-test versus control+RhoGDI (RhoGEF screen) or versus control (RhoGAP screen). Benjamini-Hochberg procedure was applied for multiple testing correction with α=0.05.

Statistical analysis of luciferase assay

Statistical significance of PLEKHG4B activation by ARHGEF11 and ARHGEF12 as determined by luciferase assay was determined using the One-way analysis of variance (ANOVA), followed by Tukey's multiple comparisons. Statistical calculations were performed with JMP Pro 11.0.0.

DATA AND SOFTWARE AVAILABILITY

The protein interactions from this publication (silver dataset) have been submitted to the IMEx (http://www.imexconsortium.org) consortium through IntAct (Orchard et al., 2013) and assigned the identifier IM-26436. The mass spectrometry proteomics data from the Q Exactive HF-X run have been deposited to the ProteomeXchange Consortium via the PRIDE (Vizcaíno et al. 2016) partner repository with the dataset identifier PXD010084. The rest of the mass spectrometry proteomics data have been deposited under the dataset identifier PXD010144. cDNA sequences have been submitted to the ENA database and assigned the accession numbers LS482294-LS482434. Detailed information, including sequences of the inserts in our cDNA library is provided in Table S1. The following data, figures and files can also be found in Biostudies:S-BSST160 - https://www.ebi.ac.uk/biostudies/studies/S-BSST160 (McEntyre et al., 2015): a) The results of the GO term analysis (using Funcassociate 3.0) on the protein interaction network we identified , b) the clustered (using the DAVID webserver (Huang et al., 2009b)) GO terms associated with prey only ours and not the Bioplex 2.0 study (Huttlin et al., 2017; Letunic and Bork, 2017) identified using common baits and the reverse c) The results from our localization study, the localization mentioned for our baits in the literature, plus associated PubMed IDs d) The results of our specificity screen for all baits in our screen and the specificities described in the literature and the associated PubMed IDs e) the full table of z-scores for the quantifications from the high content microscopy experiment and f) the dataset with the parameters we used in subsequent analysis after feature reduction g) the tables of the full mass spectrometry data before filtering and analysis h) the parameters used for their analysis i)the sequences of our cloned ORFs in fasta format j) The gold, silver and bronze interactome table with additional details to those provided in Table S4 k) the list of small GTPases, effectors and actin-binding proteins used to calculate enrichment for such interactions l) Figures of the GO terms and Reactome pathway enrichment analyses m) an overview figure of the domain composition of human RhoGAP/GEFs n) individual image files from the localisation screen and the high content imaging, o) our silver interactome annotated with the adhesome and actin binding proteins in our set. The code used for the filtering of the interactome data is available here: https://gitlabci.ebi.ac.uk/petsalaki/the-rhome.

Supplemental Item Titles

Supplementary Table 1. Information on the RhoGEFs/RhoGAPs included in our cDNA library. Detailed description of the RhoGEF/RhoGAP cDNA expression library including information on synonyms, Human Ensembl and Entrez GeneID, species in library, Protein ID, size of construct in the library, Citrine expression construct ID, cDNA source and cDNA sequence. Information can also be found here: Biostudies:S-BSST160. Related to "cDNA expression library of full-length mammalian RhoGEFs/RhoGAPs" section in main text.

Supplementary Table 2. RhoGEF/RhoGAP specificities identified in this study and in the literature. Data from FRET biosensor screen and from literature review are shown including information about other substrate GTPases and reference PubMed IDs. Due to the high degree of conflicting literature data, four separate lists were compiled with different emphases: integrated, *in vitro*, *in vivo* and gold standard, see STAR Methods. Information can also be found here: Biostudies:S-BSST160. Related to "Family-wide RhoGEF and RhoGAP activity screens" section in main text and Figure 1.

Supplementary Table 3. Localization reported in the literature and determined in this study. Overview of RhoGEF/RhoGAP subcellular localization screen including data from confocal, TIRF and Cytochalasin D screen with additional notes and data from literature review with reference Pubmed IDs. Information can also be found at Biostudies:S-BSST160. Related to "RhoGEFs and RhoGAPs display diverse spatial distribution in cells" section in the main text and Figure 3.

Supplementary Table 4. RhoGEF/RhoGAP interactome. The Gold, silver and bronze interactome lists are included. Information can also be found at Biostudies:S-BSST160. Related to "The RhoGEF/RhoGAP interactome is highly interconnected and includes components of multiple cellular processes" section in the main text and Figure 5.

Supplementary Data 1. Genbank files of cDNA sequences used in this study (the European Nucleotide Archive (ENA) & Biostudies:S-BSST160**)** Related to "cDNA expression library of full-length mammalian RhoGEFs/RhoGAPs" section in main text.

Supplementary Data 2. Parameters used for analysis of mass spectrometry data (Biostudies:S-BSST160**)** Related to "Sample preparation and mass spectrometry" section in STAR Methods.

Figure 1

A

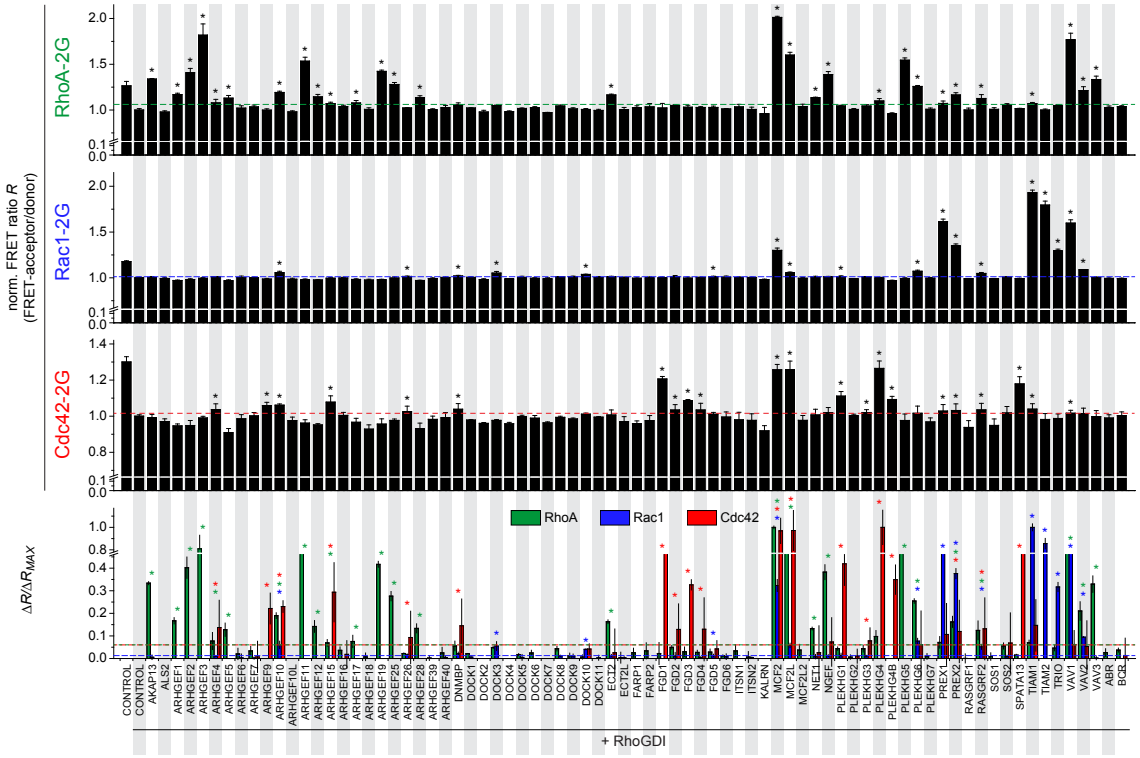

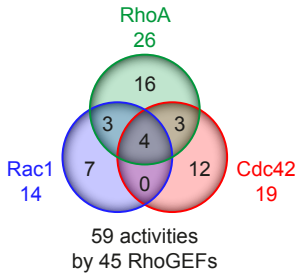

AKAP13, ARHGEF1, ARHGEF2, ARHGEF3, ARHGEF4, ARHGEF5, ARHGEF10, ARHGEF11, ARHGEF12, ARHGEF15, ARHGEF17, ARHGEF19, ARHGEF25, ARHGEF28, ECT2, MCF2, MCF2L, NET1, NGEF, PLEKHG5, PLEKHG6, PREX2, RASGRF2, VAV1, VAV2, VAV3

ARHGEF10, DOCK3, DOCK10, FGD5, MCF2, PLEKHG6, PREX1, PREX2, RASGRF2, TIAM1, TIAM2, TRIO, VAV1, VAV2

ARHGEF4, ARHGEF9, ARHGEF10, ARHGEF15, ARHGEF26, DNMBP, FGD1, FGD2, FGD3, FGD4, MCF2, MCF2L, PLEKHG1, PLEKHG3, PLEKHG4, PLEKHG4B, PREX2, RASGRF2, SPATA13

B

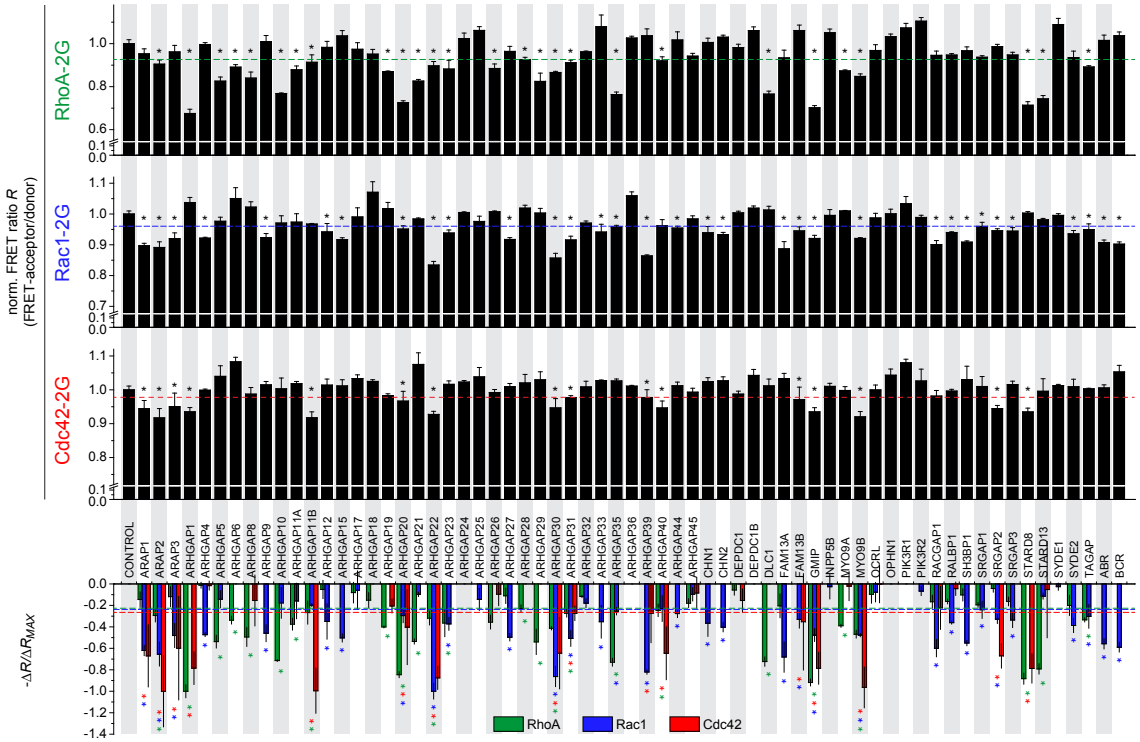

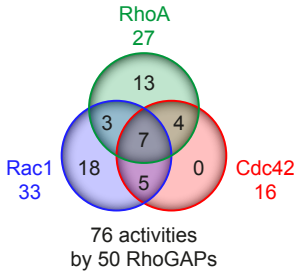

ARAP2, ARHGAP1, ARHGAP5, ARHGAP6, ARHGAP8, ARHGAP10, ARHGAP11A, ARHGAP11B, ARHGAP19, ARHGAP20, ARHGAP21, ARHGAP22, ARHGAP23, ARHGAP26, ARHGAP28, ARHGAP29, ARHGAP30, ARHGAP31, ARHGAP35, ARHGAP40, DLC1, GMIP, MYO9A, MYO9B, STARD8, STARD13, TAGAP

ARAP1, ARAP2, ARAP3, ARHGAP4, ARHGAP9, ARHGAP12, ARHGAP15, ARHGAP20, ARHGAP22, ARHGAP23, ARHGAP27, ARHGAP30, ARHGAP31, ARHGAP33, ARHGAP35, ARHGAP39, ARHGAP44, CHN1, CHN2, FAM13A, FAM13B, GMIP, MYO9B, RACGAP1, RALBP1, SH3BP1, SRGAP1, SRGAP2, SRGAP3, SYDE2, TAGAP, ABR, BCR

ARAP1, ARAP2, ARAP3, ARHGAP1, ARHGAP11B, ARHGAP20, ARHGAP22, ARHGAP30, ARHGAP31, ARHGAP39, ARHGAP40, FAM13B, GMIP, MYO9B, SRGAP2, STARD8

Figure 1. Family-wide RhoGEF and RhoGAP activity screens

(A) Results of RhoGEF assay: HEK293T cells were transfected with the mCherry-labeled RhoGEF cDNA library and the FRET sensors RhoA-2G, Rac1-2G, and Cdc42-2G together with RhoGDI (where indicated). All values were normalized to control+RhoGDI. (B) Results of RhoGAP assay: RhoGDI shRNA-depleted HEK293T cells were transfected with the mCherry-labeled RhoGAP cDNA library and indicated FRET sensors. All values were normalized to control. (A and B) Controls were transfected with sensor and mCherry alone. Mean ± SD (n=3) is shown throughout. Dashed lines indicate activity thresholds. Significance of values above (A) or below (B) the threshold was calculated by unpaired Student's t-test versus control+RhoGDI (A) or control (B) and Benjamini-Hochberg procedure was applied as multiple testing correction with α=0.05, significant values are marked with an asterisk (*). Graphs on the bottom show quantification of RhoGEF or RhoGAP activities towards RhoA (green), Rac1 (blue), and Cdc42 (red), allowing direct comparison. Changes in FRET ratio (ΔR) compared to control+RhoGDI (A) or control (B) were normalized to the maximal FRET ratio change (ΔR_{MAX}). For regulators with multiple activities, only those above 20% of the main activity were taken into account (asterisks). Venn diagrams show the numbers of RhoGEFs and RhoGAPs with single or multiple activities towards RhoA, Rac1, and Cdc42. Active regulators are listed by substrates RhoA (green box), Rac1 (blue box), and Cdc42 (red box).

Figure 2

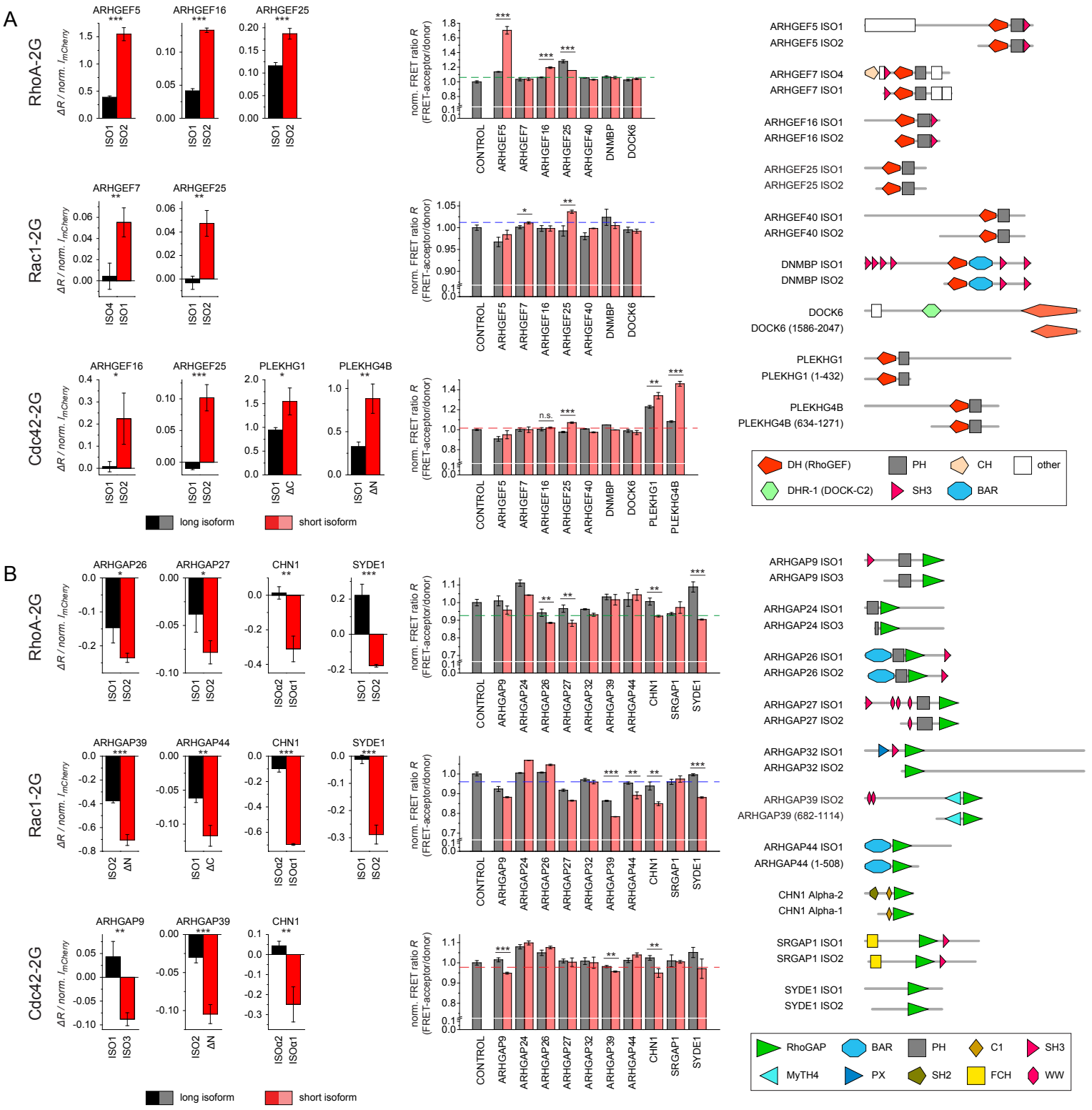
A
RhoA-2G
Rac1-2G
Cdc42-2G
ARHGEF5
ARHGEF16
ARHGEF25
ARHGEF7
PLEKHG1
PLEKHG4B
ΔR / norm. I_mCherry
ISO1
ISO2
ISO4
ΔC
ΔN
long isoform
short isoform
norm. FRET ratio R (FRET-acceptor/donor)
CONTROL
ARHGEF5
ARHGEF7
ARHGEF16
ARHGEF25
ARHGEF40
DNMBP
DOCK6
PLEKHG1
PLEKHG4B
n.s.
ARHGEF5 ISO1
ARHGEF5 ISO2
ARHGEF7 ISO4
ARHGEF7 ISO1
ARHGEF16 ISO1
ARHGEF16 ISO2
ARHGEF25 ISO1
ARHGEF25 ISO2
ARHGEF40 ISO1
ARHGEF40 ISO2
DNMBP ISO1
DNMBP ISO2
DOCK6
DOCK6 (1586-2047)
PLEKHG1
PLEKHG1 (1-432)
PLEKHG4B
PLEKHG4B (634-1271)
DH (RhoGEF)
PH
CH
other
DHR-1 (DOCK-C2)
SH3
BAR
B
RhoA-2G
Rac1-2G
Cdc42-2G
ARHGAP26
ARHGAP27
CHN1
SYDE1
ARHGAP39
ARHGAP44
ARHGAP9
ISO3
ISOα2
ISOα1
CONTROL
ARHGAP9
ARHGAP24
ARHGAP26
ARHGAP27
ARHGAP32
ARHGAP39
ARHGAP44
CHN1
SRGAP1
SYDE1
ARHGAP9 ISO1
ARHGAP9 ISO3
ARHGAP24 ISO1
ARHGAP24 ISO3
ARHGAP26 ISO1
ARHGAP26 ISO2
ARHGAP27 ISO1
ARHGAP27 ISO2
ARHGAP32 ISO1
ARHGAP32 ISO2
ARHGAP39 ISO2
ARHGAP39 (682-1114)
ARHGAP44 ISO1
ARHGAP44 (1-508)
CHN1 Alpha-2
CHN1 Alpha-1
SRGAP1 ISO1
SRGAP1 ISO2
SYDE1 ISO1
SYDE1 ISO2
RhoGAP
BAR
PH
C1
SH3
MyTH4
PX
SH2
FCH
WW

Figure 2. Autoinhibition is a common feature of RhoGEFs and RhoGAPs

Semiquantitative comparison of catalytic activities of full-length longest isoforms versus shorter isoforms or truncations of randomly selected 9 RhoGEFs (A) and 10 RhoGAPs (B). Experiments were performed as described in Figure 1A and 1B. Graphs on the left represent changes in FRET ratio (ΔR) normalized to RhoGEF or RhoGAP expression levels as determined by mCherry intensity. Values reflect arbitrary units. Graphs on the right show the FRET ratios normalized to control. Dashed lines indicate activity thresholds as in Figure 1. Values show mean ± SD (n=3; n=2 for ARHGEF40 and DNMBP). Significance levels were calculated by unpaired Student's t-tests as indicated: ***$p<0.001$, **$p<0.01$, *$p<0.05$, n.s.=not significant. Right panels: domain representations of the various constructs used, as in Figure S0.

Figure 3

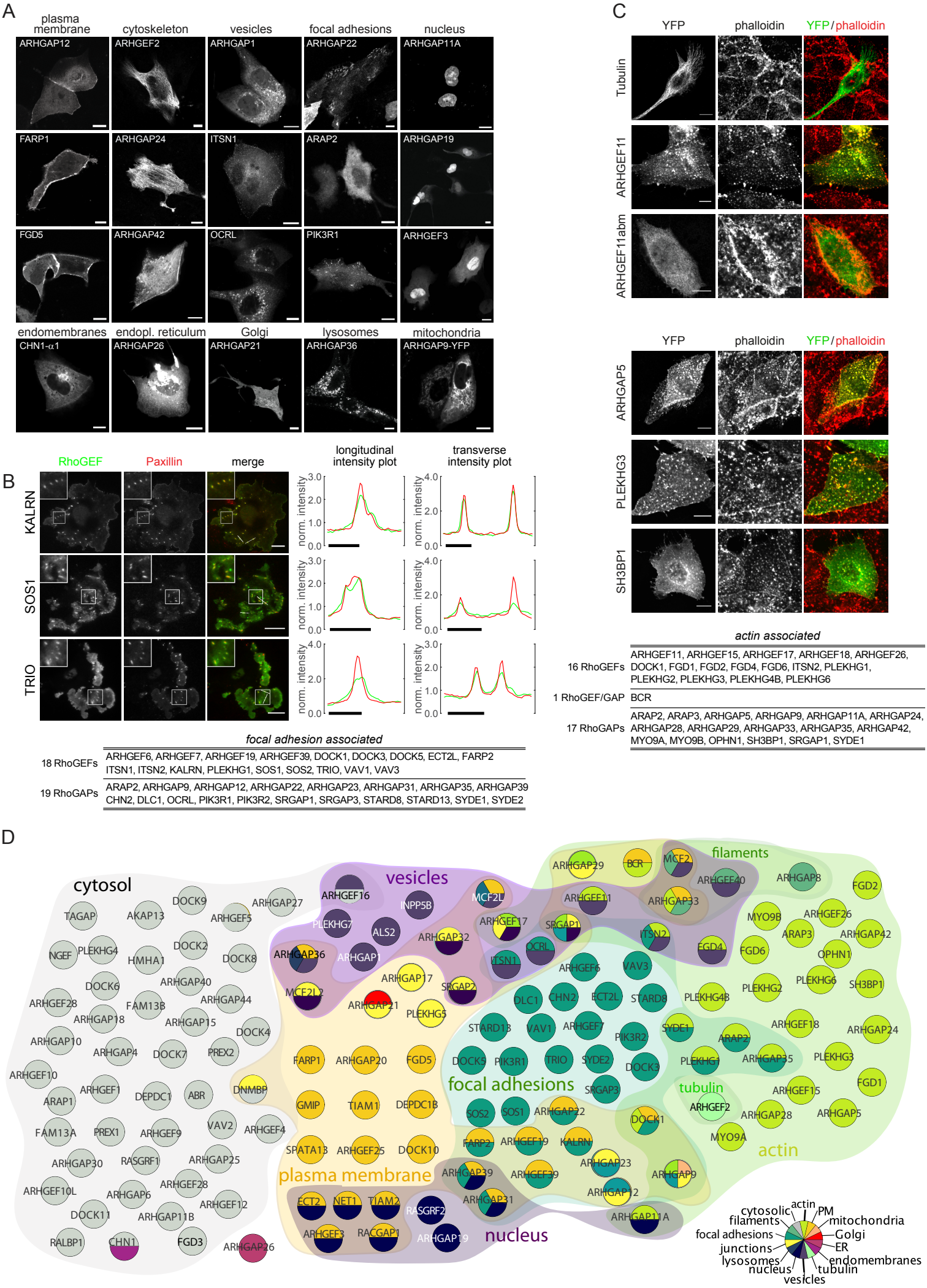

focal adhesion associated	
18 RhoGEFs	ARHGEF6, ARHGEF7, ARHGEF19, ARHGEF39, DOCK1, DOCK3, DOCK5, ECT2L, FARP2 ITSN1, ITSN2, KALRN, PLEKHG1, SOS1, SOS2, TRIO, VAV1, VAV3
19 RhoGAPs	ARAP2, ARHGAP9, ARHGAP12, ARHGAP22, ARHGAP23, ARHGAP31, ARHGAP35, ARHGAP39 CHN2, DLC1, OCRL, PIK3R1, PIK3R2, SRGAP1, SRGAP3, STARD8, STARD13, SYDE1, SYDE2

actin associated	
16 RhoGEFs	ARHGEF11, ARHGEF15, ARHGEF17, ARHGEF18, ARHGEF26, DOCK1, FGD1, FGD2, FGD4, FGD6, ITSN2, PLEKHG1, PLEKHG2, PLEKHG3, PLEKHG4B, PLEKHG6
1 RhoGEF/GAP	BCR
17 RhoGAPs	ARAP2, ARAP3, ARHGAP5, ARHGAP9, ARHGAP11A, ARHGAP24, ARHGAP28, ARHGAP29, ARHGAP33, ARHGAP35, ARHGAP42, MYO9A, MYO9B, OPHN1, SH3BP1, SRGAP1, SYDE1

Figure 3. RhoGEFs and RhoGAPs display diverse spatial distribution in cells

(A) Selection of confocal live-cell images of transiently transfected MDCK cells showing the localization of YFP-tagged RhoGEFs and RhoGAPs to the indicated subcellular compartments. (B) Focal adhesion localization revealed by live-cell TIRF microscopy of COS-7 cells stably expressing mCherry-Paxillin and transfected with the indicated YFP-tagged RhoGEFs (green: YFP, red: mCherry). Insets show higher magnifications of the boxed areas. Right panels: fluorescence intensity profiles of longitudinal and transverse sections through focal adhesions, indicated by white lines in the merged images. Intensity plots were normalized to the average intensity over the whole line. White scale bars: 20 µm, black scale bars: 5 µm. (C) Actin association assessed by confocal imaging of Cytochalasin D-treated MDCK cells transiently transfected with the indicated YFP-tagged RhoGEFs, RhoGAPs or controls (abm: actin binding mutant). Cells were fixed and stained for actin with phalloidin, YFP signals were enhanced by anti-GFP immunofluorescence (green: YFP, red: actin). Scale bars: 10 µm. (D) Summary of the distribution of RhoGEF and RhoGAP proteins over different subcellular compartments.

Figure 4

A

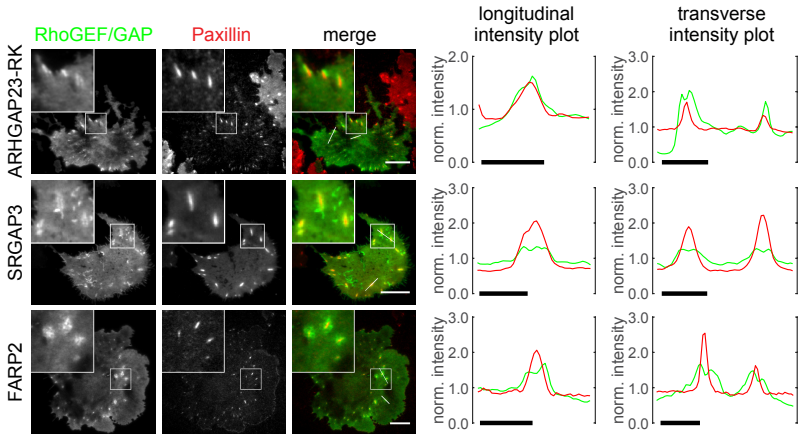

pericentric focal adhesion localization

ECT2L, FARP2, ARAP2, ARHGAP22, ARHGAP23, SRGAP3

B

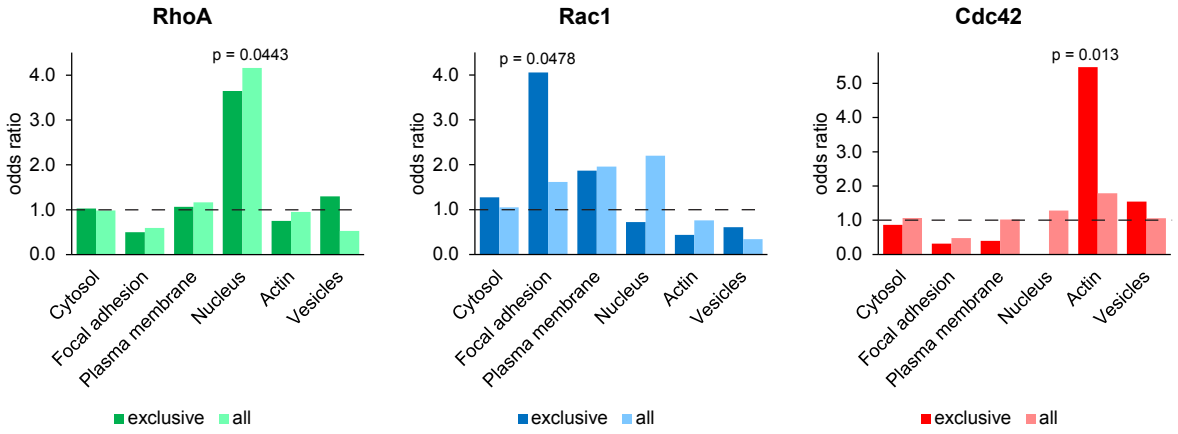

Figure 4. Micro-compartmentalization and substrate-specific local overrepresentation of RhoGEFs/RhoGAPs

(A) Live-cell TIRF micrographs as in Figure 3B, revealing the pericentric focal adhesion localization of the indicated regulators. Note the RhoGEF/RhoGAP intensity minimum at the center of focal adhesions as indicated by the maximal Paxillin intensity. (B) RhoA-, Rac1- and Cdc42-specific regulators are enriched in the nucleus, on focal adhesions and on actin, respectively. Odds ratios for enrichment of RhoGEFs and RhoGAPs with activity towards RhoA, Rac1, and Cdc42 (as identified in the FRET-based substrate specificity screen) on indicated subcellular locations. Values were calculated for RhoGEFs and RhoGAPs with exclusive GTPase substrate activity (exclusive) and, for comparison, for promiscuous and exclusive regulators combined (all). Dashed lines indicate no enrichment at odds ratio 1. p values were determined by Fisher's exact test.

Figure 5

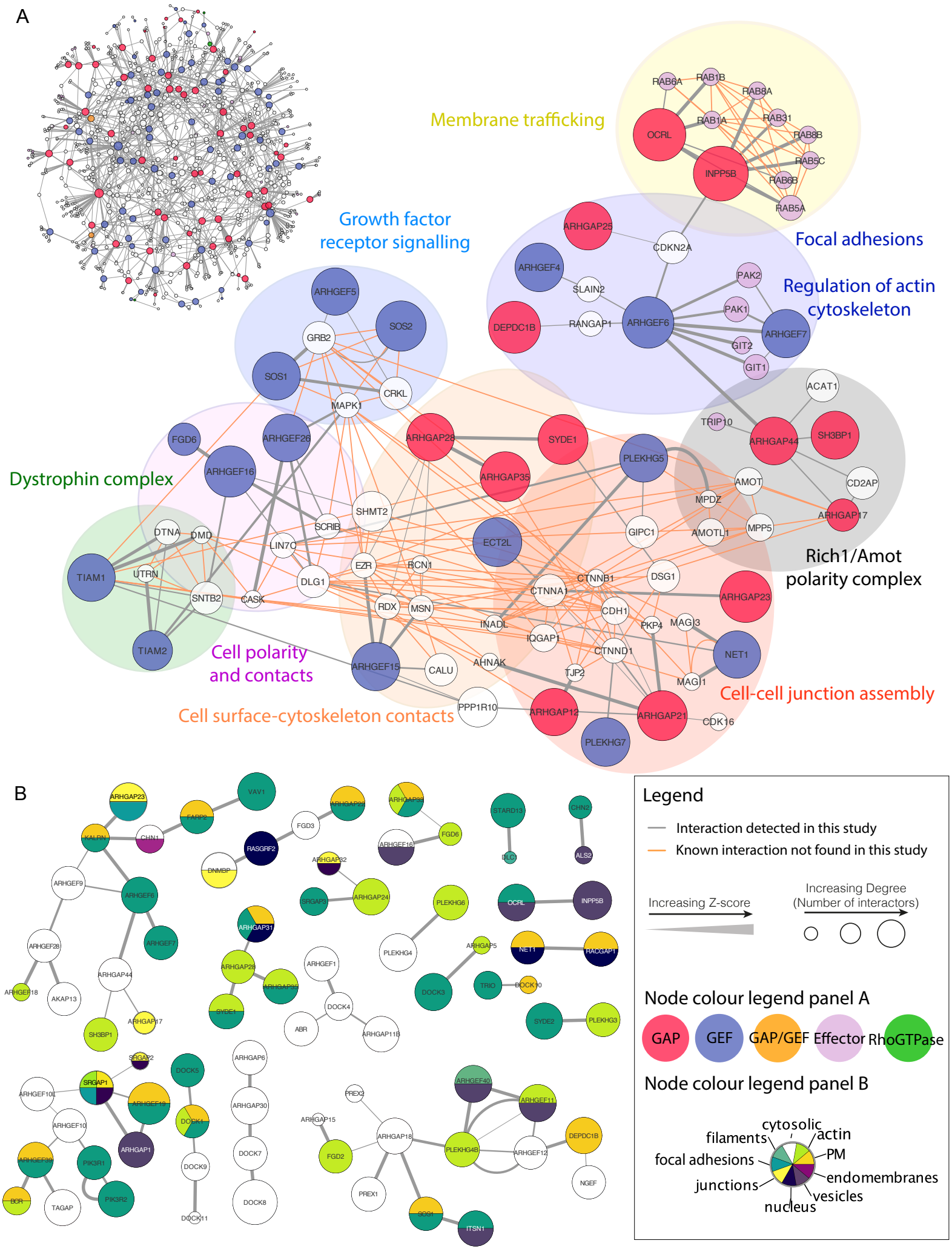
A
Membrane trafficking
RAB6A
RAB1B
RAB8A
RAB1A
RAB31
OCRL
RAB8B
RAB5C
INPP5B
RAB6B
RAB5A
Growth factor receptor signalling
Focal adhesions
ARHGAP25
CDKN2A
ARHGEF4
SLAIN2
PAK2
Regulation of actin cytoskeleton
ARHGEF5
PAK1
DEPDC1B
RANGAP1
ARHGEF6
ARHGEF7
SOS2
GRB2
GIT2
GIT1
SOS1
CRKL
MAPK1
ACAT1
TRIP10
ARHGAP44
SH3BP1
FGD6
ARHGEF26
ARHGAP28
SYDE1
PLEKHG5
ARHGEF16
ARHGAP35
AMOT
CD2AP
Dystrophin complex
MPDZ
SHMT2
ARHGAP17
DTNA
DMD
SCRIB
GIPC1
AMOTL1
MPP5
LIN7C
ECT2L
Rich1/Amot polarity complex
TIAM1
UTRN
EZR
RCN1
DLG1
CTNNB1
DSG1
SNTB2
CASK
CTNNA1
ARHGAP23
RDX
MSN
CDH1
INADL
PKP4
MAGI3
IQGAP1
NET1
TIAM2
CTNND1
Cell polarity and contacts
ARHGEF15
CALU
AHNAK
TJP2
MAGI1
Cell-cell junction assembly
PPP1R10
ARHGAP12
ARHGAP21
CDK16
Cell surface-cytoskeleton contacts
PLEKHG7
B
ARHGAP23
VAV1
FARP2
FGD3
STARD13
CHN2
KALRN
CHN1
RASGRF2
FGD6
ALS2
DNMBP
ARHGAP32
ARHGEF9
ARHGEF6
SRGAP3
ARHGAP24
PLEKHG6
OCRL
INPP5B
ARHGAP31
ARHGEF26
ARHGEF7
PLEKHG4
ARHGAP5
NET1
RACGAP1
ARHGAP44
ARHGAP28
ARHGEF1
ARHGEF18
AKAP13
DOCK3
TRIO
DOCK10
SYDE1
DOCK4
ARHGAP17
SYDE2
PLEKHG3
SH3BP1
ABR
ARHGAP11B
SRGAP2
ARHGAP6
DOCK5
SRGAP1
ARHGEF40
ARHGEF10L
ARHGEF12
PREX2
ARHGEF11
ARHGAP30
DOCK1
ARHGEF10
ARHGAP15
DEPDC1B
ARHGAP1
ARHGAP18
PLEKHG4B
ARHGEF12
DOCK7
ARHGEF39
PIK3R1
FGD2
DOCK9
NGEF
BCR
TAGAP
PIK3R2
PREX1
DOCK8
SGSM1
ITSN1
DOCK11
Legend
Interaction detected in this study
Known interaction not found in this study
Increasing Z-score
Increasing Degree (Number of interactors)
Node colour legend panel A
GAP
GEF
GAP/GEF
Effector
RhoGTPase
Node colour legend panel B
cytosolic
actin
filaments
PM
focal adhesions
endomembranes
junctions
vesicles
nucleus

Figure 5. The RhoGEF/RhoGAP interactome is highly interconnected and includes components of multiple cellular processes

(A) RhoGEF/RhoGAP interactome network. As examples of subnetworks of the RhoGEF/RhoGAP interactome, interactions with complexes involved in cell polarity, junctions, membrane trafficking, growth factor receptor signaling and actin cytoskeleton organization are shown. (B) Bait-bait interactome. Our network is enriched (p-value <<0.001) in bait-bait interactions among RhoGEFs and RhoGAPs. Shown are all 66 interactions, with nodes color-coded by their subcellular localization (see also Figure 3).

Figure 6

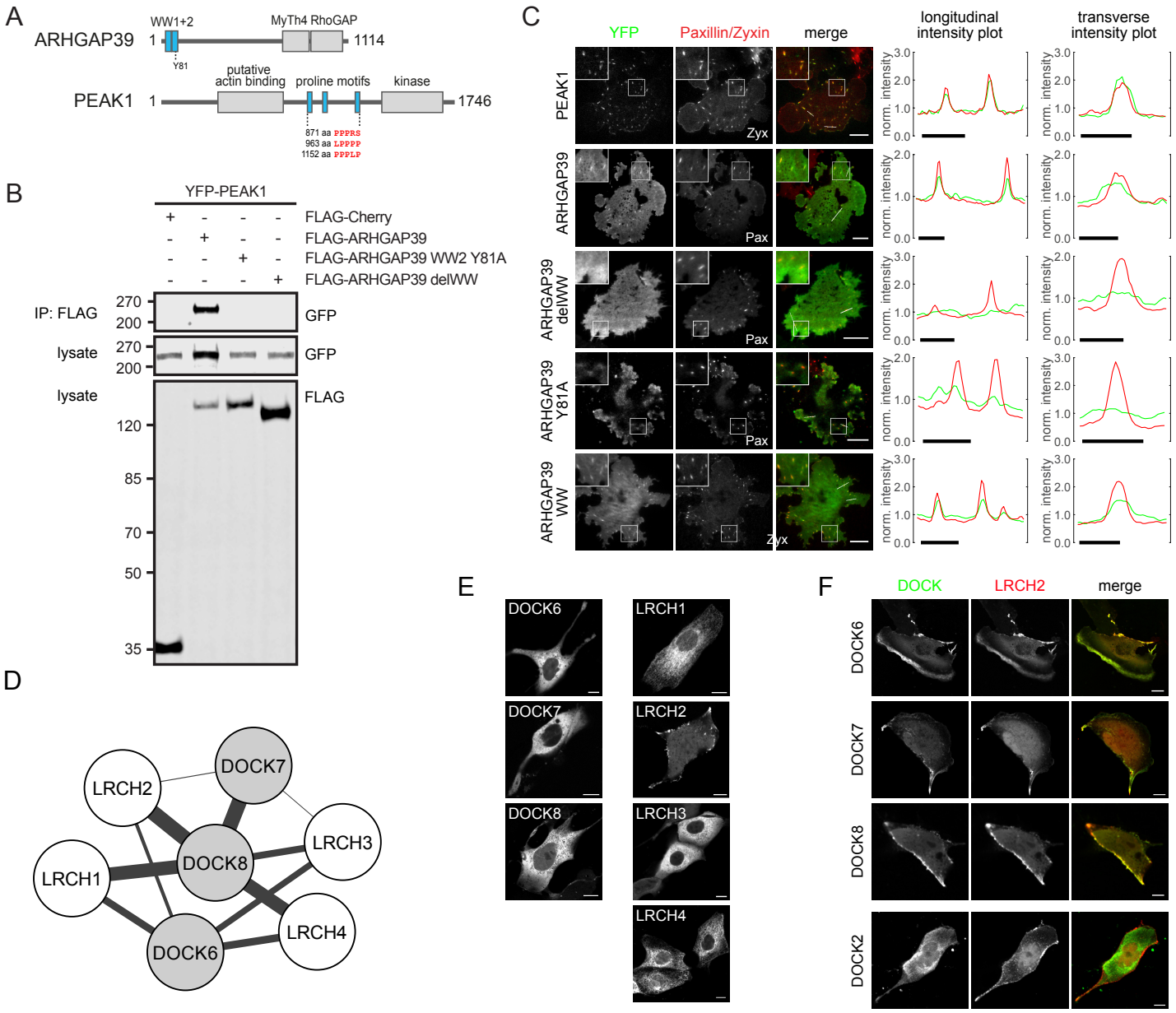
A
ARHGAP39
WW1+2
MyTh4 RhoGAP
1
1114
Y81
PEAK1
putative actin binding
proline motifs
kinase
1746
871 aa PPPRS
963 aa LPPPP
1152 aa PPPLP
B
YFP-PEAK1
FLAG-Cherry
FLAG-ARHGAP39
FLAG-ARHGAP39 WW2 Y81A
FLAG-ARHGAP39 delWW
IP: FLAG
lysate
GFP
FLAG
270
200
120
85
70
50
35
C
YFP
Paxillin/Zyxin
merge
longitudinal intensity plot
transverse intensity plot
PEAK1
ARHGAP39
ARHGAP39 delWW
ARHGAP39 Y81A
ARHGAP39 WW
Zyx
Pax
norm. intensity
D
DOCK7
LRCH2
LRCH3
LRCH1
DOCK8
LRCH4
DOCK6
E
DOCK6
LRCH1
DOCK7
LRCH2
DOCK8
LRCH3
LRCH4
F
DOCK
LRCH2
merge
DOCK6
DOCK7
DOCK8
DOCK2

Figure 6. Network data reveals RhoGEF/RhoGAP interactors mediating their relocalization

(A) Schematic representation of human ARHGAP39 and PEAK1. Putative WW domain-binding proline-rich motifs are indicated in red. (B) PEAK1 interacts with the WW domain of ARHGAP39. Lysates of HEK293T cells transfected with YFP-PEAK1 together with FLAG-ARHGAP39 wild type, a Y81A functional mutant of the second WW domain, a construct lacking both WW domains or FLAG-Cherry control were immunoprecipitated (IP-ed) using a FLAG antibody and immunoblotted using a GFP antibody. (C) PEAK1 recruits ARHGAP39 via its WW domain. As in Figure 3C, TIRF micrographs of COS-7 cells expressing the indicated focal adhesion markers were transfected with YFP-tagged PEAK1 or different ARHGAP39 constructs. (D) C-DOCK and LRCH family proteins form a highly interconnected network. Thickness of nodes represents the Z-score and interactome is derived from the bronze list. (E) Confocal micrographs of live MDCK cells expressing YFP-fusions of all C-DOCK and all LRCH family proteins alone (see Figure S6 for details about LRCH protein isoforms used), or (F) the indicated proteins together, revealing the recruitment of DOCK6,7,8 from the cytosol to the cell periphery by LRCH2. Control: A-DOCK family protein DOCK2. Scale bars (E, F): 10 µm.

Figure 7

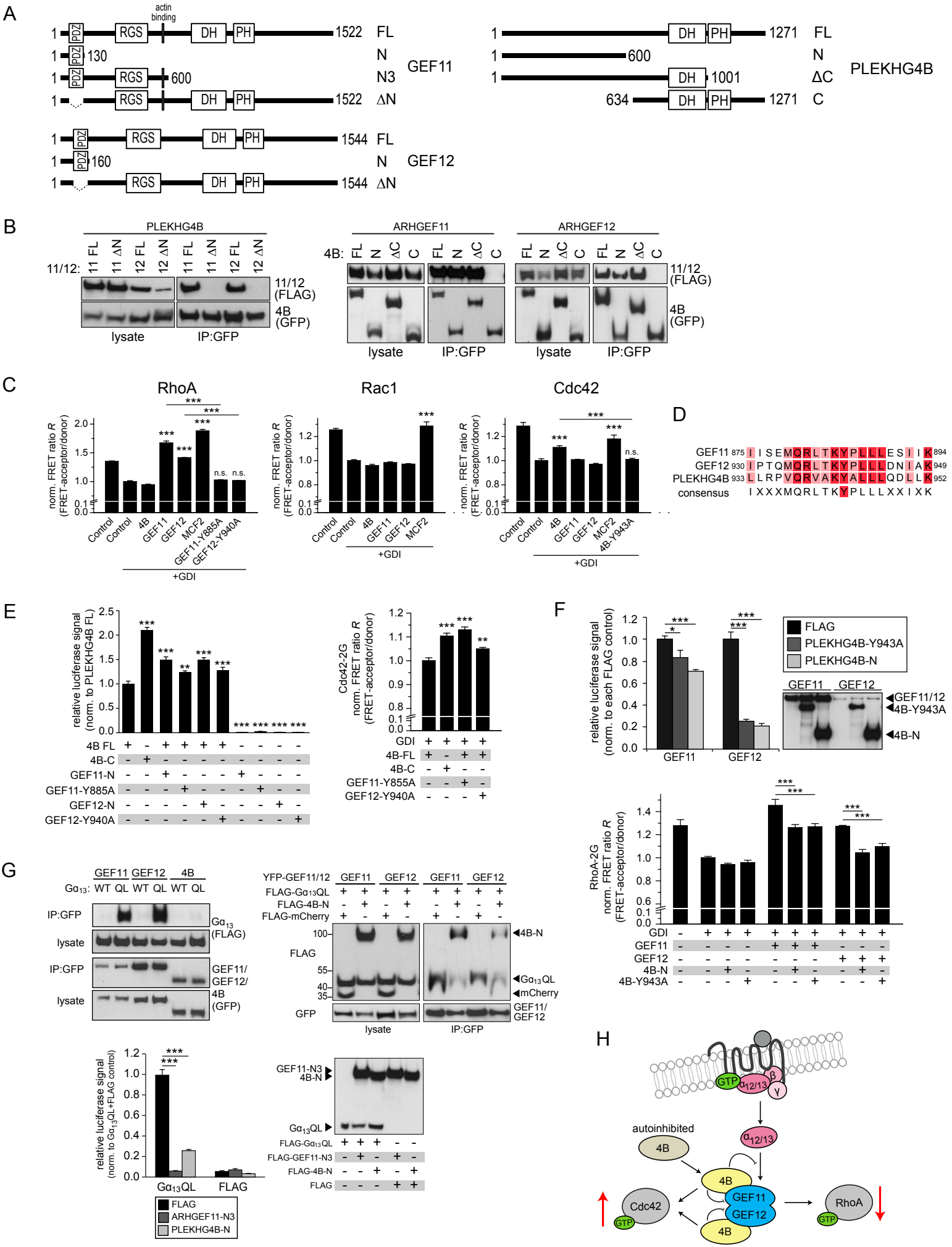
A
actin binding
PDZ
RGS
DH
PH
1522 FL
130 N
600 N3
1522 ΔN
GEF11
1544 FL
160 N
1544 ΔN
GEF12
1271 FL
600 N
1001 ΔC
634 1271 C
PLEKHG4B
B
PLEKHG4B
11/12: 11 FL 11 ΔN 12 FL 12 ΔN 11 FL 11 ΔN 12 FL 12 ΔN
11/12 (FLAG)
4B (GFP)
lysate
IP:GFP
ARHGEF11
ARHGEF12
4B: FL N ΔC C
C
RhoA
Rac1
Cdc42
norm. FRET ratio R (FRET-acceptor/donor)
Control
4B
GEF11
GEF12
MCF2
GEF11-Y885A
GEF12-Y940A
4B-Y943A
+GDI
n.s.
D
GEF11 875 I I S E M Q R L T K Y P L L L E S I I K 894
GEF12 930 I P T Q M Q R L T K Y P L L L D N I A K 949
PLEKHG4B 933 L L R P V Q R V A K Y A L L L Q D L L K 952
consensus I X X X M Q R L T K Y P L L L X X I X K
E
relative luciferase signal (norm. to PLEKHG4B FL)
4B FL
4B-C
GEF11-N
GEF11-Y885A
GEF12-N
GEF12-Y940A
Cdc42-2G norm. FRET ratio R (FRET-acceptor/donor)
GDI
4B-FL
F
relative luciferase signal (norm. to each FLAG control)
FLAG
PLEKHG4B-Y943A
PLEKHG4B-N
GEF11
GEF12
GEF11/12
4B-Y943A
4B-N
RhoA-2G norm. FRET ratio R (FRET-acceptor/donor)
G
Gα13: WT QL WT QL WT QL
IP:GFP
lysate
Gα13 (FLAG)
GEF11/ GEF12/ 4B (GFP)
YFP-GEF11/12
FLAG-Gα13QL
FLAG-4B-N
FLAG-mCherry
FLAG
GFP
4B-N
Gα13QL
mCherry
relative luciferase signal (norm. to Gα13QL+FLAG control)
Gα13QL
FLAG
ARHGEF11-N3
PLEKHG4B-N
GEF11-N3
FLAG-Gα13QL
FLAG-GEF11-N3
H
GTP
α12/13
β
γ
autoinhibited
4B
Cdc42
RhoA

Figure 7. A multi-RhoGEF complex downstream of GPCR

(A) Schematic representation of the three human RhoGEFs and truncations used. (B) PLEKHG4B, ARHGEF11 and ARHGEF12 interact via their N-termini. HEK293T cells were transfected with YFP-PLEKHG4B together with FLAG-ARHGEF11 or FLAG-ARHGEF12 full-length or N-terminal deletion mutants (left panel), or with FLAG-ARHGEF11 or FLAG-ARHGEF12 together with YFP-tagged PLEKHG4B full-length or indicated deletion mutants (right panel). Lysates were IP-ed using a GFP antibody and immunoblotted using GFP or FLAG antibodies. (C) ARHGEF11 and ARHGEF12 are RhoA-specific GEFs, whereas PLEKHG4B activates Cdc42. As described in Figure 1A, FRET ratios of the three Rho biosensors in presence of the indicated RhoGEFs or GEF-dead mutants. (D) Sequence alignment of human ARHGEF11, ARHGEF12 and PLEKHG4B revealing the conserved tyrosine in the center of the DH domain (Sterpetti et al., 1999), critical for the catalytic function of several RhoGEFs. (E) Autoinhibition of PLEKHG4B and its release by ARHGEF11 and ARHGEF12 binding. Left panel: effect of the indicated ARHGEF11 or ARHGEF12 constructs on PLEKHG4B-stimulated SRE-luciferase reporter activation in HEK293T cells. Right panel: FRET ratios of HEK293T cells transfected with the Cdc42-2G biosensor together with RhoGDI, mCherry-tagged PLEKHG4B and the indicated miRFP-tagged ARHGEF11 and ARHGEF12 mutants. (F) ARHGEF11 and ARHGEF12 are inhibited by PLEKHG4B. Upper panel: as in (E), effect of indicated PLEKHG4B constructs on ARHGEF11- or ARHGEF12-stimulated SRE-luciferase reporter activation. Anti-FLAG Western Blot shows the expression of the transfected constructs. Lower panel: FRET ratios of HEK293T cells transfected with the RhoA-2G biosensor together with RhoGDI, mCherry-ARHGEF11 or -ARHGEF12 and the indicated miRFP-tagged PLEKHG4B mutants. (G) PLEKHG4B inhibits Gα13-mediated ARHGEF11/12 recruitment and downstream RhoA activation. Upper left panel: HEK293T cells were transfected with YFP-fusions of the three GEFs and wild type (WT) or constitutively active FLAG-Gα13 (QL). Lysates were IP-ed using a GFP antibody and immunoblotted using GFP or FLAG antibodies. Upper right panel: HEK293T cells were transfected with the indicated YFP- and FLAG-tagged proteins. Lysates were IP-ed using a GFP antibody and immunoblotted using GFP or FLAG antibodies. Lower left panel: as in (E), effect of N-terminal fragments of ARHGEF11 or PLEKHG4B on Gα13QL-stimulated SRE-luciferase reporter activation. Anti-FLAG Western Blot shows the expression of transfected constructs. H) Model of PLEKHG4B interaction with ARHGEF11 and ARHGEF12 and their mutual regulation of Gα12/13-mediated GPCR signaling. All bar graphs show mean of three (C, E left, F, and G) or four (E right) independent experiments. Error bars indicate standard deviation. Significance was calculated by unpaired Student's t-test (C, E (right panel), F, and G) versus control+GDI (C), versus PLEKHG4B (E (right panel)) or as indicated by the lines. Significance was determined using the One-way ANOVA, followed by Tukey's multiple comparisons (E (left panel)). Significance was ranked as * $p<0.05$, ** $p<0.01$, *** $p<0.001$.

Figure S0

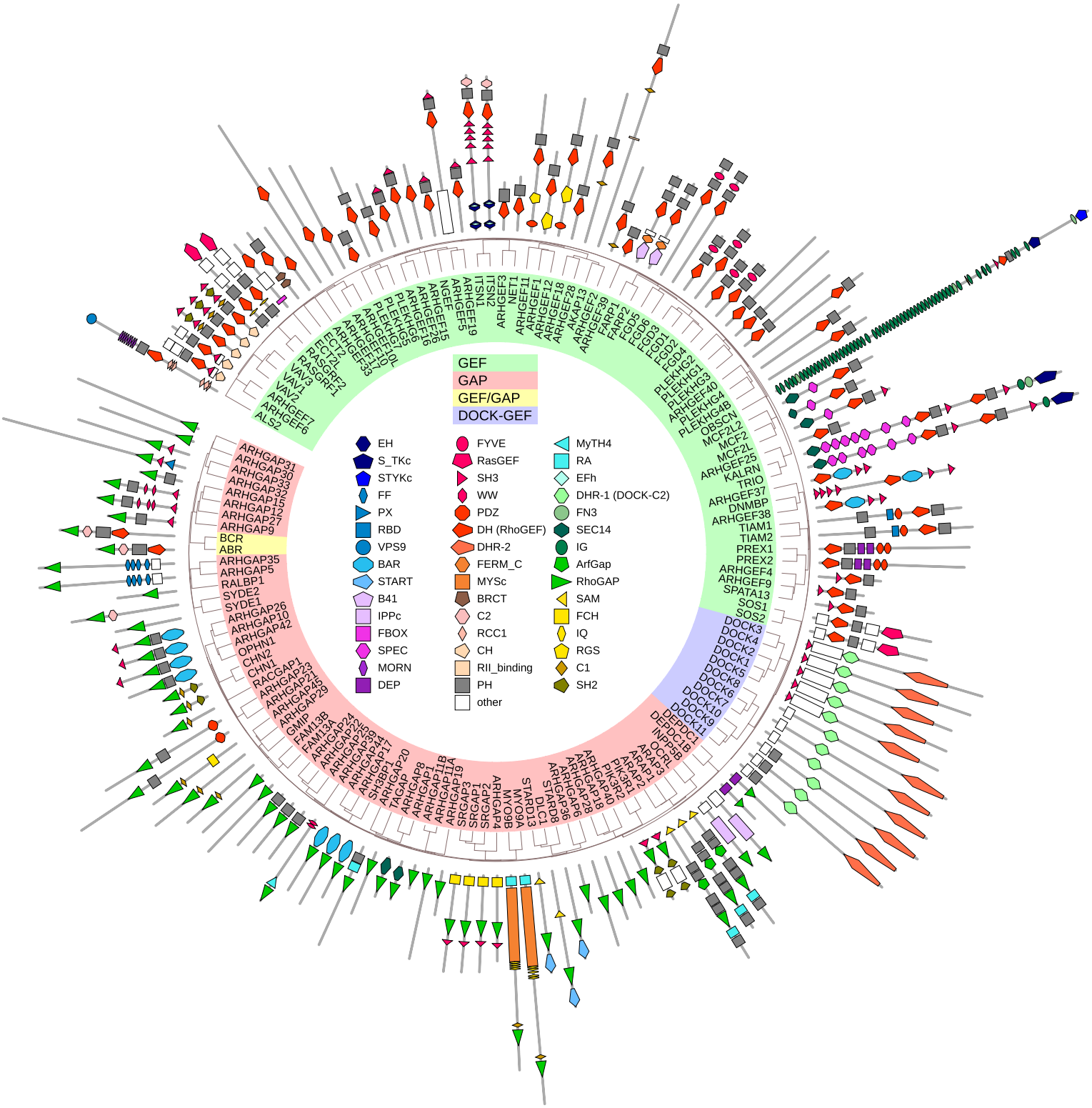
GEF
GAP
GEF/GAP
DOCK-GEF
EH
S_TKc
STYKc
FF
PX
RBD
VPS9
BAR
START
B41
IPPc
FBOX
SPEC
MORN
DEP
FYVE
RasGEF
SH3
WW
PDZ
DH (RhoGEF)
DHR-2
FERM_C
MYSc
BRCT
C2
RCC1
CH
RII_binding
PH
other
MyTH4
RA
EFh
DHR-1 (DOCK-C2)
FN3
SEC14
IG
ArfGap
RhoGAP
SAM
FCH
IQ
RGS
C1
SH2

Figure S0. Domain architecture of the human RhoGEF and RhoGAP proteins (Biostudies S-BSST160).

The canonical isoforms of all 145 human RhoGEFs and RhoGAPs containing all distinguishable domains, were collected from UniProt and clustered by multiple sequence alignment using ClustalOmega. The resulting dendrogram and domain structures as predicted by SMART and Pfam (or by Prosite for ARHGEF37 and ARHGEF38) were assembled using iTol. Not all domain families are listed, non-selected ones are indicated as 'other'. IGc2, IG and IG_like were summarized as IG. OBSCN is downscaled by a factor of 0.5.

Figure S1

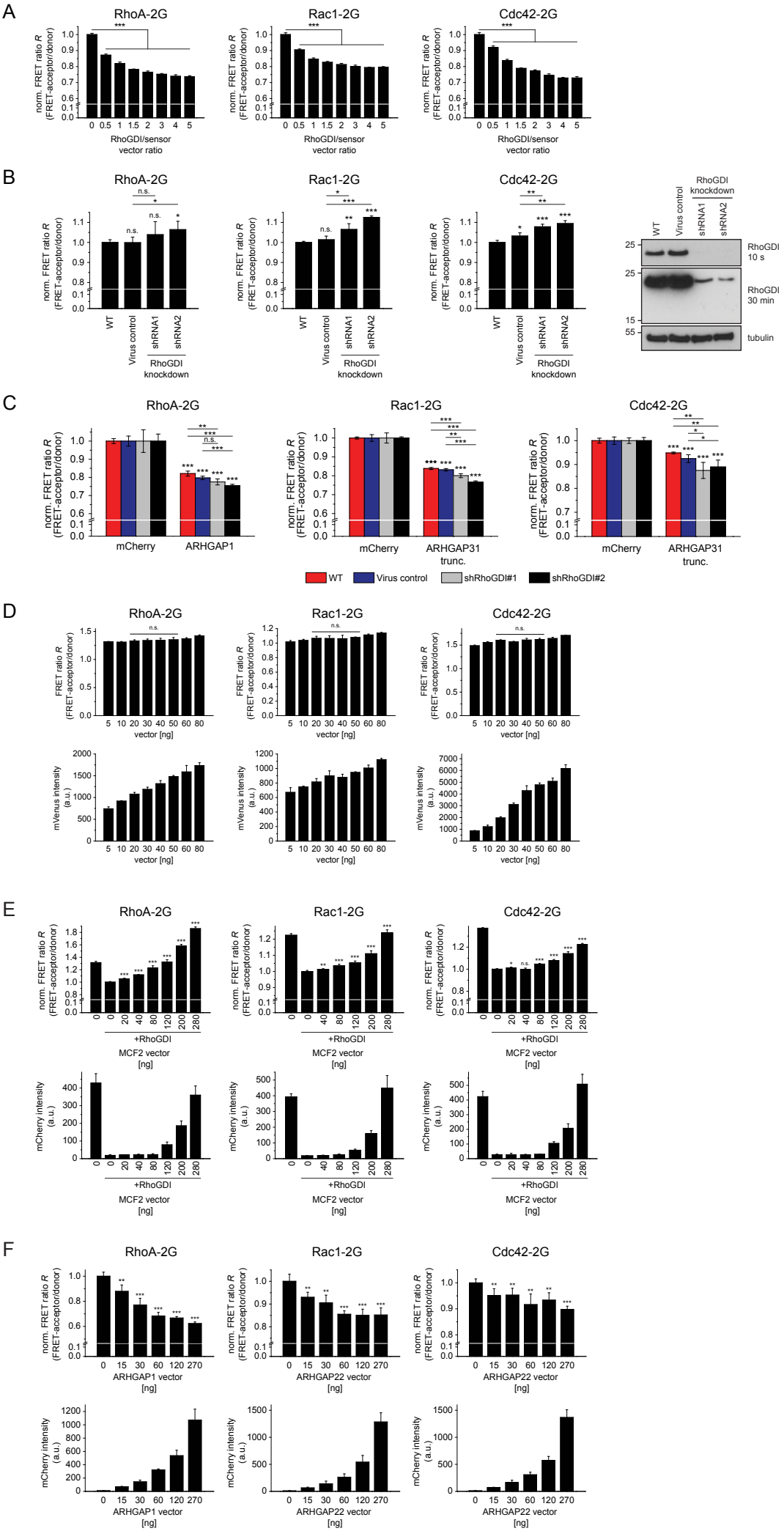
A
RhoA-2G
Rac1-2G
Cdc42-2G
norm. FRET ratio R (FRET-acceptor/donor)
RhoGDI/sensor vector ratio
B
WT
Virus control
shRNA1
shRNA2
RhoGDI knockdown
RhoGDI 10 s
RhoGDI 30 min
tubulin
C
mCherry
ARHGAP1
ARHGAP31 trunc.
WT
Virus control
shRhoGDI#1
shRhoGDI#2
D
FRET ratio R (FRET-acceptor/donor)
vector [ng]
mVenus intensity (a.u.)
E
+RhoGDI
MCF2 vector [ng]
mCherry intensity (a.u.)
F
ARHGAP1 vector [ng]
ARHGAP22 vector [ng]

Figure S1. Establishment of the FRET-based RhoGEF/RhoGAP activity screen, Related to Figure 1

(A) RhoGDI addition decreases the basal activity of the Rho biosensors. Overexpressed Rho sensors exhibit elevated basal activity levels (STAR Methods). To restore low levels, allowing high dynamic range RhoGEF responses, increasing concentrations of RhoGDI plasmid were transfected into HEK293T cells together with the indicated Rho sensors. Total DNA levels were filled to the same amount with mCherry plasmid. FRET ratio was normalized to control (RhoGDI/sensor vector ratio 0). Data represents mean of five fields of view for each condition, error bars indicate standard deviation. Significance levels were calculated by individual unpaired Student's t-tests against control (RhoGDI/sensor vector ratio 0): ***$p<0.001$. Note that approximately a 2-fold excess of coexpressed RhoGDI over the sensors reestablished their low basal activity without saturating the system with RhoGDI. (B) RhoGDI depletion increases the basal activity of the Rho biosensors. Right panel: Stable RhoGDI knockdown cell lines were created by lentiviral infection of HEK293T cells with two different shRNA vectors (shRNA#1 and shRNA#2) and subsequent antibiotic selection. Cells stably transduced with pLKO.1 TRC cloning vector served as control together with non-infected wt HEK293T cells. Lysates were immunoblotted with the indicated antibodies. For RhoGDI, a short and a long exposure is shown. Left graphs: HEK293T cells (WT), control lentivirus transduced cells (control), and the two RhoGDI knockdown cell lines were transfected with the indicated Rho sensors. FRET ratios were normalized to WT. Data represent mean of four independent experiments, error bars indicate standard deviation. Significance levels were calculated by unpaired Student's t-test against WT or as indicated by lines: ***$p<0.001$, **$p<0.01$, *$p<0.05$, n.s. = not significant. (C) FRET biosensor response to RhoGAPs is more pronounced in RhoGDI-depleted cells. HEK293T cells (WT), control virus transduced cells (control), and the two RhoGDI knockdown cell lines were transfected with each of the Rho sensors together with the indicated RhoGAPs or mCherry control. FRET ratio was normalized to mCherry control of each cell line. Data show mean of four independent experiments, error bars indicate standard deviation. Significance levels indicated on top of bars were calculated by unpaired Student's t-test against mCherry control. Significance levels indicated by lines were calculated by unpaired Student's t-test after data normalization: ***$p<0.001$, **$p<0.01$, *$p<0.05$, n.s. = not significant. RhoGDI shRNA#2 HEK293T cells allowed the highest dynamic responses and were therefore used in all subsequent RhoGAP activity assays. (D) FRET ratio is stable across a wide range of sensor expression levels. HEK293T cells were transfected with increasing amounts of the indicated Rho sensors. Total DNA levels were adjusted to equal amounts with mCherry plasmid. The mVenus intensity shown in the lower panel represents the sensor expression levels. Data represents the mean of three independent experiments, error bars indicate standard deviation. Significance levels were calculated by individual unpaired Student's t-tests within all samples under the line: n.s. = not significant. This experiment shows the robustness of the assay to technical and biological variability of sensor expression. (E) Minimal RhoGEF levels are sufficient to alter the Rho GTPase activity state. HEK293T cells were cotransfected with

the indicated FRET sensors and increasing amounts of mCherry-tagged MCF2 (a promiscuous RhoGEF), together with 80 ng RhoGDI where indicated, or 80 ng mCherry. Total DNA levels were adjusted to equal amounts with miRFP empty plasmid. FRET ratio (*R*) was normalized to the 0 ng MCF2+RhoGDI control value. mCherry intensities shown in the bottom panel represent the RhoGEF expression levels. All data represent the mean of five fields of view, error bars indicate standard deviation. Significance levels were calculated by unpaired Student's t-tests versus the 0 ng MCF2+RhoGDI value. ***$p<0.001$, **$p<0.01$, *$p<0.05$, n.s.=not significant. (F) Minimal RhoGAP levels are sufficient to alter the Rho GTPase activity state. RhoGDI shRNA#2-depleted HEK293T cells were cotransfected with the indicated FRET sensors and increasing amounts of mCherry-ARHGAP1 (a RhoA GAP) or mCherry-ARHGAP22 (a Rac1 and Cdc42 GAP). Total DNA levels were adjusted to equal amounts with miRFP plasmid. FRET ratio was normalized to the 0 ng RhoGAP control value. mCherry intensities shown in the bottom panel represent the RhoGAP expression levels. All data represent the mean of five fields of view, error bars indicate standard deviation. Significance levels were calculated by unpaired Student's t-tests versus 0 ng RhoGAP. ***$p<0.001$, **$p<0.01$, *$p<0.05$, n.s. = not significant.

Figure S2

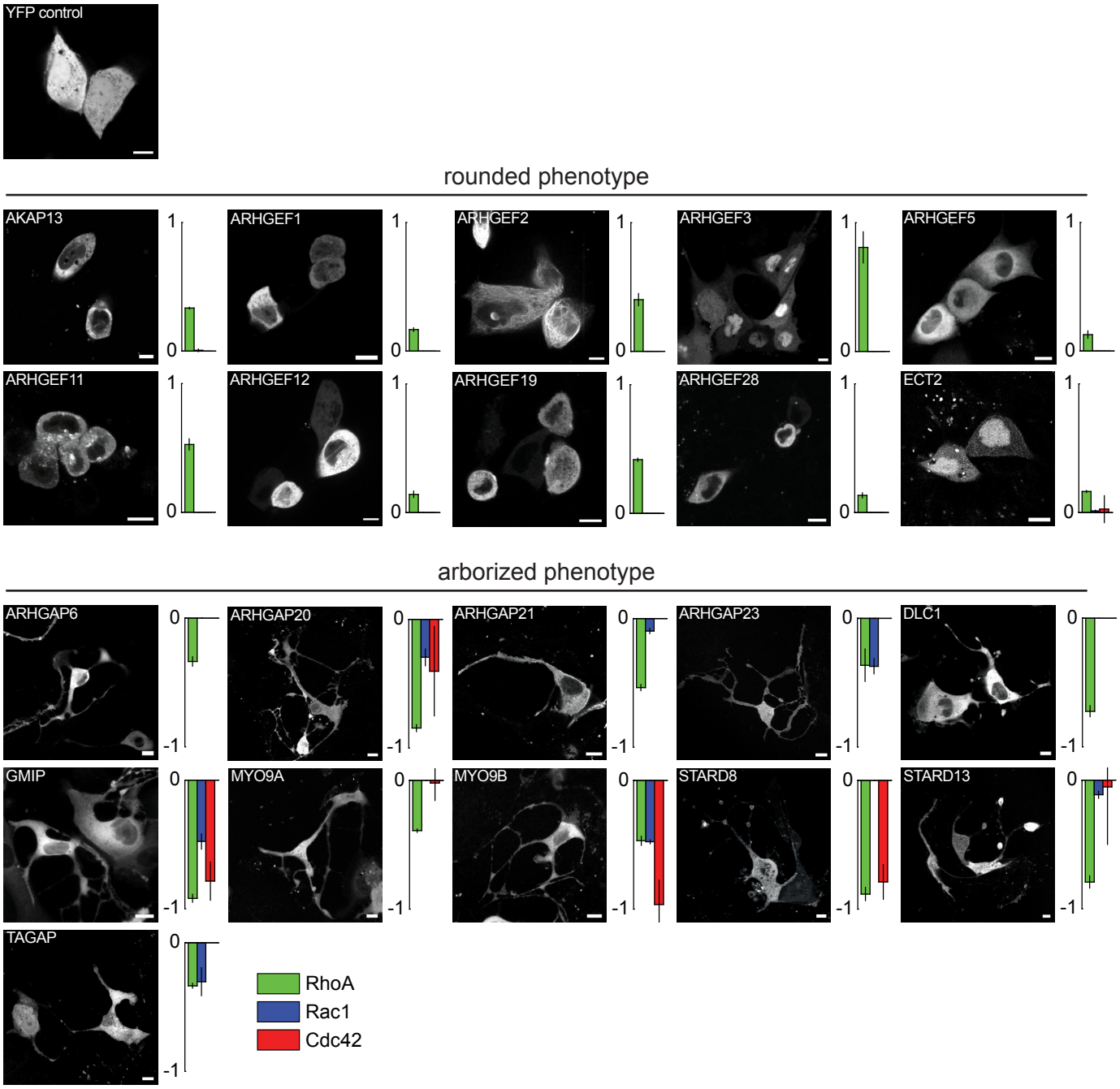
YFP control
rounded phenotype
AKAP13
ARHGEF1
ARHGEF2
ARHGEF3
ARHGEF5
ARHGEF11
ARHGEF12
ARHGEF19
ARHGEF28
ECT2
arborized phenotype
ARHGAP6
ARHGAP20
ARHGAP21
ARHGAP23
DLC1
GMIP
MYO9A
MYO9B
STARD8
STARD13
TAGAP
RhoA
Rac1
Cdc42

Figure S2. Correlation between RhoGEF/RhoGAP substrate specificity and overexpression phenotype, Related to Figure 2

Confocal micrographs of live MDCK cells transiently transfected with the indicated YFP-tagged RhoGEFs that were classified as 'rounded' (upper panel) or with the indicated RhoGAPs classified as 'arborized' (bottom panel). The respective relative catalytic activities of each RhoGEF or RhoGAP towards RhoA, Rac1 and Cdc42 are shown on the right of each micrograph as $\Delta R/\Delta R_{MAX}$ for RhoGEFs and $-\Delta R/\Delta R_{MAX}$ for RhoGAPs (see Figure 1). RhoGEFs with rounded phenotype showed exclusive substrate specificity for RhoA, RhoGAPs with arborized phenotype showed exclusive RhoA substrate specificity or, when promiscuous, strong RhoA activity. Scale bars: 10 µm.

Figure S3 (page 1/2)

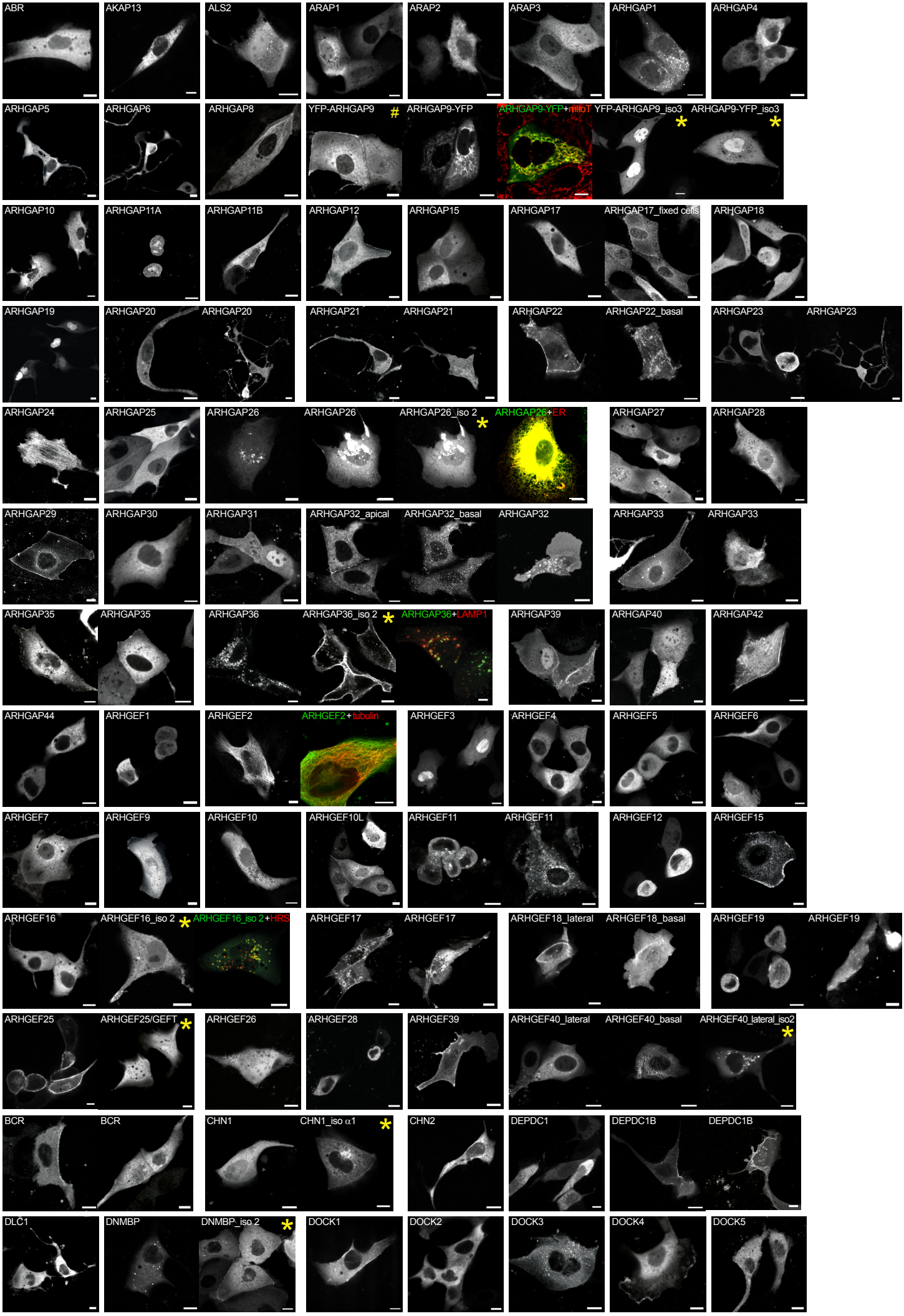

Figure S3 (page 2/2)

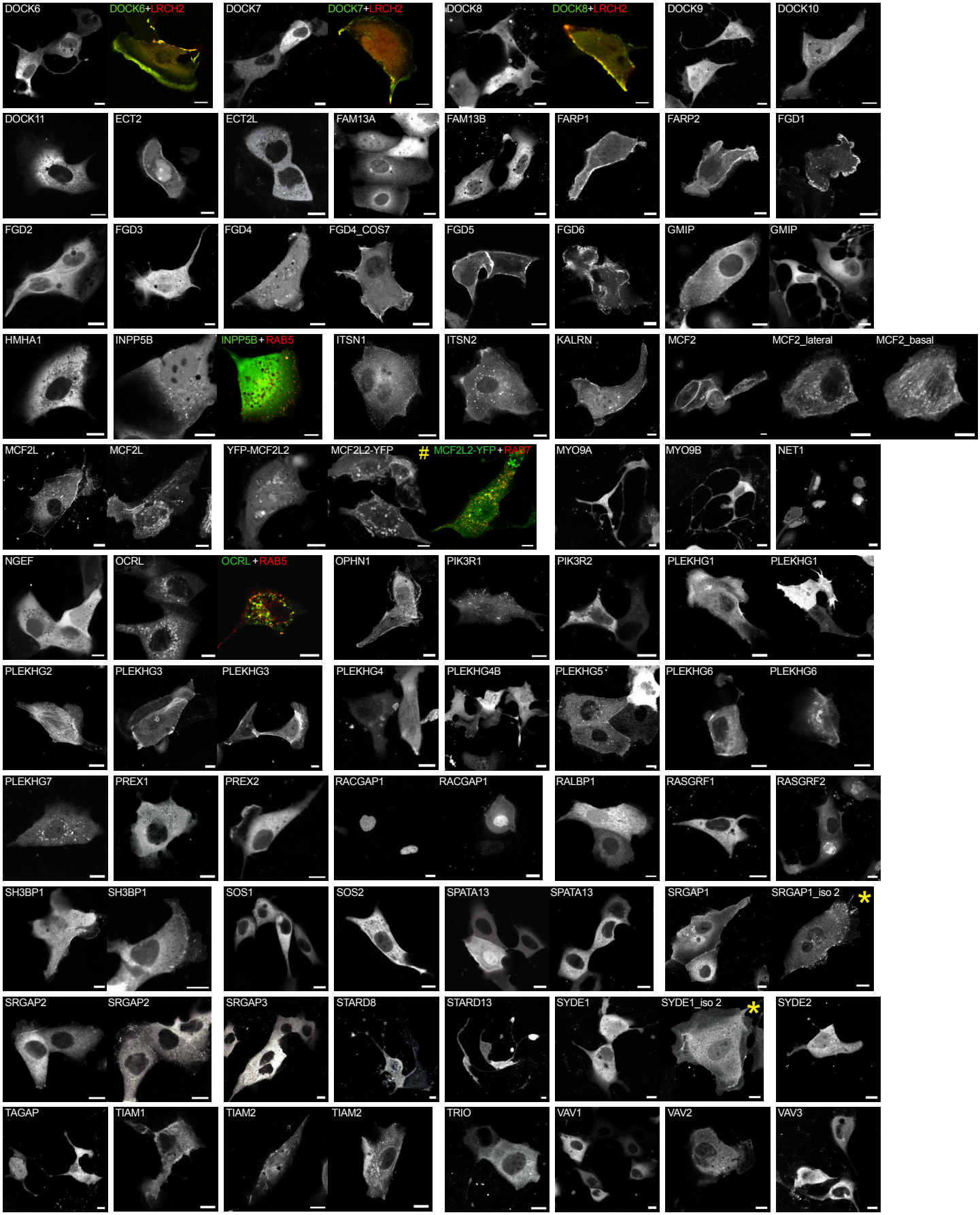

Figure S3. Steady-state subcellular localization of 141 RhoGEFs/RhoGAPs: confocal microscopy, Related to Figure 3

Confocal micrographs of live MDCK epithelial cells transiently transfected with the indicated 141 RhoGEFs and RhoGAPs in the library, revealing their diverse spatial distribution. MDCK cells were chosen because of their cuboidal shape that is well-suited for the detection of plasma membrane enriched proteins. Only cells with low expression levels were analyzed of which representative images are shown. If not otherwise denoted, N-terminal Citrine-YFP fusion constructs were used. Where required, further images are shown to document additional observations regarding their cellular distribution, their overexpression phenotypes, differences in localization between isoforms (asterisks *), N- or C-terminal tag orientation (hashes #) or live versus fixed cells, or to depict a different localization observed in COS-7 cells. In some cases, additional overlay images are shown to detail colocalization with subcellular marker proteins as indicated (ER: PTP1B-CFP, mitoT: Mitotracker). Scale bars: 10 µm.

Figure S4A (page 1/2)

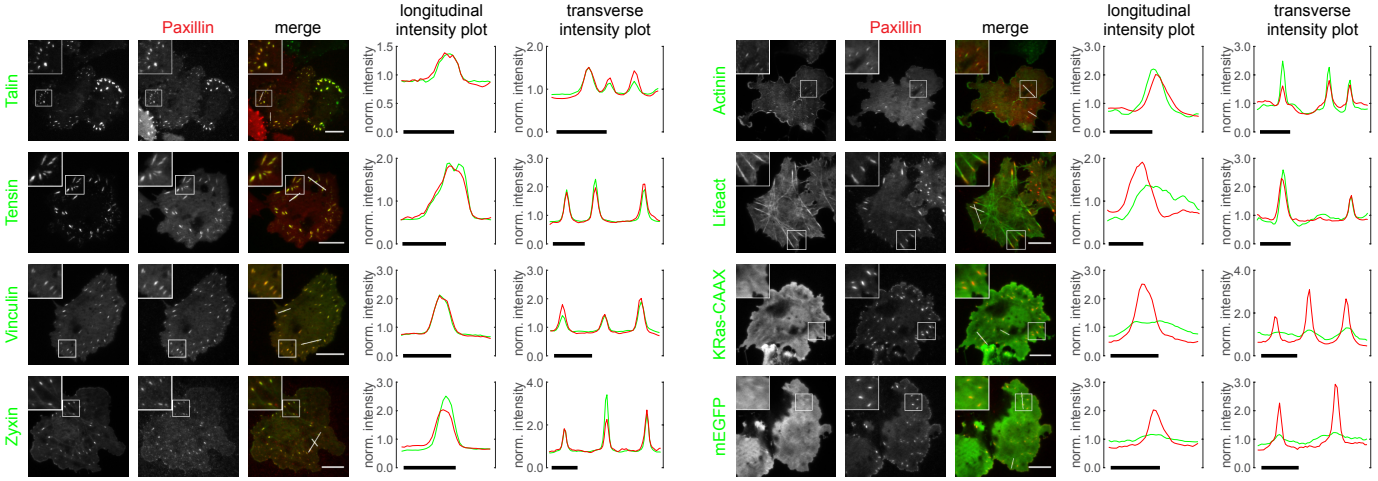

Figure S4A (page 2/2)

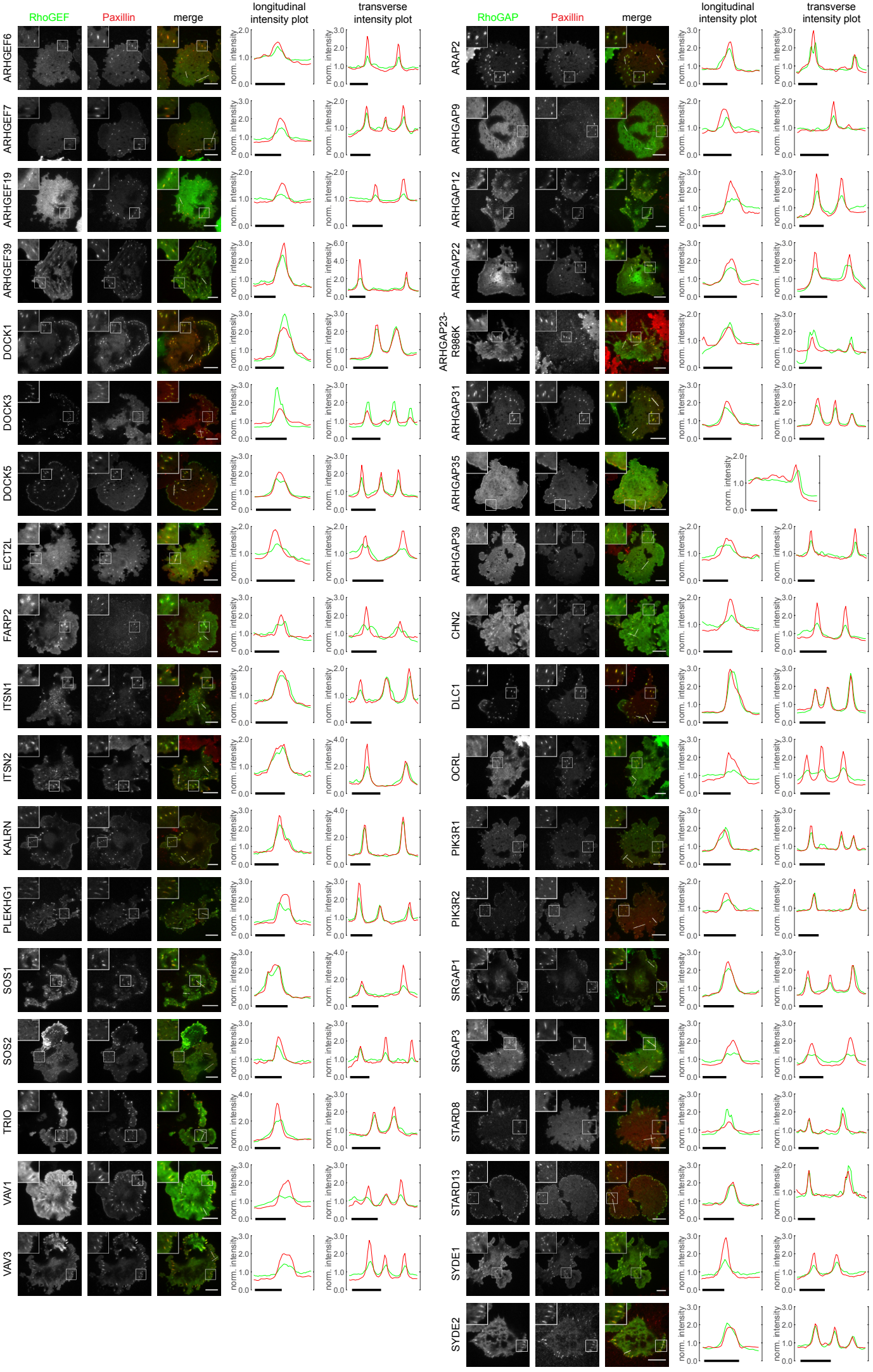

Figure S4A. TIRF microscopy screen for focal adhesion-associated RhoGEFs and RhoGAPs, Related to Figure 3

COS-7 cells stably expressing the focal adhesion marker Paxillin-mCherry, were transfected with Citrine-YFP fusion constructs of the indicated positive (upper left) or negative (upper right) control proteins, RhoGEFs (lower left) and RhoGAPs (lower right) and live-imaged by TIRF illumination. The COS-7 cell line was chosen because of its flat morphology that is well-suited for TIRF microscopy. All 37 focal adhesion-enriched regulators are displayed. Insets show magnifications of the boxed areas (green: YFP, red: Cherry). Right panels: fluorescence intensity profiles of longitudinal and transverse sections through focal adhesions (except for ARHGAP35 which is enriched in paxillin-rich regions at the lamellipodia edge), indicated by white lines in the merged images. Intensity plots were normalized to the average intensity over the whole line. Scale bars (white): 20 µm, scale bars (black): 5 µm.

Figure S4B

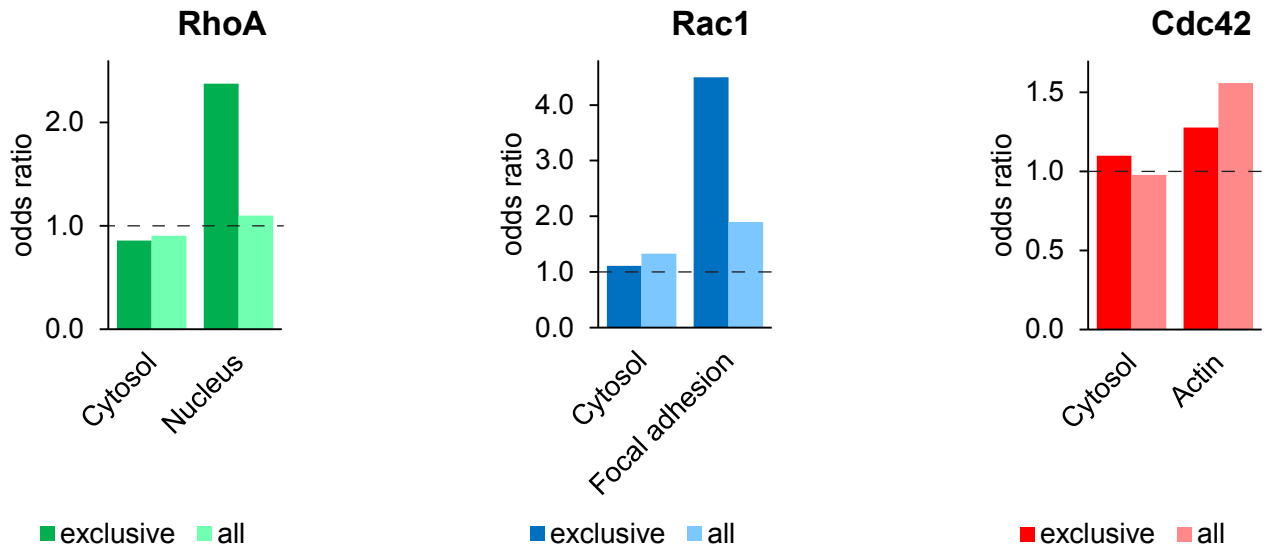
RhoA
odds ratio
2.0
1.0
0.0
Cytosol
Nucleus
exclusive
all
Rac1
odds ratio
4.0
3.0
2.0
1.0
0.0
Cytosol
Focal adhesion
exclusive
all
Cdc42
odds ratio
1.5
1.0
0.5
0.0
Cytosol
Actin
exclusive
all

Figure S4B. Substrate-specific overrepresentation of RhoGEFs/RhoGAPs in the nucleus, at focal adhesions and on actin filaments (literature data), Related to Figure 4

RhoA-, Rac1- and Cdc42-specific regulators are enriched in the nucleus, on focal adhesions and on actin, respectively. Odds ratios for enrichment of RhoGEFs and RhoGAPs with activity towards RhoA in the nucleus, with activity towards Rac1 on focal adhesions, and with activity towards Cdc42 on actin filaments (as identified by literature review). Values were calculated for RhoGEFs and RhoGAPs which had been characterised for RhoA, Rac1, and Cdc42 but showed exclusive GTPase substrate activity (exclusive) and, for comparison, for promiscuous and exclusive regulators combined (all). Dashed lines indicate no enrichment at odds ratio 1.

Figure S4C

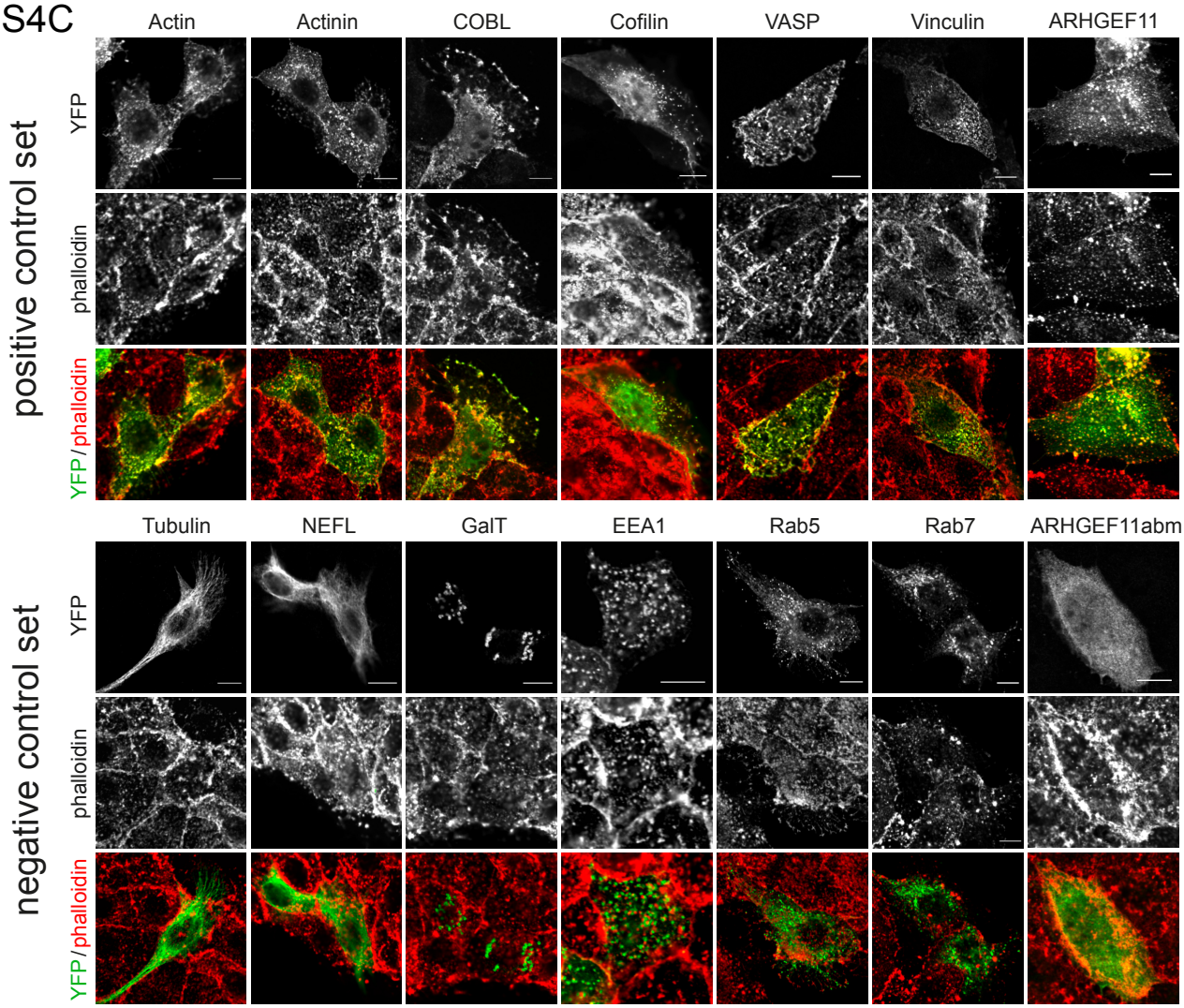
positive control set
Actin
Actinin
COBL
Cofilin
VASP
Vinculin
ARHGEF11
YFP
phalloidin
YFP / phalloidin
negative control set
Tubulin
NEFL
GalT
EEA1
Rab5
Rab7
ARHGEF11abm
YFP
phalloidin
YFP / phalloidin

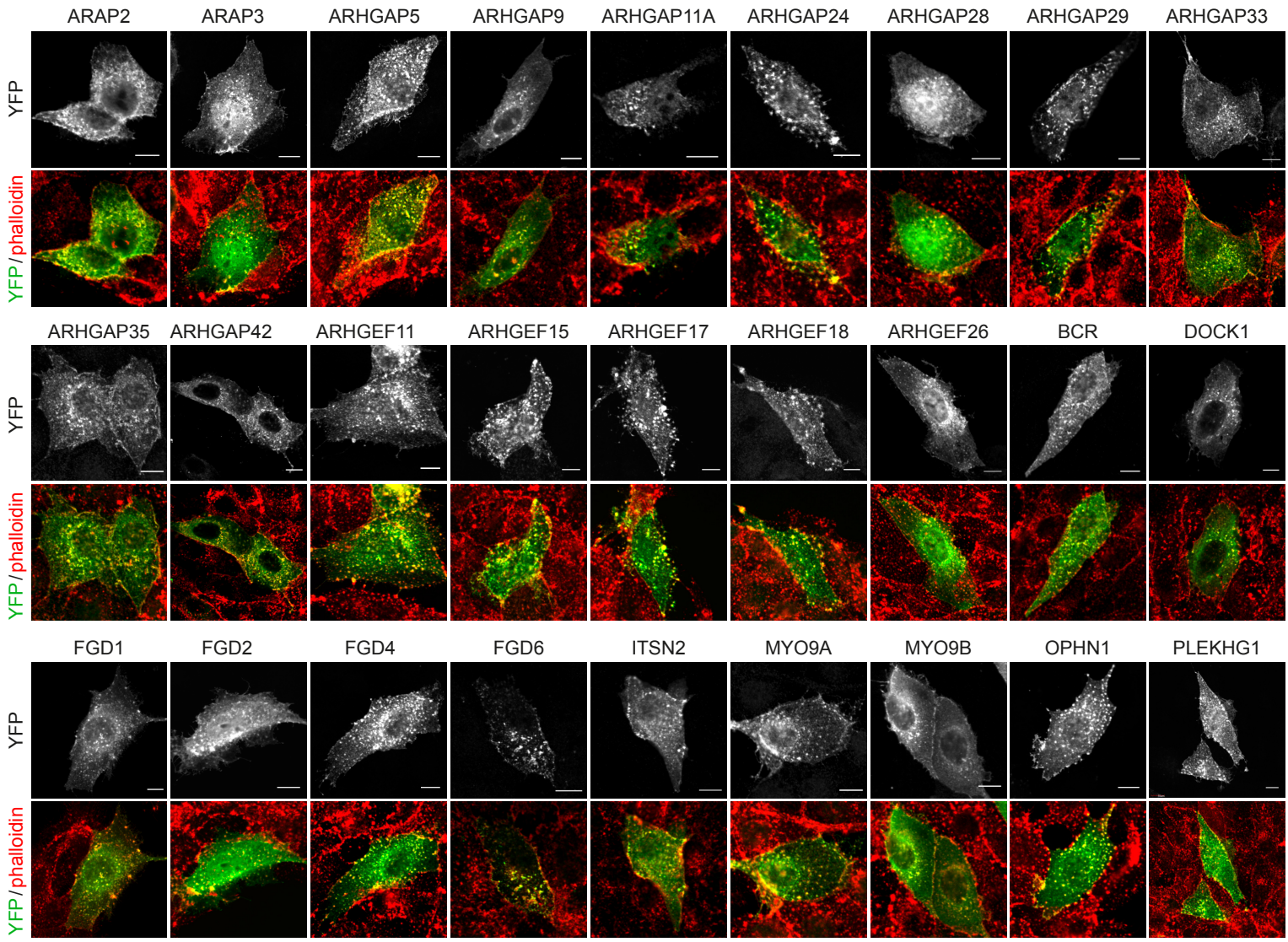
ARAP2
ARAP3
ARHGAP5
ARHGAP9
ARHGAP11A
ARHGAP24
ARHGAP28
ARHGAP29
ARHGAP33
YFP
YFP / phalloidin
ARHGAP35
ARHGAP42
ARHGEF11
ARHGEF15
ARHGEF17
ARHGEF18
ARHGEF26
BCR
DOCK1
YFP
YFP / phalloidin
FGD1
FGD2
FGD4
FGD6
ITSN2
MYO9A
MYO9B
OPHN1
PLEKHG1
YFP
YFP / phalloidin

Figure S4C. Cytochalasin D screen for actin-associated RhoGEFs and RhoGAPs, Related to Figure 3

Confocal images of MDCK cells transiently transfected with Citrine-YFP fusion constructs of the indicated positive (upper panel) or negative (middle panel) control proteins and RhoGEFs and RhoGAPs (bottom panel). Cells were treated for 30 min with Cytochalasin D, fixed and stained for actin with phalloidin. YFP signals were enhanced by anti-GFP immunofluorescence (green: YFP, red: actin in merged images). All 34 actin-associated regulators are displayed. Scale bars: 10 µm.

Figure S5A

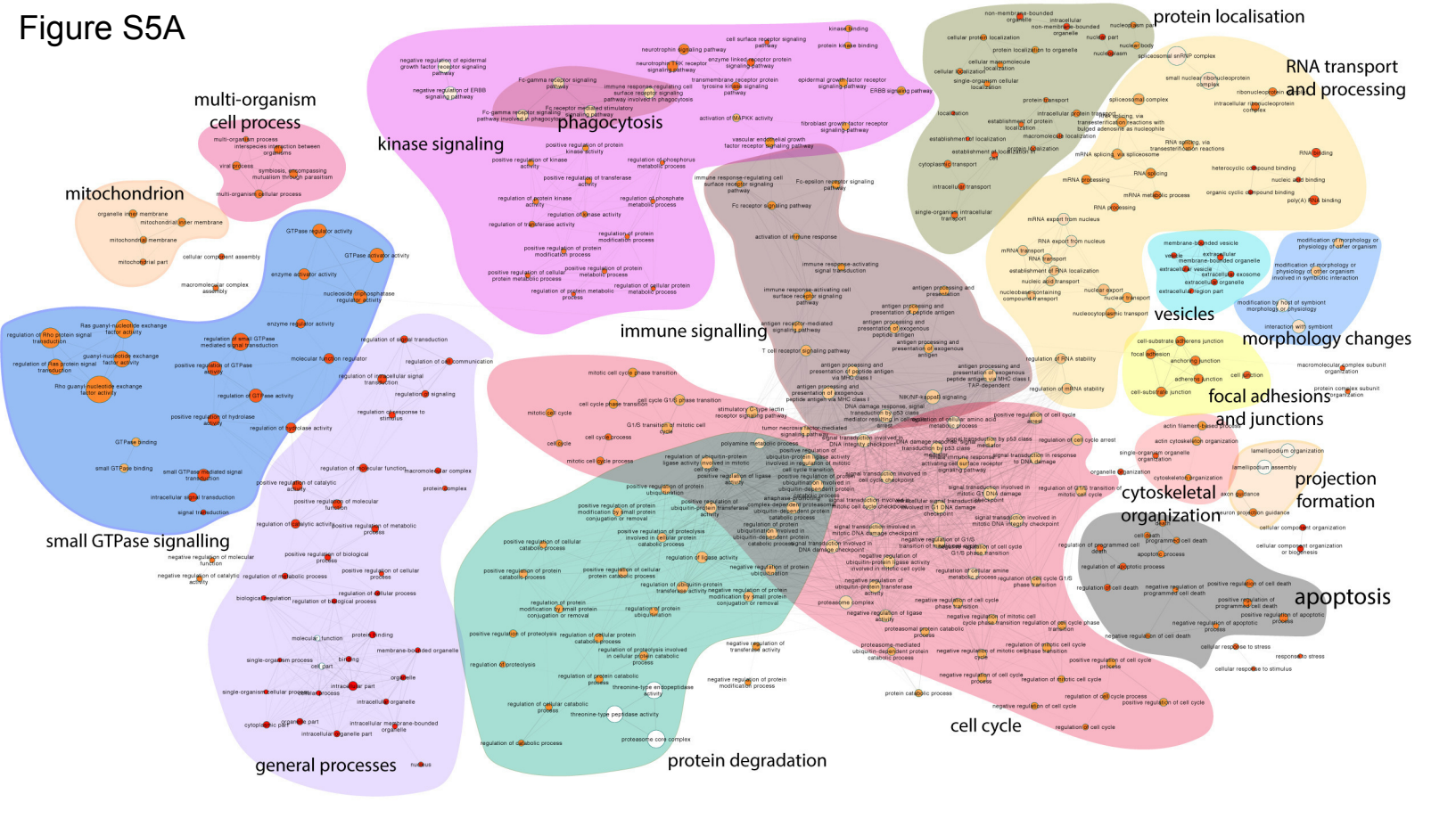
multi-organism cell process
mitochondrion
small GTPase signalling
general processes
kinase signaling
phagocytosis
immune signalling
protein degradation
cell cycle
protein localisation
RNA transport and processing
vesicles
morphology changes
focal adhesions and junctions
cytoskeletal organization
projection formation
apoptosis

Figure S5A. GO Terms enrichment analysis visualisation (Biostudies:S-BSST160)

GO Terms enrichment analysis was performed using the Funcassociate 3.0 web server (Berriz et al., 2003). Edges between GO terms were calculated using vectors of the genes included in the term and our set and calculating the Jaccard index. Results were visualized using Cytoscape (Russell and Cohn, 2012).

Figure S5B

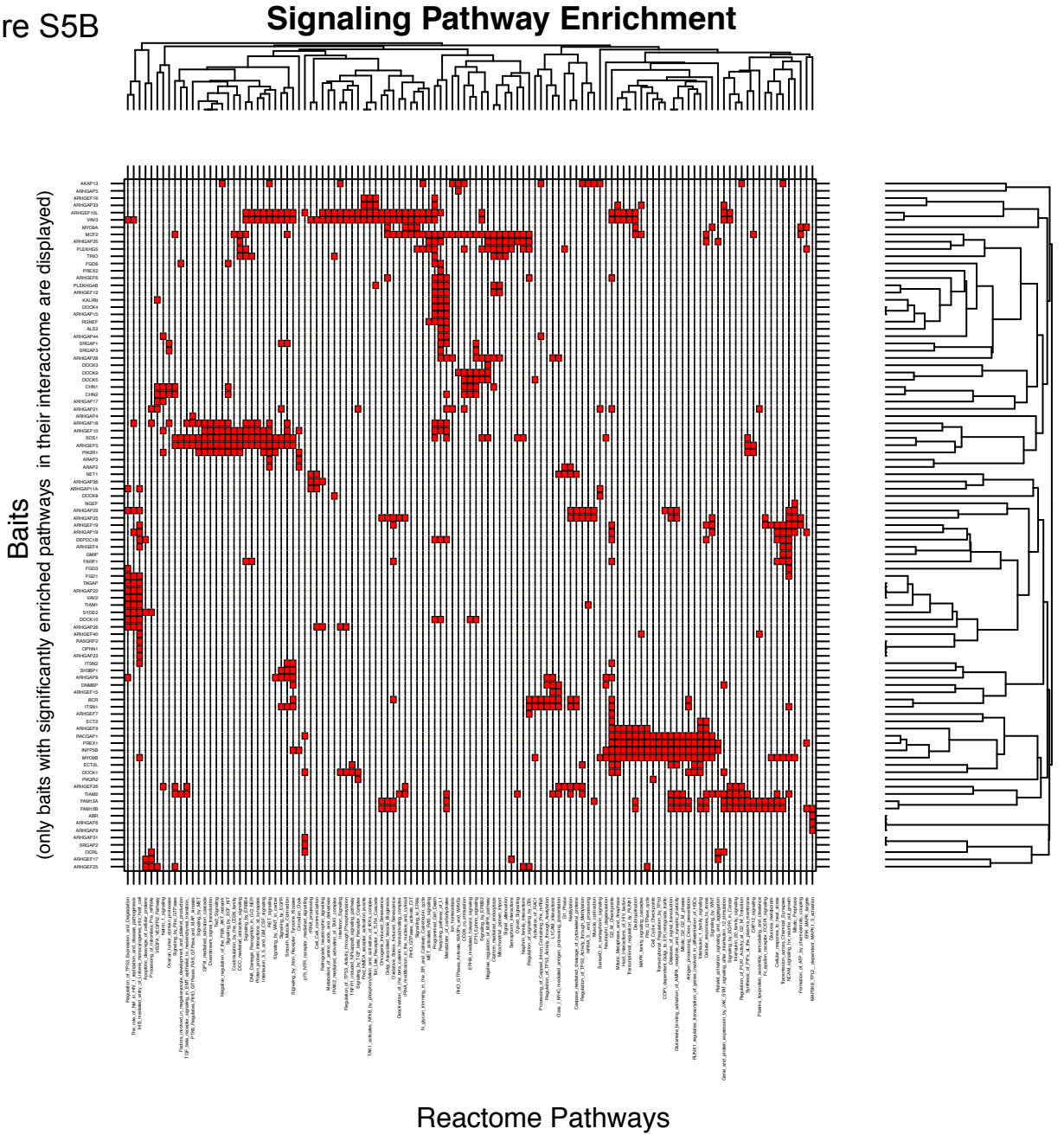
Signaling Pathway Enrichment
Baits
(only baits with significantly enriched pathways in their interactome are displayed)
Reactome Pathways

Figure S5B. Reactome pathways enrichment analysis (Biostudies:S-BSST160)

Pathway enrichment analysis (Biostudies:S-BSST160) was performed using the ReactomePA function from Bioconductor (Yu and He, 2016). Clustering was done using the hclust function in R (Murtagh and Legendre, 2014).

Figure S5C

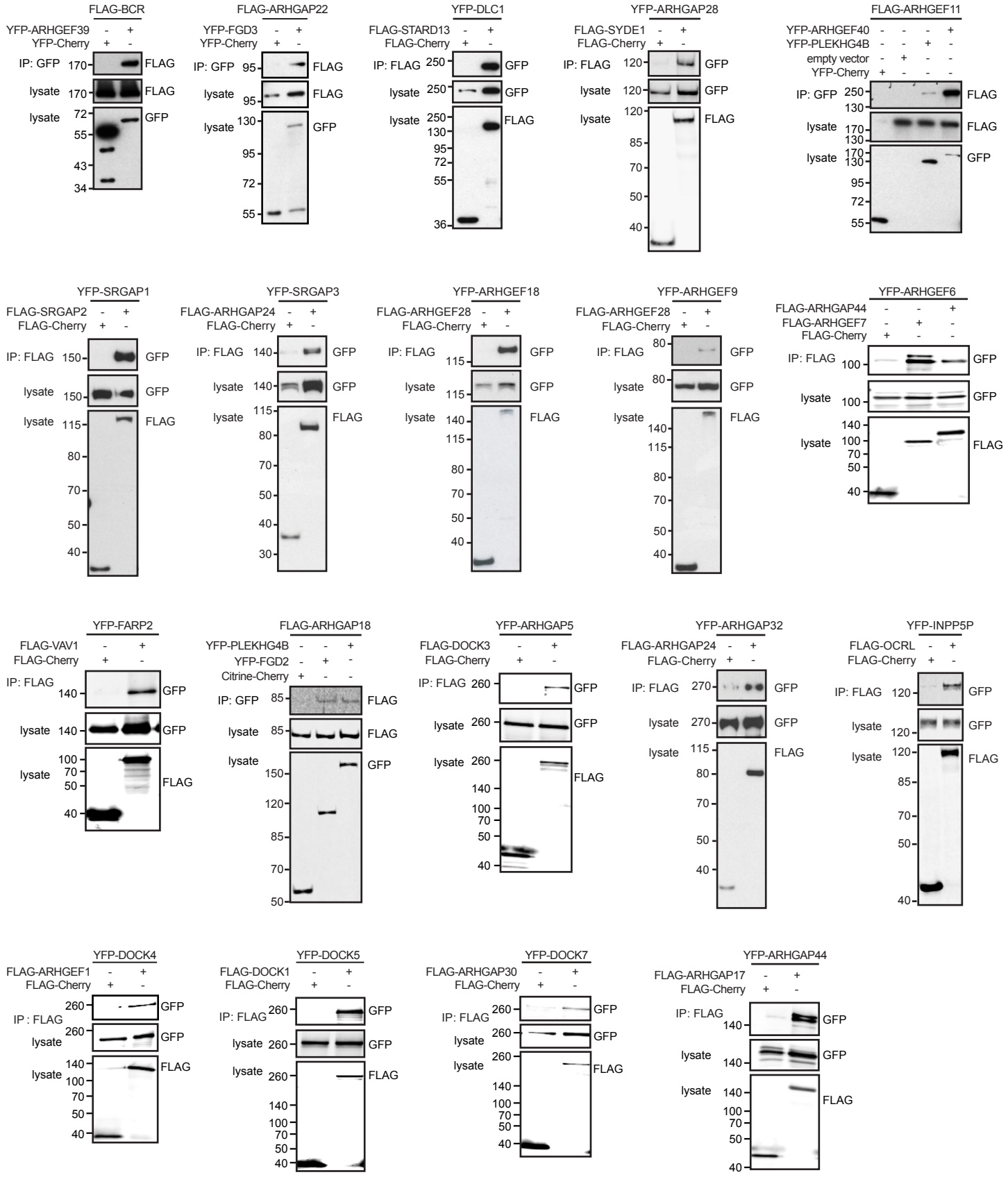
FLAG-BCR
YFP-ARHGEF39 - +
YFP-Cherry + -
IP: GFP 170 FLAG
lysate 170 FLAG
lysate 72 55 43 34 GFP
FLAG-ARHGAP22
YFP-FGD3 - +
YFP-Cherry + -
IP: GFP 95 FLAG
lysate 95 FLAG
lysate 130 95 72 55 GFP
YFP-DLC1
FLAG-STARD13 - +
FLAG-Cherry + -
IP: FLAG 250 GFP
lysate 250 GFP
lysate 250 130 95 72 55 36 FLAG
YFP-ARHGAP28
FLAG-SYDE1 - +
FLAG-Cherry + -
IP: FLAG 120 GFP
lysate 120 GFP
lysate 120 85 70 50 40 FLAG
FLAG-ARHGEF11
YFP-ARHGEF40 - - - +
YFP-PLEKHG4B - - + -
empty vector - + - -
YFP-Cherry + - - -
IP: GFP 250 130 FLAG
lysate 170 130 FLAG
lysate 170 130 95 72 55 GFP
YFP-SRGAP1
FLAG-SRGAP2 - +
FLAG-Cherry + -
IP: FLAG 150 GFP
lysate 150 GFP
lysate 115 80 70 50 40 FLAG
YFP-SRGAP3
FLAG-ARHGAP24 - +
FLAG-Cherry + -
IP: FLAG 140 GFP
lysate 140 GFP
lysate 115 80 70 50 40 30 FLAG
YFP-ARHGEF18
FLAG-ARHGEF28 - +
FLAG-Cherry + -
IP: FLAG 115 GFP
lysate 115 GFP
lysate 140 115 80 70 50 40 FLAG
YFP-ARHGEF9
FLAG-ARHGEF28 - +
FLAG-Cherry + -
IP: FLAG 80 GFP
lysate 80 GFP
lysate 140 115 80 70 50 40 FLAG
YFP-ARHGEF6
FLAG-ARHGAP44 - - +
FLAG-ARHGEF7 - + -
FLAG-Cherry + - -
IP: FLAG 100 GFP
lysate 100 GFP
lysate 140 100 70 50 40 FLAG
YFP-FARP2
FLAG-VAV1 - +
FLAG-Cherry + -
IP: FLAG 140 GFP
lysate 140 GFP
lysate 100 70 50 40 FLAG
FLAG-ARHGAP18
YFP-PLEKHG4B - - +
YFP-FGD2 - + -
Citrine-Cherry + - -
IP: GFP 85 FLAG
lysate 85 FLAG
lysate 150 120 85 70 50 GFP
YFP-ARHGAP5
FLAG-DOCK3 - +
FLAG-Cherry + -
IP: FLAG 260 GFP
lysate 260 GFP
lysate 260 140 100 70 50 40 FLAG
YFP-ARHGAP32
FLAG-ARHGAP24 - +
FLAG-Cherry + -
IP: FLAG 270 GFP
lysate 270 GFP
lysate 115 80 70 50 40 FLAG
YFP-INPP5P
FLAG-OCRL - +
FLAG-Cherry + -
IP: FLAG 120 GFP
lysate 120 GFP
lysate 120 85 70 50 40 FLAG
YFP-DOCK4
FLAG-ARHGEF1 - +
FLAG-Cherry + -
IP : FLAG 260 GFP
lysate 260 GFP
lysate 140 100 70 50 40 FLAG
YFP-DOCK5
FLAG-DOCK1 - +
FLAG-Cherry + -
IP: FLAG 260 GFP
lysate 260 GFP
lysate 260 140 100 70 50 40 FLAG
YFP-DOCK7
FLAG-ARHGAP30 - +
FLAG-Cherry + -
IP: FLAG 260 GFP
lysate 260 GFP
lysate 260 140 100 70 50 40 FLAG
YFP-ARHGAP44
FLAG-ARHGAP17 - +
FLAG-Cherry + -
IP: FLAG 140 GFP
lysate 140 GFP
lysate 140 100 70 50 40 FLAG

Figure S5C. Validation of interactions between RhoGEFs and RhoGAPs identified by mass spectrometry, Related to Figure 5

To assess the quality of the network dataset, lysates of HEK293T cells transfected with the indicated Citrine-YFP- and FLAG-tagged regulators or controls were IP-ed as indicated using either a FLAG or a GFP antibody and subsequently immunoblotted using a corresponding GFP or FLAG antibody. Protein bands were detected either by chemiluminescence or using a gel imaging system. 22 out of 26 RhoGEF/RhoGAP pairs tested could be successfully validated.

Figure S6

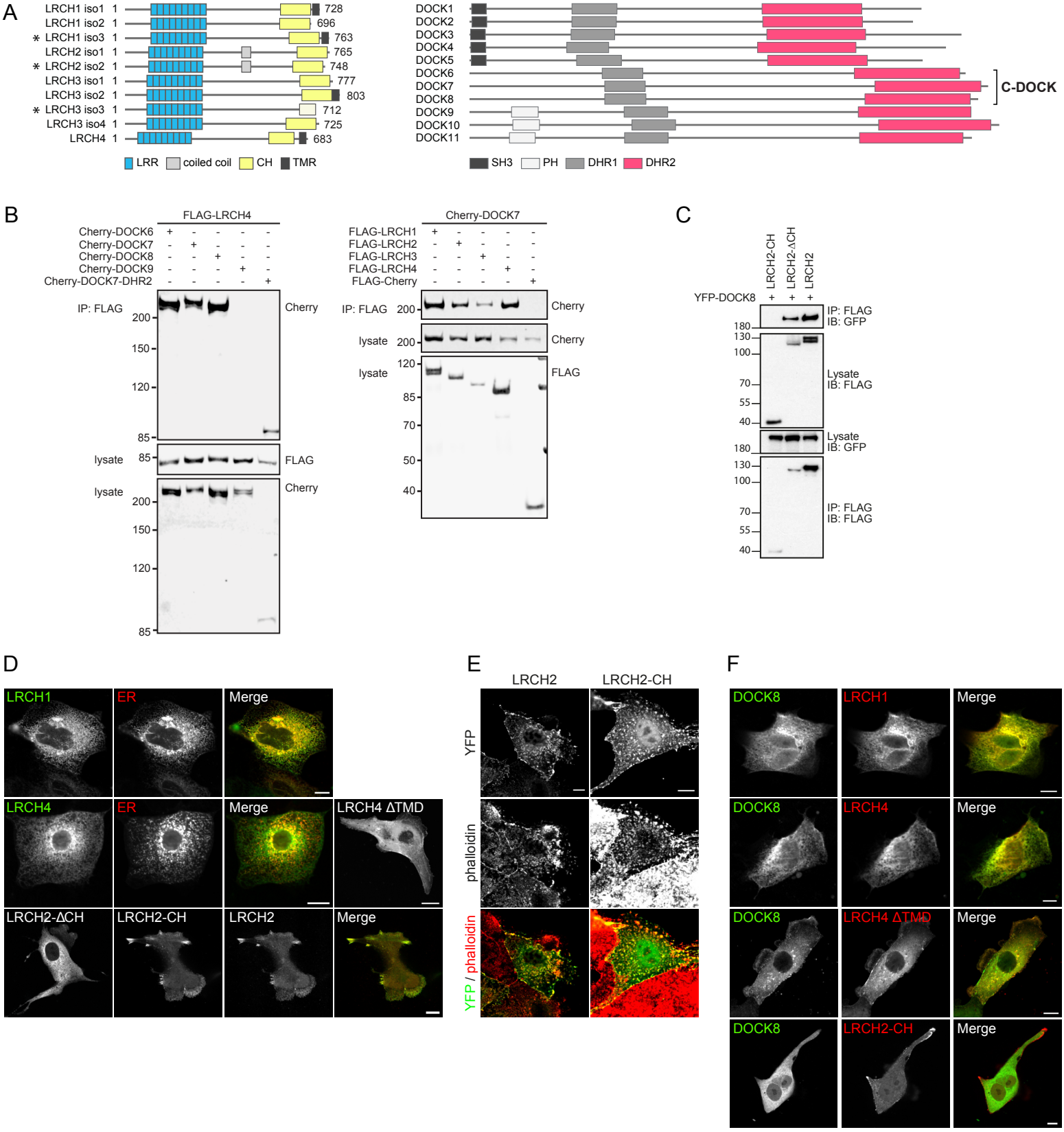
A
LRCH1 iso1 1 728
LRCH1 iso2 1 696
* LRCH1 iso3 1 763
LRCH2 iso1 1 765
* LRCH2 iso2 1 748
LRCH3 iso1 1 777
LRCH3 iso2 1 803
* LRCH3 iso3 1 712
LRCH3 iso4 1 725
LRCH4 1 683
LRR
coiled coil
CH
TMR
DOCK1
DOCK2
DOCK3
DOCK4
DOCK5
DOCK6
DOCK7
DOCK8
DOCK9
DOCK10
DOCK11
C-DOCK
SH3
PH
DHR1
DHR2
B
FLAG-LRCH4
Cherry-DOCK6
Cherry-DOCK7
Cherry-DOCK8
Cherry-DOCK9
Cherry-DOCK7-DHR2
IP: FLAG
Cherry
lysate
FLAG
Cherry-DOCK7
FLAG-LRCH1
FLAG-LRCH2
FLAG-LRCH3
FLAG-LRCH4
FLAG-Cherry
C
LRCH2-CH
LRCH2-ΔCH
LRCH2
YFP-DOCK8
IP: FLAG
IB: GFP
Lysate
IB: FLAG
Lysate
IB: GFP
IP: FLAG
IB: FLAG
D
LRCH1
ER
Merge
LRCH4
LRCH4 ΔTMD
LRCH2-ΔCH
LRCH2-CH
LRCH2
E
LRCH2
LRCH2-CH
YFP
phalloidin
YFP / phalloidin
F
DOCK8
LRCH1
LRCH4
LRCH4 ΔTMD
LRCH2-CH

Figure S6. C-DOCK subfamily RhoGEFs interact with LRCH family proteins, Related to Figure 6

(A) Domain architecture of the human LRCH and DOCK family proteins. Asterisks mark LRCH protein isoforms used in this study. Note the compromised CH domain in LRCH3 isoform 3 which many account for its cytosolic localization (see also (E) below). LRR: Leucin rich repeats; CH: Calponin homology; TMR: transmembrane region; SH3: Src homology 3; PH: Pleckstrin homology; DHR: DOCK homology region. (B) C-DOCK RhoGEFs associate with LRCH proteins. Left panel: LRCH4 specifically binds C-DOCK family proteins, the DHR2 domain is sufficient for the interaction. Lysates of HEK293T cells cotransfected with FLAG-LRCH4 and the indicated mCherry-tagged DOCK proteins or DOCK7 fragment were IP-ed using a FLAG antibody and immunoblotted using a Cherry antibody. Right panel: DOCK7 binds all LRCH family proteins. Lysates of HEK293T cells cotransfected with mCherry-DOCK7 and the indicated FLAG-tagged LRCH proteins or FLAG-Cherry control were IP-ed using a FLAG antibody and immunoblotted using a Cherry antibody. (C) The Leucine rich repeats likely mediate the LRCH-DOCK interaction while the CH domain is dispensable. Lysates of HEK293T cells cotransfected with YFP-DOCK8 and FLAG-tagged LRCH2 full-length or truncation constructs were IP-ed using a FLAG antibody and immunoblotted using a GFP antibody. (D) Confocal micrographs of live MDCK cells coexpressing CFP-LRCH1 (upper panel) or CFP-LRCH4 (middle panel) together with the endoplasmic reticulum (ER) marker protein PTP1B-YFP, revealing their colocalization. Both LRCH proteins contain predicted C-terminal type II-transmembrane signals (TMHMM2.0 tool (Krogh et al., 2001)). Truncation of this signal in LRCH4 (LRCH4-ΔTMD; middle panel, right image) causes its relocalization from the ER to the cell periphery. Lower panel: the CH domain of LRCH2 is sufficient for its localization to the cell periphery. (E) Cytochalasin D experiment as shown in Figure S4C, revealing actin coaggregation both of LRCH2 full-length and of a CH domain fragment, suggesting that the CH domains of LRCH proteins mediate their targeting to peripheral actin structures in cells. (F) Confocal micrographs of live MDCK cells coexpressing CFP-DOCK8 and the indicated LRCH proteins and fragments thereof, showing the recruitment of DOCK8 to the ER by LRCH1 and LRCH4, or to the cell periphery by LRCH4-ΔTMR. LRCH2-CH, lacking the Leucine rich repeats, cannot recruit DOCK8 to the cell periphery. All scale bars: 10 μm.

Figure S7

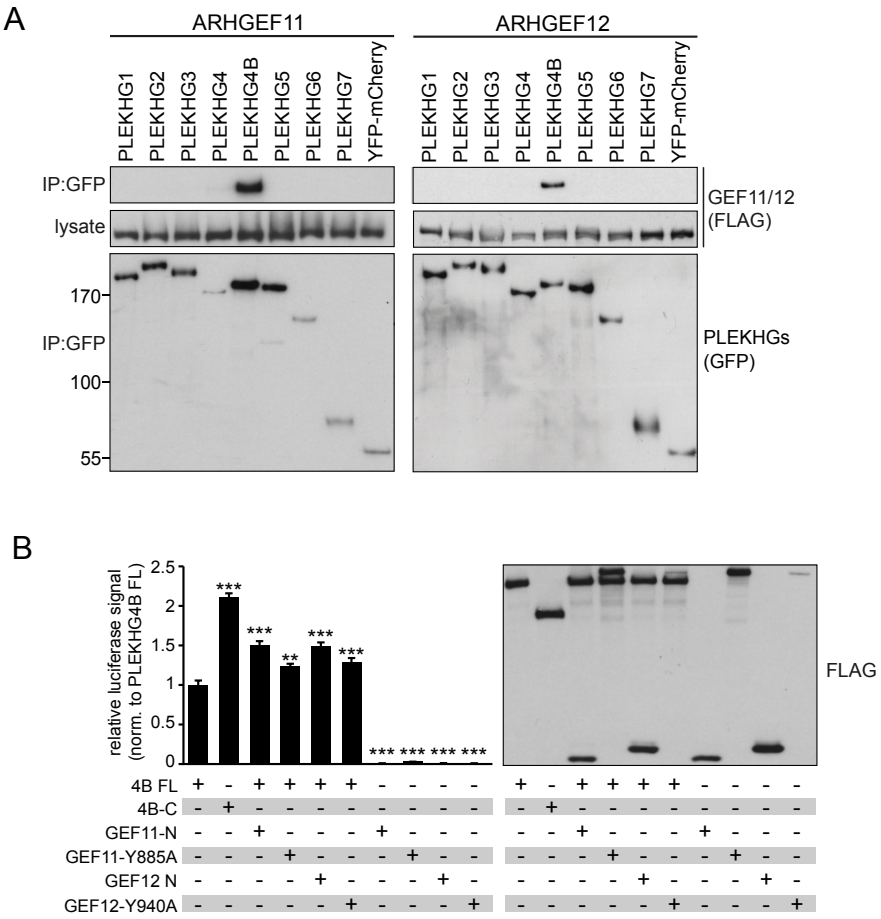
A
ARHGEF11
ARHGEF12
PLEKHG1
PLEKHG2
PLEKHG3
PLEKHG4
PLEKHG4B
PLEKHG5
PLEKHG6
PLEKHG7
YFP-mCherry
IP:GFP
lysate
GEF11/12
(FLAG)
170
IP:GFP
100
55
PLEKHGs
(GFP)
B
relative luciferase signal
(norm. to PLEKHG4B FL)
2.5
2
1.5
1
0.5
0
***
**
FLAG
4B FL
4B-C
GEF11-N
GEF11-Y885A
GEF12 N
GEF12-Y940A

Figure S7. Characterization of the PLEKHG4B/ARHGEF11/ARHGEF12 multi-RhoGEF complex, related to Figure 7

(A) ARHGEF11 and ARHGEF12 specifically interact with PLEKHG4B. HEK293T cells were transfected with Citrine YFP-fusions of all eight PLEKHG family proteins or with YFP-mCherry control together with FLAG-ARHGEF11 (left panel) or FLAG-ARHGEF12 (right panel). Lysates were IP-ed using a GFP antibody and immunoblotted using GFP or FLAG antibodies. (B) PLEKHG4B autoinhibition is released by ARHGEF11 and ARHGEF12. Anti-FLAG Western Blot corresponding to the SRE-luciferase reporter activation data presented in Figure 7E, showing the expression of the transfected constructs.

Figure S8 (page 1/7) UNCROPPED WESTERN BLOTS

FIGURE S1B

RhoGDI knockdown

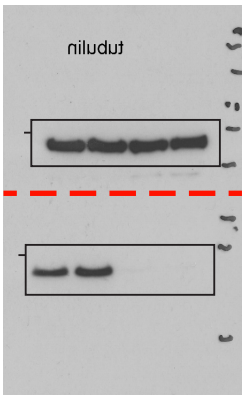

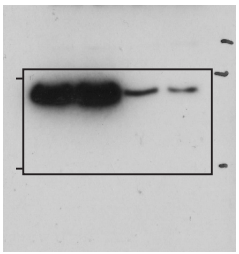

FIGURE S5

IP: YFP-ARHGEF39
Co-IP: FLAG-BCR
FLAG

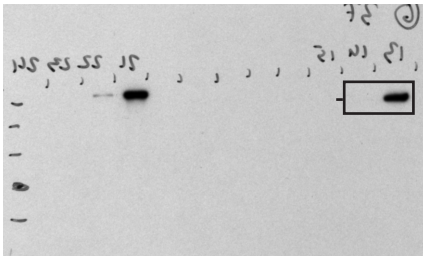

lysate FLAG

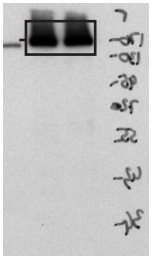

lysate GFP

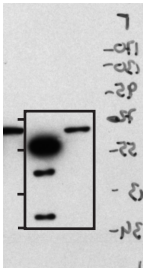

IP: YFP-FGD3
Co-IP: FLAG-ARHGAP22
FLAG

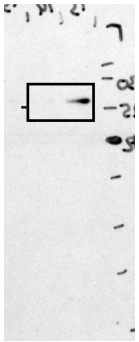

lysate FLAG

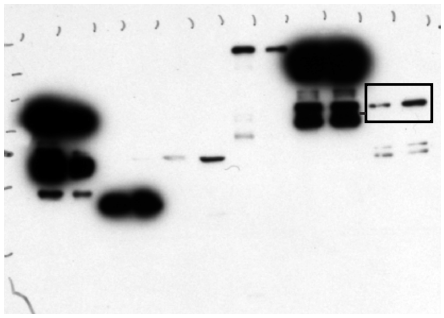

lysate GFP

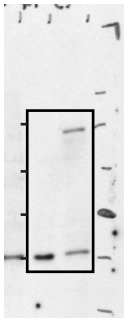

IP: FLAG-STARD13
Co-IP: YFP-DLC1
GFP

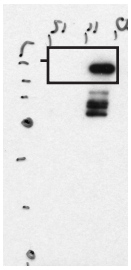

lysate GFP

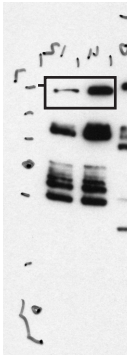

lysate FLAG

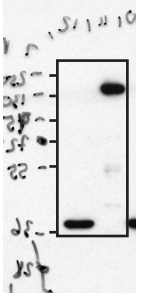

IP: FLAG-SYDE1
Co-IP: YFP-ARHGAP28
GFP

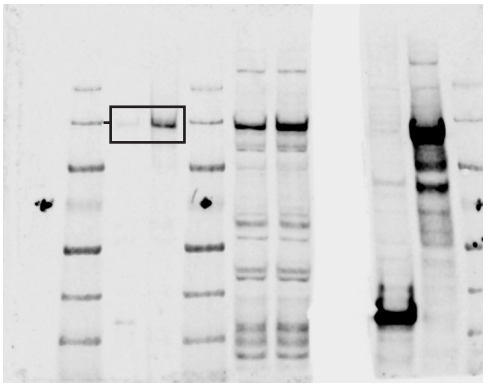

lysate GFP

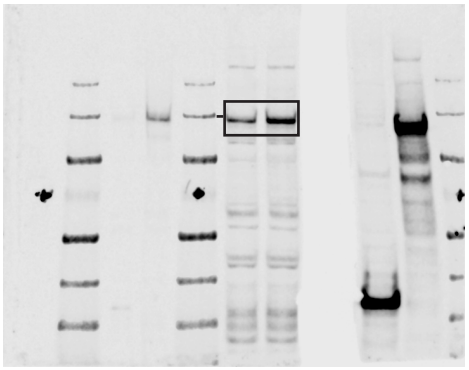

lysate FLAG

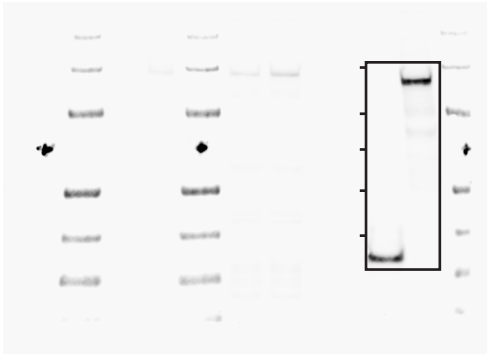

Figure S8 (page 2/7)

FIGURE S5

IP: YFP-ARHGEF40 IP: YFP-PLEKHG4B
Co-IP: FLAG-ARHGEF11
FLAG

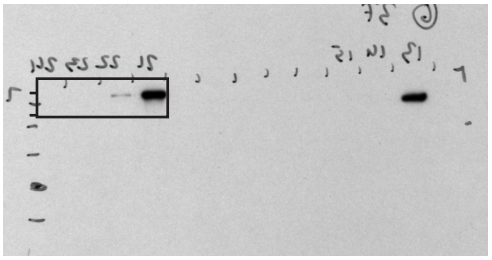

lysate FLAG

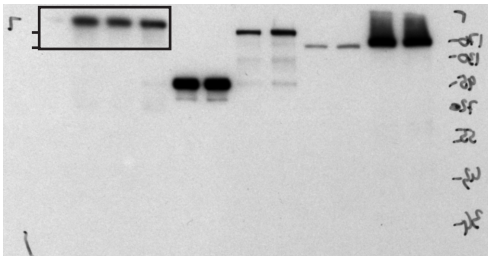

lysate GFP

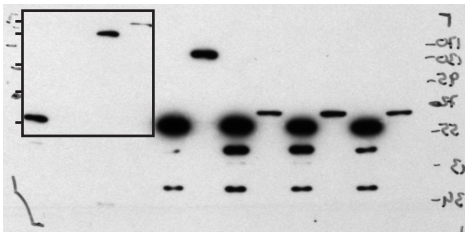

IP: FLAG-ARHGAP24
Co-IP: YFP-SRGAP3
GFP

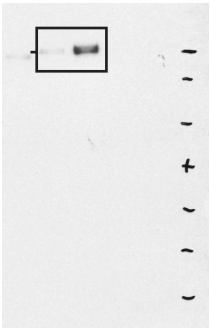

lysate GFP

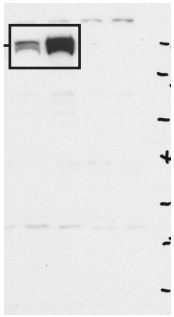

lysate FLAG

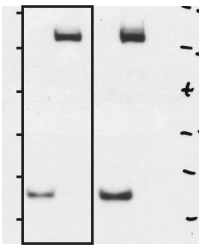

IP: FLAG-ARHGEF28
Co-IP: YFP-ARHGEF18
GFP

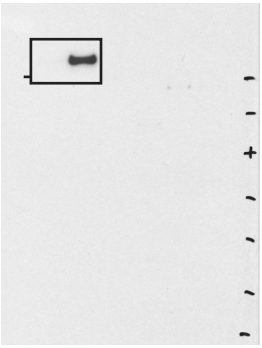

lysate GFP

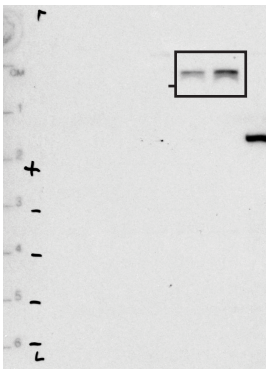

lysate FLAG

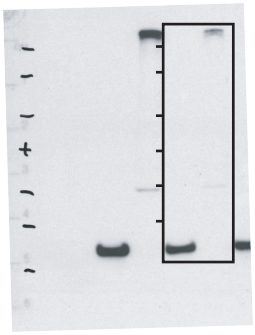

IP: FLAG-ARHGEF28
Co-IP: YFP-ARHGEF9
GFP

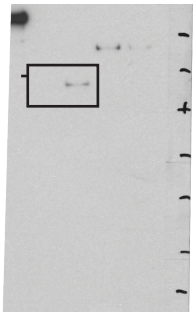

lysate GFP

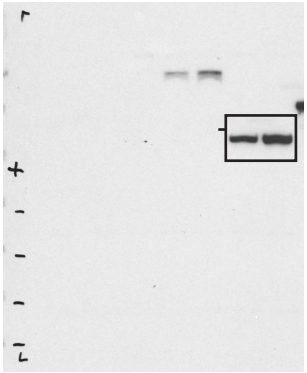

lysate FLAG

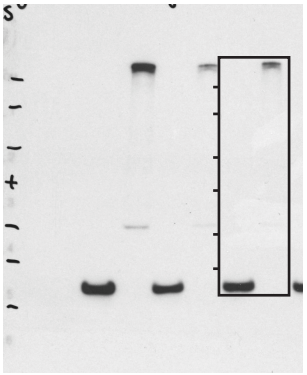

Figure S8 (page 3/7)

FIGURE S5

IP: FLAG-ARHGAP24
Co-IP: YFP-ARHGAP32
GFP

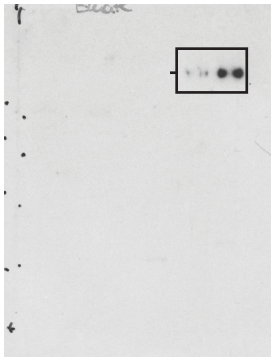

lysate GFP

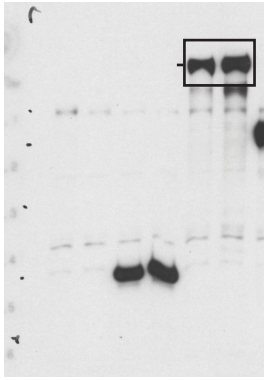

lysate FLAG

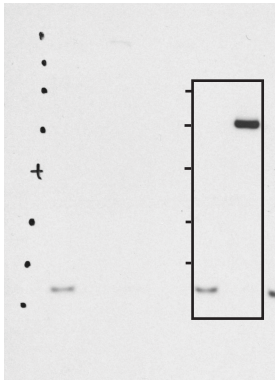

IP: YFP-PLEKHG4B IP: YFP-FGD2
Co-IP: FLAG-ARHGAP18
FLAG

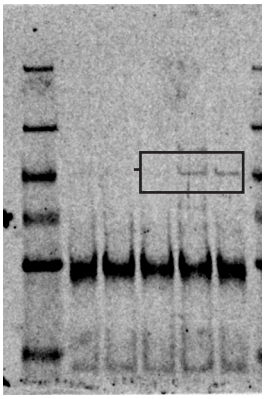

lysate FLAG

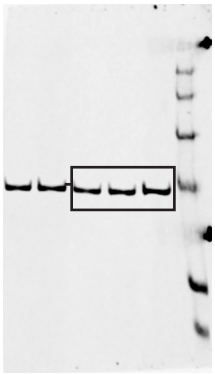

lysate GFP

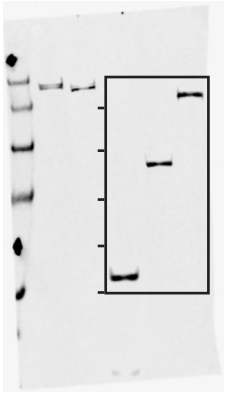

IP: FLAG-VAV1
Co-IP: YFP-FARP2
GFP

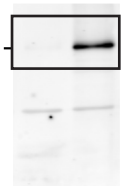

lysate GFP

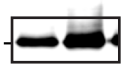

lysate FLAG

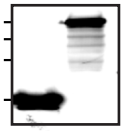

IP: FLAG-DOCK3
Co-IP: YFP-ARHGAP5
GFP

lysate GFP

lysate FLAG

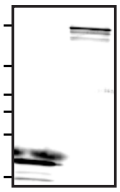

IP: FLAG-ARHGAP17
Co-IP: YFP-ARHGAP44
GFP

lysate GFP

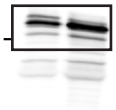

lysate FLAG

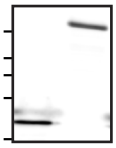

IP: FLAG-OCRL
Co-IP: YFP-INPP5P
GFP

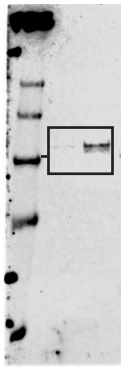

lysate GFP

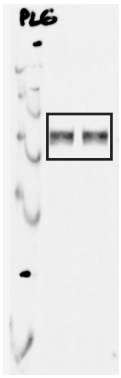

lysate FLAG

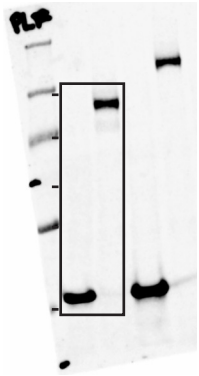

Figure S8 (page 4/7)

FIGURE S5

IP: FLAG-SRGAP2
CO-IP: YFP-SRGAP1
GFP

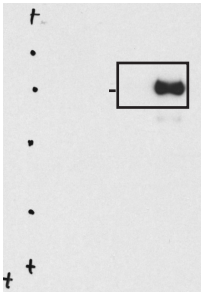

lysate GFP

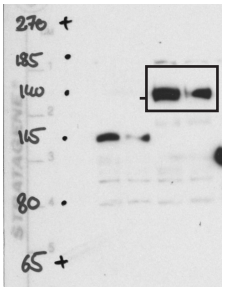

lysate FLAG

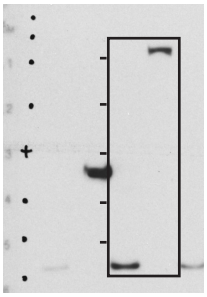

IP: FLAG-GAP44 IP: FLAG-GEF7
Co-IP: YFP-ARHGEF6
GFP

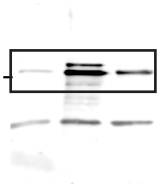

lysate GFP

lysate FLAG

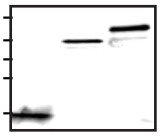

IP: FLAG-GAP30
Co-IP: YFP-DOCK7
GFP

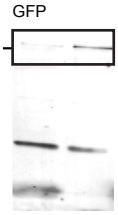

lysate GFP

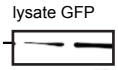

lysate FLAG

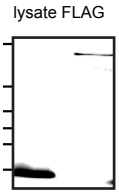

IP: FLAG-DOCK1
Co-IP: YFP-DOCK5
GFP

lysate GFP

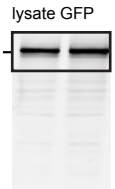

lysate FLAG

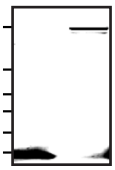

IP: FLAG-GEF1
Co-IP: YFP-DOCK4
GFP

lysate GFP

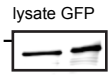

lysate FLAG

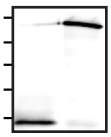

Figure S8 (page 5/7)

FIGURE 6B

IP: FLAG-ARHGAP39
IP: FLAG-ARHGAP39 WW2 Y81A
IP: FLAG-ARHGAP39 delWW
Co-IP: YFP-PEAK1

GFP

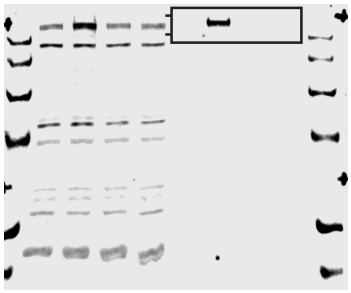

lysate GFP

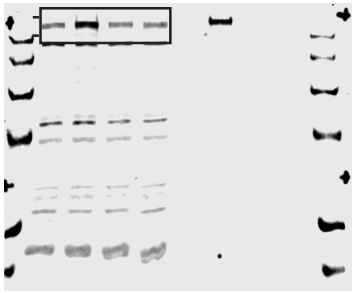

lysate FLAG

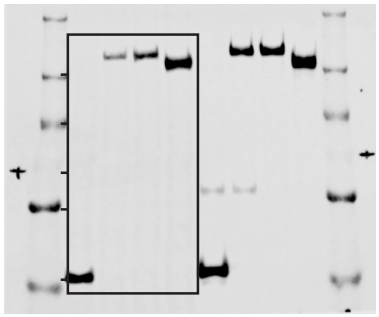

FIGURE S6C

IP: FLAG-LRCH4
Co-IP: Cherry-DOCK6
Co-IP: Cherry-DOCK7
Co-IP: Cherry-DOCK8
Co-IP: Cherry-DOCK9

lysate Cherry Cherry

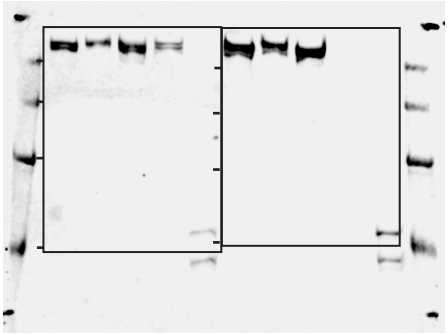

lysate FLAG

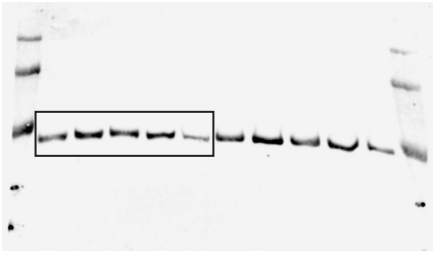

IP: FLAG-LRCH1
IP: FLAG-LRCH2
IP: FLAG-LRCH3
IP: FLAG-LRCH4
Co-IP: Cherry-DOCK7

lysate Cherry Cherry

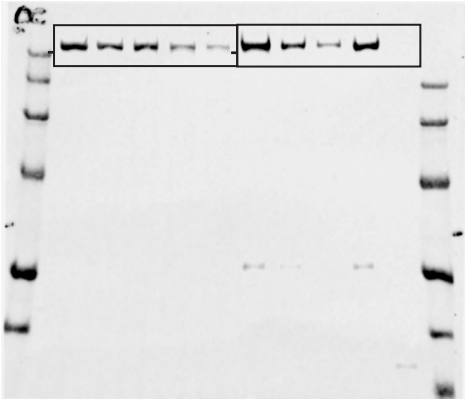

lysate FLAG

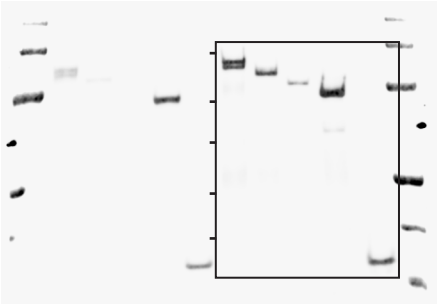

FIGURE S6D

IP: FLAG-LRCH2-CH
IP: FLAG-LRCH2-ΔCH
IP: FLAG-LRCH2
Co-IP: YFP-DOCK8

GFP

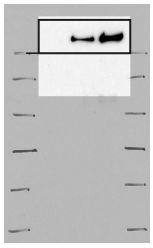

FLAG

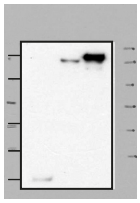

lysate GFP

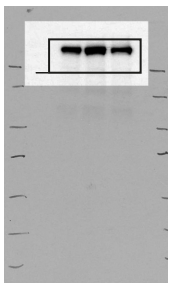

lysate FLAG

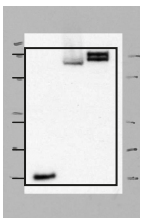

Figure S8 (page 6/7)

FIGURE 7B

IP: YFP-PLEKHG4B
Co-IP: FLAG-ARHGEF11/12

lysate FLAG FLAG

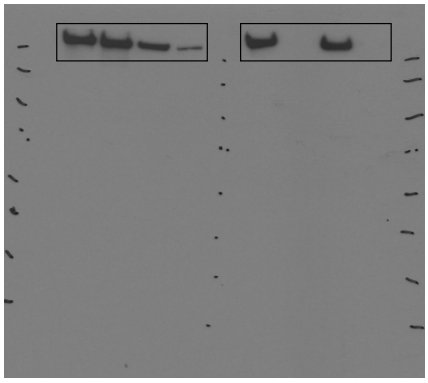

lysate GFP GFP

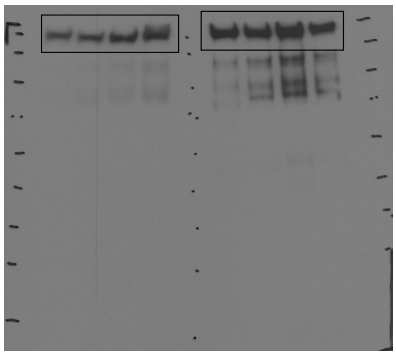

IP: YFP-PLEKHG4B
Co-IP: FLAG-ARHGEF11

lysate FLAG FLAG

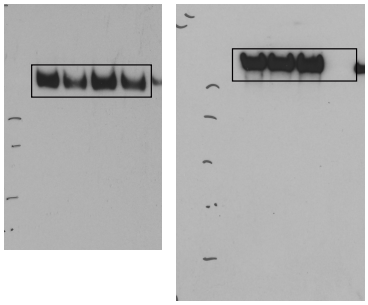

lysate GFP GFP

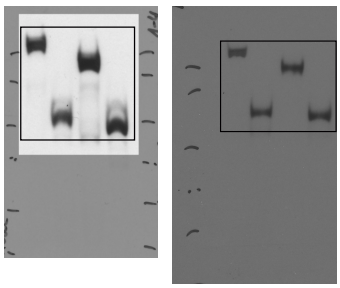

IP: YFP-PLEKHG4B
Co-IP: FLAG-ARHGEF12

lysate FLAG FLAG

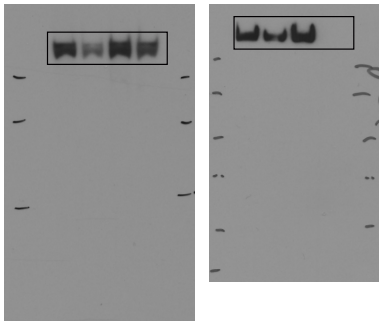

lysate GFP GFP

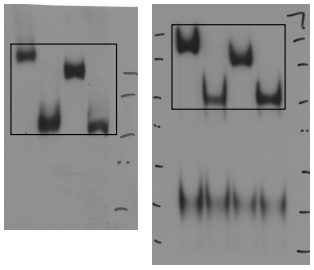

FIGURE 7F

SRE-Luciferase assay

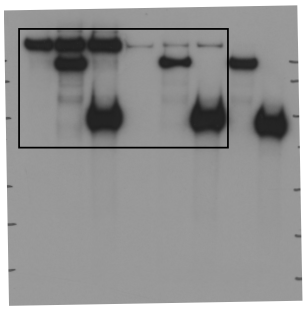

FLAG

FIGURE 7G

IP: YFP-ARHGEF11
IP: YFP-ARHGEF12
IP: YFP-PLEKHG4B
Co-IP: FLAG-Gα13

lysate FLAG FLAG

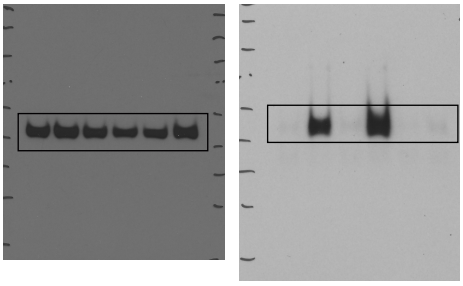

lysate GFP GFP

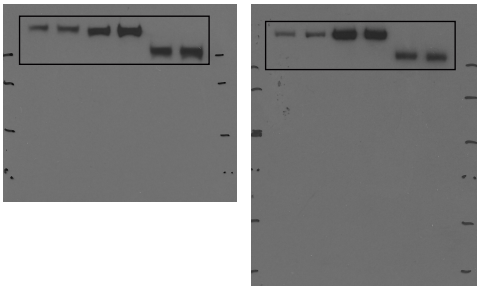

IP: YFP-ARHGEF11
IP: YFP-ARHGEF12
Co-IP: FLAG-Gα13

lysate FLAG FLAG

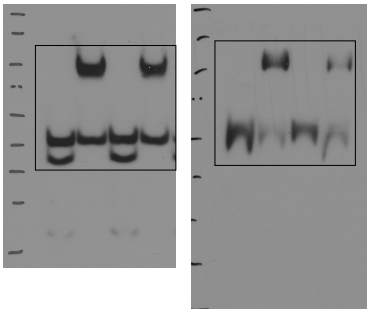

lysate GFP GFP

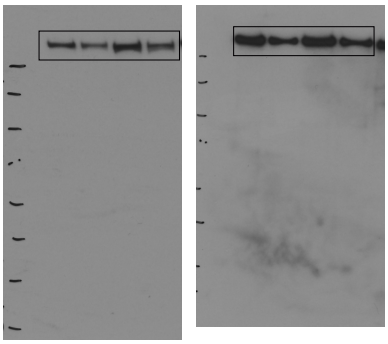

SRE-Luciferase assay

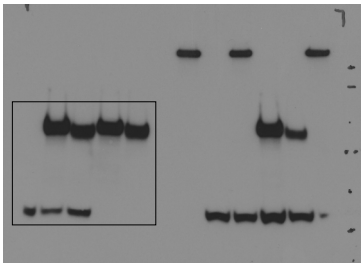

FLAG

Figure S8 (page 7/7)

FIGURE S7

IP: YFP-PLEKHGs
Co-IP: FLAG-ARHGEF11

FLAG

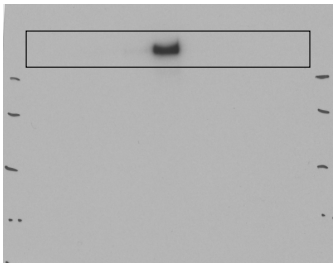

lysate FLAG

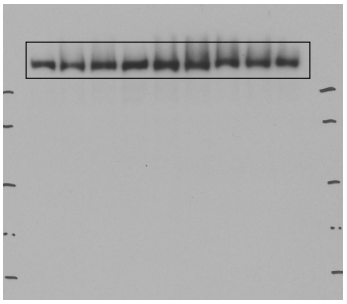

GFP

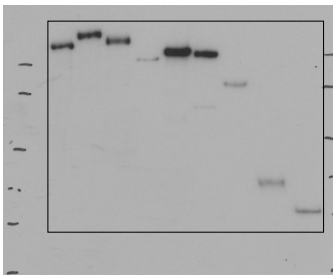

IP: YFP-PLEKHGs
Co-IP: FLAG-ARHGEF12

FLAG

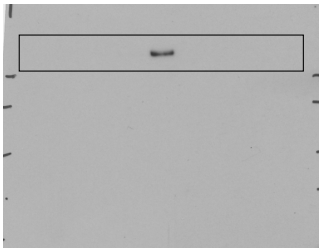

lysate FLAG

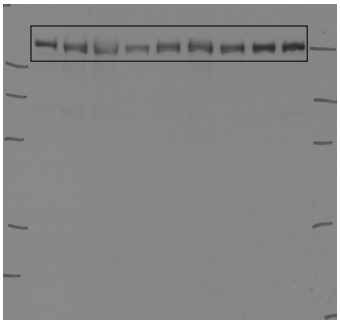

GFP

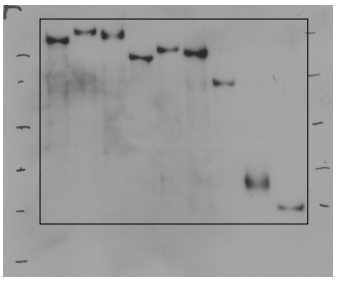

SRE-Luciferase assay

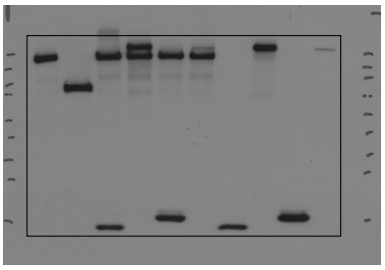

FLAG

Figure S8. Uncropped Western Blots from all figures